UNIVERSITY OF CALIFORNIA, SAN DIEGO

Naturally Derived Injectable Hydrogels for Treating Cardiovascular Diseases

A dissertation submitted in partial satisfaction of the requirements for the degree Doctor of Philosophy

in

Bioengineering

by

Todd Daniel Johnson

Committee in charge:

Professor Karen L. Christman, Chair
Professor Ehtisham Mahmud
Professor Mark Mercola
Professor Shyni Varghese
Professor Yang Xu

2015

The Dissertation of Todd Daniel Johnson is approved, and it is acceptable in quality and form for publication on microfilm and electronically:

_____

_____

_____

_____

_____

Chair

University of California, San Diego

2015

DEDICATION

I would like to dedicate this work to my loving parents and family. My parents have supported me more than I could have ever hoped. Through any major life decision they provided me the flexibility and financial backing to do whatever I thought was best. My older siblings have always been hard on me but that is what helped push me to accomplish things I never could have imagined. I am truly blessed to be part of such an amazing family. Thus, my family means everything to me and this work is dedicated to them.

TABLE OF CONTENTS

LIST OF ABBREVIATIONS

CLI – Critical Limb Ischemia

DMEM – Dulbecco's Modified Eagle's Medium

dsDNA – Double Stranded DNA

ECM – Extracellular Matrix

ECs – Endothelial Cells

FBS – Fetal Bovine Serum

GAGs – Glycosaminoglycans

GF – Growth Factors

H&E – Hematoxylin and Eosin

HCAECs – Human Coronary Artery Endothelial Cells

hCMPCs – Human Cardiomyocyte Progenitor Cells

HF – Heart Failure

HMM – Human Myocardial Matrix

HRP – Horseradish Peroxidase

hUC – Human Umbilical Cord

IFNγ – Interferon-γ

IPA – Isopropyl Alchohol

LASCA – Laser Speckle Contrast Analysis

MI – Myocardial Infarction

NDM – Non-decellularized matrix

NSG – NOD.Cg-Prkdc^{scid}Il2rg^{tm1wjl}/SzJ

PAD – Peripheral Artery Disease

PBS – Phosphate Buffered Saline

PGs - Proteoglycans

PMM – Porcine Myocardial Matrix

PS – Penicillin Streptomycin

qRT-PCR – Quantitative Real-Time Polymerase Chain Reaction

RASMCs – Rat Aortic Smooth Muscle Cells

ROIs – Regions of Interest

SD – Sprague Dawley

SDS – Sodium Dodecyl Sulfate

SEM – Scanning Electron Microscopy

SIS – Small Intestinal Submucosa

SKM – Skeletal Muscle Matrix

SMCs – Smooth Muscle Cells

SMs – Skeletal Muscle Myoblasts

TnT – Troponin T

αSMA – Alpha-Smooth Muscle Actin

LIST OF FIGURES

LIST OF TABLES

ACKNOWLEDGEMENTS

I would like to acknowledge Professor Karen L. Christman for her support as the chair of my committee. Without her continual help and encouragement this work would not have been possible.

I would also like to acknowledge all the co-authors for all of my publications, as the work presented here was truly a team effort. Also, thank you to all the past and present Christman Lab members who provided me with technical knowledge, experiment design feedback, and mental support.

Introduction, in part, is a reprint of the material as it appears in Expert Opinion on Drug Delivery 2012. Christman, Karen L. The dissertation author was the primary investigator and author of this paper.

Chapter 1, in full, is a reprint of the material as it appears in Nanotechnology 2011. Lin, Stephen; and Christman, Karen L. The dissertation author was the primary investigator and author of this paper.

Chapter 2, in full, is a reprint of the material as it appears in Biomaterials Science 2014. DeQuach, Jessica A.; Gaetani, Robert; Ungerleider, Jessica; Elhag, Dean; Nigam, Vishal; Behfar, Atta; Christman, Karen L. The dissertation author was the primary investigator and author of this paper.

Chapter 3, in full, is currently being prepared for submission for publication of the material. Rong, Zhili; Wang, Raymond M.; He, Jingjin; Wong, Michelle; Nigam, Vishal; Behfar, Atta; Xu, Yang; and Christman, Karen L. The dissertation author was the primary investigator and author of this material.

Chapter 4, in full, is submitted for publication. Ungerlieder, Jessica; Hernandez, Melissa; Elhag, Dean; Braden, Rebecca; Osborn, Kent; Mahmud, Ehtisham; and Christman, Karen L. The dissertation author was the primary investigator and author of this paper.

VITA

2006 Bachelor of Science in Engineering, Tulane University

2012 Master of Science, University of California, San Diego

2013 Candidate of Philosophy, University of California, San Diego

2015 Doctor of Philosophy, University of California, San Diego

PUBLICATIONS

Johnson, T. D., Lin, S. Y., & Christman, K. L. (2011). Tailoring material properties of a nanofibrous extracellular matrix derived hydrogel. *Nanotechnology*, *22*(49), 494015.

Singelyn, J. M., Sundaramurthy, P., **Johnson, T. D.**, Schup-Magoffin, P. J., Hu, D. P., Faulk, D. M., et al. (2012). Catheter-deliverable hydrogel derived from decellularized ventricular extracellular matrix increases endogenous cardiomyocytes and preserves cardiac function post-myocardial infarction. *Journal of the American College of Cardiology*, *59*(8), 751–763.

Johnson, T. D., & Christman, K. L. (2012). Injectable hydrogel therapies and their delivery strategies for treating myocardial infarction. *Expert Opinion on Drug Delivery*, 1–14.

Johnson, T. D., Braden, R. L., & Christman, K. L. (2014). Injectable ECM Scaffolds for Cardiac Repair. *Methods in Molecular Biology (Clifton, N.J.)*, *1181*, 109–120.

Johnson, T. D., DeQuach, J. A., Gaetani, R., Ungerleider, J., Elhag, D., Nigam, V., Behfar, A., & Christman, K.L. (2014). Human versus porcine tissue sourcing for an injectable myocardial matrix hydrogel. *Biomaterials Science*, *2*(5), 735–744.

Johnson, T.D., Ungerleider, J.L., Hernandez, M.J., Elhag, D.I., Braden, R.L., Osborn, K.G., Mahmud, E. & Christman, K.L. (2014). Injectable Tissue Specific Extracellular Matrix Hydrogel Promotes Tissue Remodeling, Arteriogenesis, and Perfusion in a PAD Model. *Submitted.*

Johnson, T.D., Rong, A., Wang, R.M., He, J., Wong, M., Nigam, V., Behfar, A., Xu, Y., & Christman, K.L. (2015). Humanized Mouse Model as Tool for

Testing the Human Immune Response to Xenogeneic and Allogeneic Decellularized Biomaterials. *In preparation for submission*.

Johnson, T.D., Hill, R.C., Dzieciatkowska, M., Nigam, V., Wang, R.M., Behfar, A., Christman, K.L., & Hansen, K.C. (2015). Absolute Proteomics Quantification of Decellularized Human Myocardial Matrix: A Comparison of Six Patients. *In preparation for submission*.

ABSTRACT OF THE DISSERTATION

Naturally Derived Injectable Hydrogels for Treating Cardiovascular Diseases

by

Todd Daniel Johnson

Doctor of Philosophy in Bioengineering

University of California, San Diego, 2015

Professor Karen L. Christman, Chair

Cardiovascular disease (CVD) is the number one killer in the western world and includes heart failure (HF) after myocardial infarction (MI) and peripheral artery disease (PAD) in the limbs. There is a significant need for developing new therapies to treat patients with these cardiovascular diseases. Recently, the fields of tissue engineering and regenerative medicine have

begun to develop naturally derived injectable biomaterials for treating cardiovascular diseases. These naturally derived biomaterials can be derived from a specific tissue's extracellular matrix (ECM) by applying decellularization techniques to either human or non-human tissue sources. This thesis provides crucial steps for the advancement and development of these biomaterials by investigating the importance of tissue specific and species specific sourcing, and investigating a humanized mouse model as a preclinical tool for testing naturally derived biomaterials. Included here is the development of two new human based biomaterials: a human myocardial matrix and a human umbilical cord matrix. The human myocardial matrix (HMM) was used as a tool for investigating allogeneic versus xenogeneic tissue sourcing and for studying the human immune response. The HMM was compared to a porcine myocardial matrix (PMM), which was previously developed as a potential therapy for treating HF after MI. The second material, the human umbilical cord matrix (hUC), was used for investigating the importance of developing tissue specific therapies for treating PAD. Also, the hUC was compared to a porcine skeletal muscle matrix (SKM), which was previously developed as a tissue specific therapy for treating PAD. It was shown in a preclinical animal study that the tissue specific naturally derived material has the potential for producing more desirable clinical outcomes than a non-tissue specific material. In conclusion, this thesis advanced the field of naturally derived biomaterials by presenting the humanized mouse model as a

viable tool for preclinical testing and showed the potential for these biomaterials to be used as a therapy for treating PAD.

INTRODUCTION

Cardiovascular Disease

Cardiovascular disease (CVD) is the number one cause of death in the United States and is involved in 1 of every 3 deaths [1]. Two significant cardiovascular diseases include heart failure (HF) after myocardial infarction (MI) and peripheral artery disease (PAD), which can advance to critical limb ischemia (CLI). Overall, the majority of CVD based fatalities are due to myocardial infarction (MI) and correlating heart failure (HF) [1]. After MI, caused by a blockage or occlusion of a coronary artery, a portion of the myocardial tissue develops permanent ischemic damage. A process of adverse changes called left ventricular (LV) remodeling follows the ischemic damage. During LV remodeling the wall of the heart thins and the chamber dilates involving myocyte slippage. As these physical alterations progress over time the function of the heart decreases. Thus, this maladaptive response leads to the progressive spiral towards HF and potentially death [2]. Current clinical approaches including pharmacological therapies and left ventricular assist devices (LVADs) have had limited success, and heart transplantation is limited by the substantial shortages in donor organs. There is therefore a profound need for new clinical methods for cardiac repair post-MI.

CVD not only causes ischemic damage in the heart but can also lead to complications in the extremities as well. Over 27 million patients in North American and Europe have been diagnosed with peripheral artery disease (PAD), of which 25% are considered to have severe PAD including muscle

atrophy [1, 3]. PAD is a chronic disease characterized by the buildup of atherosclerotic plaque in the lower extremities. Progressive narrowing of the vessels leads to hypoperfusion, ischemia and potential muscle damage. The initial hallmark symptom of the disease is intermittent claudication, which can progress to critical limb ischemia (CLI), an advanced form of the disease. CLI is characterized by rest pain and decreased tissue integrity, ultimately leading to ulcers or gangrene, and potentially amputation. This disease leads to an estimated 120,000 patients in the U.S. and 100,000 patients in Europe requiring lower extremity amputations annually [4]. Surgical and endovascular revascularizations [5-7] are frequently used, but 40% of patients with CLI do not have a revascularization option due to extreme tissue damage and diffuse atherosclerotic disease [8-10]. Due to these limitations, amputation rates have not changed significantly over the last 30 years creating a significant demand for new therapies [11].

Biomaterials Therapeutic Approach

The field of tissue engineering and regenerative medicine has developed several new potential post-MI and PAD treatments including the promising therapy of injectable hydrogels. A variety of biomaterials can be injected into the wall of the heart or muscles in the legs to ameliorate the maladaptive biological response that is observed in the LV post-MI or in the legs after ischemic damage. Both synthetic and naturally-derived biomaterials alone have been tested in small and large animal models to assess the

efficacy of injectable hydrogels [12-14]. These studies suggest biomaterials alone have the ability to stimulate endogenous repair mechanisms that can mediate the progression towards HF or total limb amputation. It is hypothesized that by providing a scaffold alone that supplies the ischemic tissue with biochemical cues, a niche for cellular infiltration, and structural support along with the possible recruitment of endogenous stem cells can potentially improve cardiac function or perfusion in the legs. Also, modulation of the mechanical properties of the infarct via tissue bulking has also been postulated to affect cardiac function, either by providing a structural support for the weakened myocardial wall in the setting of acute MI or by creating a more compliant wall in the setting of a chronic scar. These materials have also been utilized as platforms for delivering cellular therapies and/or other therapeutics, such as growth factors, to the ischemic area. Several reviews in the field have covered the delivery of biomaterials alone for MI and PAD as well as with these additional therapeutics [12, 13, 15-18].

Biomaterial Delivery Design Parameters

An important characteristic of using injectable biomaterials for treating cardiovascular diseases is the potential ability to provide a minimally invasive approach, which decreases the damage incurred to the targeted and surrounding tissues during delivery. For the legs this is accomplished by either systemic delivery by intravascular injection or via direct intramuscular injection. Ideally the method of delivery into the heart would be through the

use of current catheter technology since it provides a pathway for quicker clinical translation. A catheter-based approach for delivery into the heart or direct injection for delivery into the limbs would also lead to shorter procedure times along with quicker patient recovery compared to other more invasive procedures. Although, catheter delivery provides these promising characteristics for clinical translation, it does create some extra challenges for material design when compared to direct injection into the limbs. For instance, the biomaterial must be maintained in the liquid form for the duration of the injection procedure, which can sometimes be over an hour long. Similar challenge is applicable for treating PAD, but the time for injection will be shorter. Then, once within the myocardial wall or the skeletal muscle in the limbs the liquid should transition into a hydrogel to provide a scaffold for encouraging repair and regeneration.

More specifically for cardiac repair, therapeutic approaches of injectable hydrogels include epicardial, intracoronary, and endocardial injections from a single or double barrel syringe. Current cardiac catheter technology does not support the use of a double barrel delivery system or epicardial delivery into the myocardial tissue, although a less invasive, yet still surgical approach using endoscopic techniques can be used for epicardial injection. Direct epicardial and catheter-based endocardial delivery can be applied via puncture and injection into the wall of the heart. Intracoronary injections utilize the pathological phenomenon of leaky vasculature to deliver the liquid form of the material into the tissue from the bloodstream with no direct puncturing of

the tissue. This approach can occur either through a coronary artery or a venous approach through the coronary sinus into the targeted region. Distinctive material design parameters must be applied if intracoronary injection is employed including the requirement of the material to be non-thrombogenic and gel only once in the targeted tissue and not in the bloodstream [19]. This is also applicable to transendocardial injections, as some leakage into the bloodstream is known to occur [20].

In terms of targeting the skeletal muscle in the limbs for treating PAD, a different challenge is observed in that delivery is over a much larger area than the heart. Typically this means the area would need to receive numerous smaller injections and possibly several sets of injections over time to stimulate regenerative repair. However, the pattern or exact placement for delivery into either the heart or the limbs would need to be optimized before clinical translation.

ECM Derived Biomaterials

It has been identified that an injectable biomaterial alone, which includes both synthetic and naturally derived materials, would be a desirable approach for treating CVDs. Here we are interested in the application of decellularization techniques to develop new naturally derived biomaterials for tissue engineering and regenerative medicine, which has become an increasingly popular direction within the last decade [21-23]. This approach is attractive, when compared to synthetics, because tissue specific materials can

be developed by creating scaffolds derived from the same tissue being treated [24-26]. This is important since each tissue has a unique extracellular matrix (ECM) composition. In fact, there is building evidence that suggests the tissue-specific nature of the ECM is important for driving progenitor and stem cell differentiation and maturation, and promoting regeneration.[27-32] The ECM is a complex mixture of proteins, proteoglycans (PGs) and glycosaminoglycans (GAGs) [33-36], which provides cells with a dynamic three-dimensional environment inherent with a nanoscale architecture [37]. ECM components, such as fibrous collagen, have nanoscale structures that are important for cell-matrix interactions via membrane bound integrin proteins [37-39]. These interactions are essential for cell migration, proliferation, differentiation, mechanical stability, and signaling [38, 40-42]. The field of tissue engineering aims to create and tailor the extracellular environment by creating custom scaffolds from decellularized tissue for both *in vivo* and *in vitro* studies and applications [17, 43-45].

Thus, decellularized scaffolds have been developed with complex biochemical compositions that more closely replicate the targeted tissues native environment when compared to single component materials. Decellularization techniques have been applied to produce naturally derived biomaterials, which mimic the native tissue environment including both structural and biochemical cues.[21, 23] In the last decade, decellularized xenogeneic and allogeneic derived biomaterials have been implanted into millions of patients with acceptable tissue responses and positive clinical

outcomes.[46] The biomaterials have typically been from planar tissue sources such as small intestine submucosa, pericardium, dermis, and bladder, and used as surgical patches or wound healing scaffolds.[23, 46] Recently, these decellularized materials have been processed into a liquid form that can form nano-fibrous hydrogels upon injection into tissue [47-49].

Development of Injectable Decellularized Matrices

The Christman lab has previously developed porcine derived injectable matrices for treating both HF after MI and PAD in the limbs. Singelyn et al. created a tissue specific scaffold by decellularizing porcine myocardial tissue to develop a novel injectable therapy for treating MI [47]. The porcine myocardial matrix (PMM) was tested in a rat MI model by occlusion of the left coronary artery for 25 minutes followed by reperfusion [50]. The material was injected at 6 mg/ml in phosphate buffered saline (PBS) 2 weeks post-MI in 75 µL injections into the infarcted region. From this model they showed an ability to maintain ejection fraction (EF) along with inhibiting signs of LV dilation by limiting the increase in end diastolic volume (EDV) and end systolic volume (ESV). Histological analysis showed an increase in proliferating cells and recruitment of c-kit+ stem cells in the infarcted tissue indicating the material's impact on cellular remodeling. They also successfully tested the feasibility of injecting the myocardial material in a porcine MI model via catheter delivery with 15-25 transendocardial injections of 0.25 mL each [50]. Next in a large animal MI model, the PMM material was delivered using similar methods via a

percutaneous transendocardial two weeks after MI. Three months later there was increased cardiac muscle, reduced infarct fibrosis, and improved both global and regional cardiac function as measured by echocardiography, suggesting it has significant translational potential.[29] Safety was also investigated along with studying the host immune response to the biomaterial in rats and hemocompatibility studies were implemented with human blood. These studies combined provide strong support for moving this porcine myocardial matrix biomaterial into clinical trials.

Minimally invasive, injectable therapies have also been investigated as a promising option for treating patients with CLI. Potential therapies that utilize cells, growth factors (GF), and/or gene therapies are currently in clinical trials with the goal of increasing vascularization and perfusion in the ischemic limb [51-53]. Cell therapy has however been plagued by poor cell retention and survival [54], as well as the viability and expense issues surrounding a living product. GF therapy has suffered from poor retention of therapeutic proteins in the tissue [55], and gene delivery results have not translated to clinical benefit [56]. While injectable biomaterial alone approaches have been explored to treat ischemic cardiac muscle [13, 14, 16, 57], they have not been extensively explored for treating the ischemic skeletal muscle associated with PAD and CLI. This approach is particularly attractive since it can be an off-the-shelf available therapy with reduced costs compared to other regenerative medicine therapies [18].

Our group has previously reported the development of a tissue specific injectable hydrogel derived from decellularized porcine skeletal muscle matrix (SKM) as a potential therapy for treating CLI [58]. In a rodent hindlimb ischemia model, histological examination over the first two weeks of treatment showed a significant increase in vascularization, muscle progenitors, and proliferating muscle cells in the SKM hydrogel treated animals compared to a collagen control [58]. These results suggested that this biomaterial alone had the potential to not only address the first objective for a PAD therapy, increased tissue perfusion, but could also aid in treating the associated muscle atrophy.

Thesis Goal and Chapter Outline

The studies presented in this thesis moved forward the field of naturally derived injectable biomaterials for treating cardiovascular disease by providing a greater understanding of their material properties, developing two new human based biomaterials, showing their ability to increase total limb perfusion in an animal model for PAD, and characterizing their human immune response by utilizing a new tool for biomaterials testing, the humanized mouse model. These advancements were organized into four chapters.

In the first chapter an injectable biomaterial derived from decellularized ECM for the treatment of cardiovascular diseases was more fully characterized. The versatility and ability to modulate material properties by varying the gelation parameters of a previously developed PMM were manipulated and assessed. The study showed that theses materials could be

varied and tailored for a given application by simply varying gelation parameters.

The second chapter showed the development of an allogeneic injectable biomaterial derived from decellularized ECM for comparison to a xenogeneic biomaterial. The potential for allogeneic versus xenogeneic tissue sourcing was investigated for a myocardial matrix hydrogel, which was developed to treat heart failure after myocardial infarction. It was shown that human myocardial matrix (HMM) biomaterial developed from human cadaveric donors was not a viable option for translation into the clinic and that future clinical studies should be implemented with the porcine myocardial matrix (PMM). However, the HMM material is still a viable option as a tool for in vitro or in vivo studies.

In the third chapter the humanized mouse model is presented and tested as a novel tool for biomaterial biocompatibility testing. The humanized mouse model was able to distinguish between allogeneic (HMM) and xenogeneic (PMM) biomaterials showing its potential as a preclinical tool for testing naturally derived biomaterials. This supported the conclusion that these biomaterials stimulate a T-cell mediated immune response and that testing or using these materials in an immune compromised model will not sufficiently mimic the appropriate immune response. It was also shown that the xenogeneic material produced a pro-remodeling immune response in a wild type animal and this was also maintained in the humanized mouse model.

The final chapter evaluated the potential for a novel injectable ECM biomaterial (hUC) and a tissue specific ECM biomaterial (SKM) to stimulate regeneration and increase perfusion in a hind limb ischemia model. The hUC matrix and SKM matrix both showed increased tissue perfusion in a hind limb ischemia model. However, muscle tissue remodeling was slightly improved by SKM indicating that a tissue specific material could potentially produce more desirable clinical outcomes for treating patients with PAD.

CHAPTER 1 - Tailoring material properties of a nanofibrous extracellular matrix derived hydrogel

1.1 Introduction

The most characterized and prominent component of the ECM is collagen. Collagen is a fibrous protein that is used for numerous applications in science and medicine including tissue culture coatings, burn-victim dressings, drug delivery, and cosmetic injections [45, 59]. Native collagen can be processed into an injectable solubilized form, which can self-assemble under certain conditions into a hydrogel with nanoscale fibrous structure [40, 60, 61]. The material properties and cell-matrix interactions of these gels have been well characterized. For example, varying temperature, ion concentration, phosphate content, pH, and material concentration is known to alter gelation kinetics, stiffness, and the nanoscale fibrous architecture of the collagen hydrogels [60-65].

Collagen is, however, a single component of the ECM and cannot fully mimic the biochemical complexity of the cells native environment. This limitation has motivated the development of more complex materials including Matrigel, decellularized tissues [66], and mixtures of single proteins (ie. collagen, fibronectin, elastin) with other ECM components (ie. PGs, GAGs) [17, 40, 43, 67, 68]. Decellularized tissues can be further processed into liquids and used to create gels with porous fibrous nanostructures similar to the collagen hydrogels [47, 69, 70]. Each tissue in the body contains a unique ECM, so decellularized materials have distinctive compositions specific to their tissue of origin [47, 67].

This diversity allows for the development of tissue-specific scaffolds for appropriate cell-matrix interactions. So far, ECM hydrogels derived from small intestinal submucosa (SIS), adipose tissue, bladder, pericardium and myocardium have been reported [47, 71-74]. The effect of cross-linking on hydrogel stiffness, degradation properties, and cell migration has been examined with an ECM hydrogel [75]; however, no studies have examined how gelation kinetics, stiffness, swelling ratio, and nanoscale architecture of ECM derived hydrogels can be modulated through altering gelation conditions. Unlike collagen, the modulation of ECM matrix gelation parameters in order to tailor the material properties has not been explored. In this study we aimed to tailor the material properties of a self-assembling ECM hydrogel and investigate the effect of varying temperature, ionic strength, pH, and material concentration on material properties. The ECM material was analyzed with scanning electron microscopy (SEM) to characterize the nano-scale architecture, rheometry to measure stiffness and viscosity, and spectrophotometry to assess gelation kinetics. An ECM hydrogel derived from porcine myocardial tissue was selected for analysis in this study. As previously discussed, this myocardial matrix material was developed as a tissue specific injectable scaffold for cardiac tissue engineering [47]. Several injectable materials, including synthetic and naturally derived materials such as the myocardial ECM hydrogel invested here, have shown promise for treating myocardial infarction, and this field has rapidly expanded in recent years [76-79].

1.2 Results

1.2.1 Effect of Temperature

The gelation temperature is an important parameter for self-assembling hydrogels when considering them as injectable materials for clinical applications, particularly their ability to gel at body temperature. Once processed, the myocardial matrix material is a free flowing liquid and upon increasing the temperature it forms into a gel (Figure 1.1). The material at physiological pH and salt concentrations, when stored at either 4°C or room temperature for 24 hours, remained a liquid. Increasing the concentration from 6 to 8 mg/mL did not result in gelation at these temperatures. However, when incubated at 37°C, the material self-assembled into a gel that maintained shape at both concentrations (Figure 1.1).

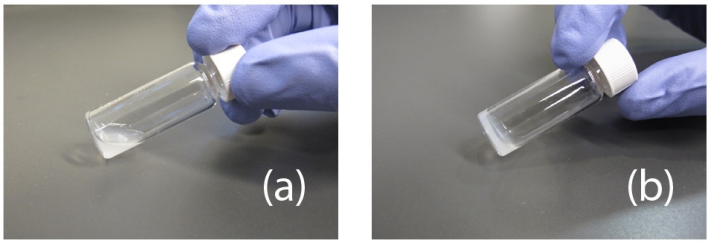

Figure 1.1: Gelation of myocardial matrix hydrogel. (a) At 4°C and 22°C the material is maintained in the liquid form. (b) When at 37°C the material forms a gel that maintains shape.

Scanning electron microscopy (SEM) was used to assess the presence of a nanoscale fibrous structure at each of the temperatures for both concentrations at standard physiological conditions. The images were used to verify which temperatures produced fibril formations. The SEM images at 20,000x confirmed that the material did not form a nanoscale fibrous network at the two lower temperatures for either concentration whereas at 37°C, fibers were formed (Figure 1.2). The lower two temperatures tested had some singular fibers, but the majority of the material was solid and nonporous as a result of the glutaraldehyde crosslinking during processing for SEM. Both material concentrations at 37°C had clear interwoven networks of linear fibers indicating successful fibrillogenesis. The morphologies for both concentrations at 37°C were similar but showed great variation from location to location when viewed at 20,000x. This fluctuation in local density and morphology is better shown in the 5,000x images in Figure 1.3. Since 4°C and 22°C did not form gels at 6 mg/ml and 8 mg/ml, these groups were not examined in subsequent experiments.

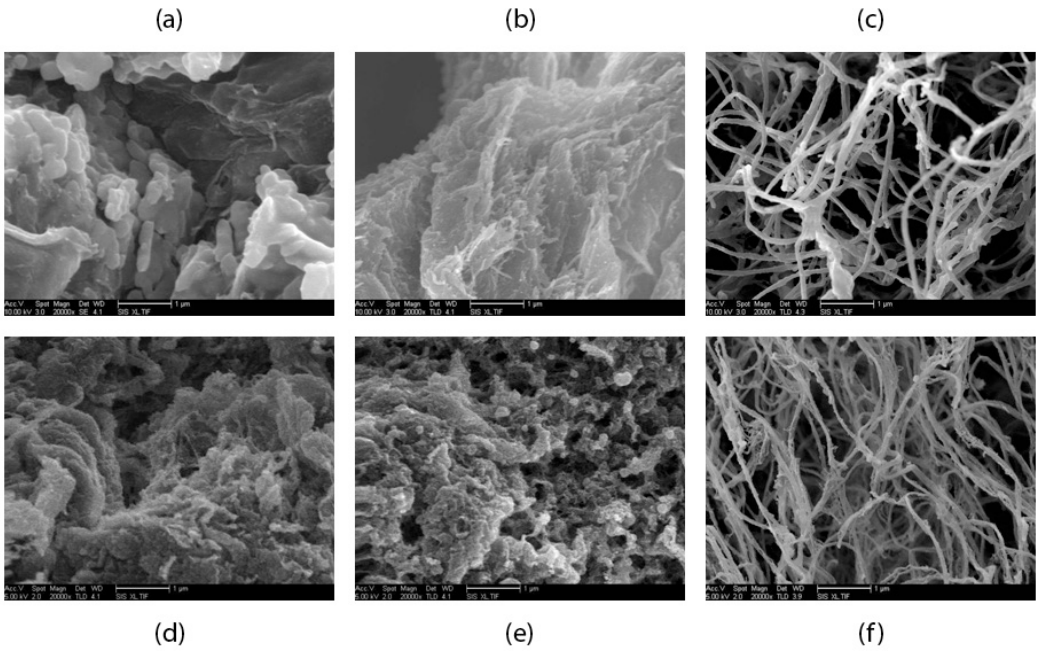

Figure 1.2: Scanning electron microscopy images of the material 24 hours after attempted gelation at different temperatures. (a) and (d) 4°C. (b) and (e) room temperature. (c) and (f) 37°C. (a)-(c) are 6 mg/ml and (d)-(f) are 8 mg/ml material concentration. Scale bars are 1 mm.

1.2.2 Effect of ionic strength, pH, and concentration

1.2.2.1 Scanning Electron Microscopy

The gels under each of the explored conditions were imaged using SEM to confirm fiber formation and analyze the fibrous structure. Gelation and the formation of a nanofibrous structure occurred for the test ranges of salt concentration (0.5x - 1.5x PBS), pH level (7.4 - 8.5), and concentrations of the myocardial matrix material (6 - 8 mg/ml) as confirmed by SEM images at 5,000x in Figure 1.3. A complex network of nanoscale fibers was consistently formed for each condition. However, each of the gels displayed inhomogeneity of the fiber matrix density; regions of increased and decreased fiber density within a single gel made it difficult to assess the overall fiber

matrix from the SEM images. These variations in densities at the nanoscale can be observed in Figure 1.3

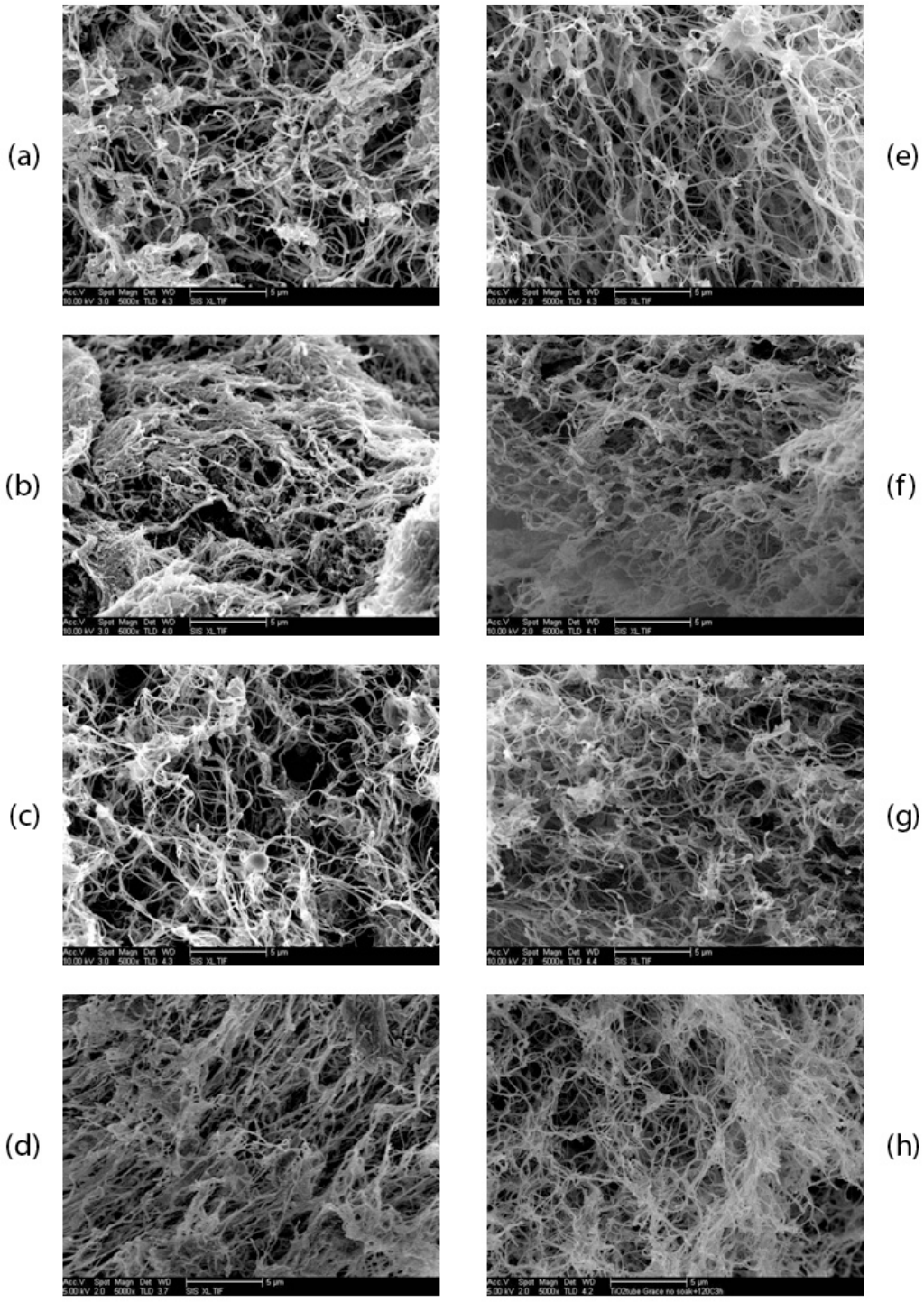

Figure 1.3: SEM images of the gels after 24 hours of incubation at 37°C. Left column is at 6 mg/ml and right column is at 8 mg/ml. (a) and (e) 0.5x PBS. (b) and (f) 1.5x PBS. (c) and (g) standard physiological conditions of 7.4 pH and 1.0x PBS. (d) and (h) pH 8.5. Scale bars are 5 mm.

Images were also taken at 20,000x and used to analyze the impact of salt, pH, and material concentration on fiber diameter (Figure 1.4). No statistically significant changes in average fiber diameter were observed when varying each of these parameters (Table 1.1). Average fiber diameter was consistently around 100nm for all conditions with distributions over the range of 30nm to 250nm.

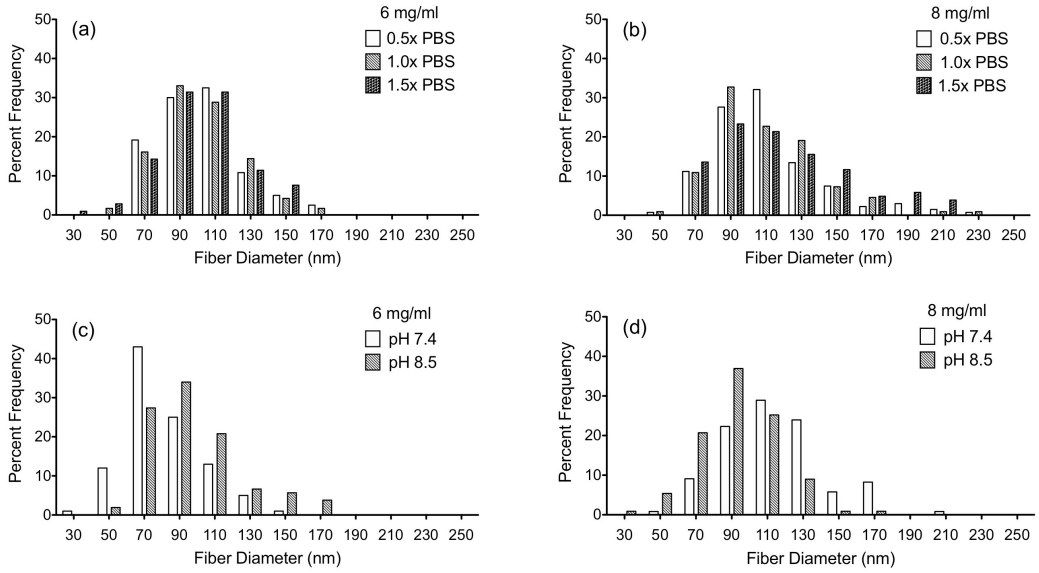

Figure 1.4: Histograms of the fiber diameter distributions measured from SEM images after gelation for 24 hours at 37°C. (a) and (c) 6 mg/ml. (b) and (d) 8 mg/ml. (a) and (b) salt concentration is varied. (c) and (d) pH is varied.

Table 1.1: Average Fiber diameter of gels incubated at 37°C for 24 hours (nm).

Condition	6 mg/ml	8 mg/ml
Standard	92.92 ± 24.38	112.20 ± 28.74
0.5x PBS	102.49 ± 22.79	111.37 ± 30.77
1.5x PBS	101.46 ± 24.32	119.80 ± 36.99
8.5 pH	96.04 ± 26.24	92.60 ± 21.86

1.2.2.2 Rheometry: Storage Modulus, Loss Modulus, and Viscosity

Rheometry was used to measure the storage modulus and loss modulus of the gels at each condition to determine if salt, pH, or material concentration alters the mechanical properties of the gels (Table 1.2). The storage modulus for the four conditions at 6 mg/ml ranged from 2.58-10.23 Pa and the 8 mg/ml gels were 5.94-12.36 Pa. Increasing material concentration from 6 mg/ml to 8 mg/ml consistently produced gels with a trend of higher storage modulus for all conditions, thus increasing concentration leads to stiffer gels. Raising salt concentration lead to a significant decrease in the storage modulus (G') of the 6 mg/ml gels with a similar trend observed for the 8 mg/ml group as shown in Figure 1.5a. When salt concentration was increased from 1.5x PBS to 0.5x PBS the storage modulus more than tripled on average at 6 mg/ml and doubled at 8 mg/ml. The changes in material properties of the gels with alterations in salt concentration were also observed during their handling. This indicates that the concentration of salt ions in solutions impacts the fibrillogenesis of the myocardial matrix leading to

changes in the bulk material properties of the hydrogels. When increasing the pH from 7.4 to 8.5 no significant change in the storage modulus was measured for either material concentration (Figure 1.5b). A ten-fold modulation in proton concentration had less of an impact on the storage modulus than decreasing the salt concentration by half. Increased gel stiffness was still observed with increasing material concentration, with significance at both pH 7.4 and pH 8.5. The loss modulus (G") followed the same trends as the storage modulus (Table 1.2). The loss modulus for each of the conditions had a range of 0.467-1.652 Pa and 1.70-2.72 Pa for the 6 and 8 mg/ml samples, respectively. Once again, there was more than a three-fold increase in the loss modulus as the salt concentration decreased from 1.5x PBS to 0.5x PBS for the 6 mg/ml samples and almost doubled for the 8 mg/ml samples. Also, as material concentration was increased there was a consistent trend of increasing loss modulus.

Table 1.2: Storage modulus (G') and loss modulus (G") of static gels after 24 hours gelation at 37°C.

Condition	*G' (Pa)*	*G" (Pa)*
6mg/ml		
Standard	5.28 ± 0.41	0.893 ± 0.085
0.5x PBS	10.23 ± 0.49	1.652 ± 0.092
1.5x PBS	2.58 ± 0.09	0.467 ± 0.21
pH 8.5	4.63 ± 0.51	0.785 ± 0.12
8mg/ml		
Standard	9.52 ± 3.77	1.75 ± 0.72
0.5x PBS	12.36 ± 2.74	2.50 ± 0.78
1.5x PBS	5.94 ± 2.21	1.70 ± 0.38
pH 8.5	8.53 ± 0.34	2.72 ± 1.0

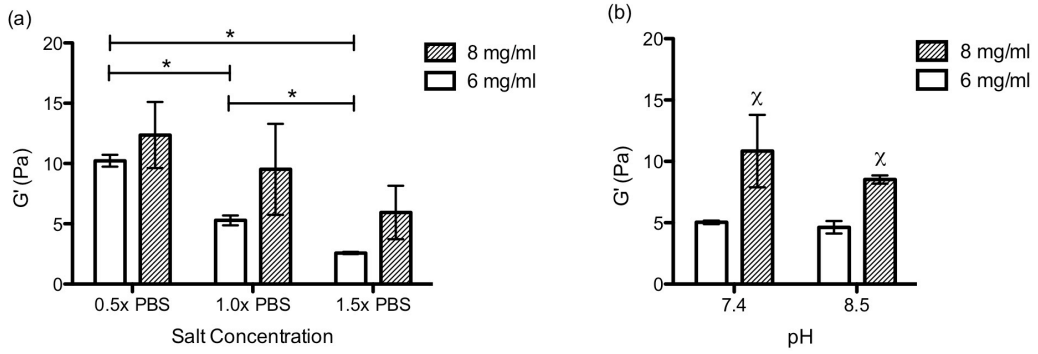

Figure 1.5: Storage modulus (G') in pascals of the static gels after 24 hours gelation at 37°C. (a) pH 7.4 with salt concentrations of 0.5x, 1.0x, and 1.5x PBS. *p<0.05 (b) 1.0x PBS with pH of 7.4 and 8.5. One-way ANOVA for pH at 6 mg/ml (p=0.0012). Inner group significance for pH or salt concentration *x* = p<0.05 compared to lower concentration.

When considering a material for delivery via injection, the viscosity in the liquid state is important. The myocardial material was thus assessed over a range of shear rates and complex viscosity was measured using a rheometer. Complex viscosity for all samples decreased as shear rate increased, providing a linear trend when plotted on a log-log scale. Because of the linear nature of the data on a log-log scale, a power equation (1) was used to fit the data (Table 1.3). The reported values of (*k*) and (*n*) are constants from the power equation used to fit the data. The coefficient of determination (r^2) indicates the accuracy of the power equation fit with a value of 1 indicating a perfect fit. Changes in complex viscosity between the different conditions were only observed for different material concentrations with pH and salt concentration having no effect. Increasing the myocardial ECM concentration when in liquid form creates increased intermolecular forces leading to an increase in viscosity. There was a significant increase in complex viscosity when material concentration was increased at standard conditions ($p = 0.0001$) and this can be observed as vertical shift of the data points in figure 6. This trend is also confirmed by the increase in the (*k)* values between the 6 mg/ml and 8 mg/ml samples (Table 1.3). Since plotted on a log-log scale, the negative values for (*n*) correlate to the slope and indicate that the material is shear thinning. The (*n*) values for the 6 mg/ml range from -0.466 to -0.550 and are significantly larger than the 8 mg/ml values, which range from -0.580 to -0.656, and this slight variation in slope can be observed in figure 6. Because the material is shear thinning, it will have a lower

viscosity when experiencing higher shear rates, such as those that occur when passing through a catheter or needle during an injection.

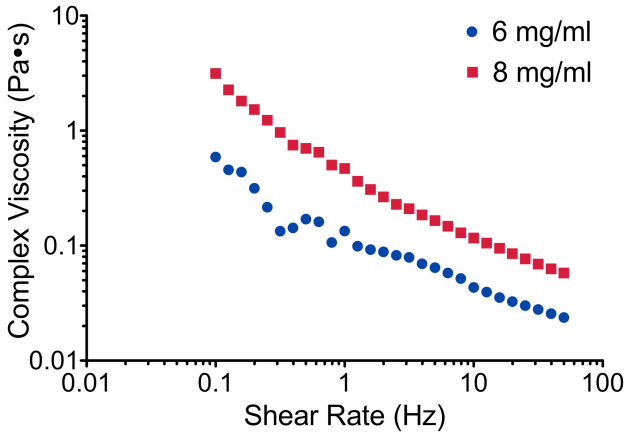

Figure 1.6: Complex viscosity of the myocardial matrix in liquid form in standard conditions at 25°C plotted over shear rate on a log-log scale.

Table 1.3: Complex viscosity of the myocardial matrix material at 25°C for frequencies from 0.1-50 Hz.

Condition	*k*	*n*	r^2
6mg/ml			
Standard	0.1300	-0.466	0.955
0.5x PBS	0.1548	-0.523	0.959
1.5x PBS	0.1580	-0.519	0.963
pH 8.5	0.2030	-0.550	0.978
8mg/ml			
Standard	0.4976	-0.617	0.982
0.5x PBS	0.4402	-0.656	0.994
1.5x PBS	0.4641	-0.580	0.983
pH 8.5	0.4568	-0.606	0.988

1.2.2.3 Swelling Ratio

Swelling ratios by mass for the five conditions at both material concentrations are summarized in Table 1.4. The mean values for swelling ratio ranged from 55.7 - 58.4 and did not show any significant variation between the groups.

Table 1.4: Swelling ratio by mass after gelation at 37°C.

Condition	6 mg/ml	8 mg/ml
Standard	58.4 ± 10.20	57.4 ± 2.39
0.5x PBS	55.9 ± 8.36	57.0 ± 1.19
1.5x PBS	56.4 ± 5.48	55.8 ± 4.68
pH 8.5	55.7 ± 4.34	56.2 ± 2.63

1.2.2.4 Turbidimetric gelation kinetics

We observed marked changes in gelation when varying salt concentration, and therefore next performed turbidimetric assessment to quantify gelation kinetics. The absorbance of the gels at 405 nm was measured to analyze the turbidimetric gelation kinetics. The results for the material at 6 mg/ml, as absorbance and normalized absorbance plotted over time, are shown in Figure 1.7. The calculated parameters $t_{1/2}$, t_{lag}, and S from the linear fits are summarized in Table 1.5. The results for 1.5x PBS were omitted because of the long gelation time. After 8 hours, the 1.5x PBS samples did not show an increase in absorbance and when visually inspected had not formed gels. When these gels were further incubated at 37°C for a total of 16 hours, gels were formed. Therefore, gelation time for 1.5x PBS samples ranges from 8 to 24 hours. Changing salt concentration had a significant effect on gelation kinetics. Samples with salt concentrations of 0.5x PBS had a significant decrease of $t_{1/2}$ and increase of slope (Table 1.5). This indicates that lowering salt concentration shortens the gelation time with an

increase in the rate of gelation. Thus, the observations of dramatically slower gelation at 1.5x PBS were consistent with these findings.

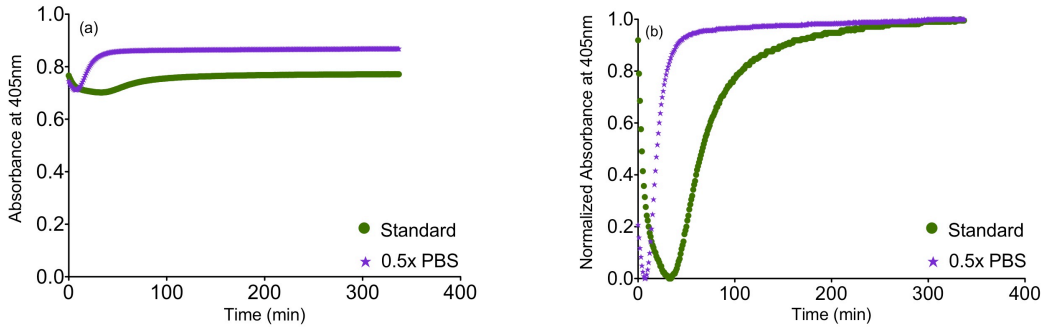

Figure 1.7: Turbidity results averaged per condition plotted over time for the gelation of the myocardial matrix at 37°C for 6 mg/ml. (a) Absorbance at 405nm. (b) Normalized absorbance at 405nm.

Table 1.5: Turbidity results for lag time (t_{lag}) slope of linear region (S), and half gelation time ($t_{1/2}$) at 6 mg/ml.

Condition	t_{lag}	S	$t_{1/2}$
Standard	40.28 ± 1.91	0.01867 ± 0.0012	67.14 ± 3.40
0.5x PBS	11.40 ± 2.17*	0.05067 ± 0.0021*	21.27 ± 2.33*

*p<0.0001 compared to standard condition.

1.3 Discussion

Naturally derived ECM hydrogels have become a new biomaterial of investigation for use as a porous fibrous scaffold that is tissue specific [47, 70, 71, 73, 80]. These hydrogels produced from decellularized tissue can be processed into an injectable liquid material that gels via self-assembly at physiological conditions for pH, temperature, and salt concentration. While the native 3D structure is lost, ECM hydrogels are advantageous over intact decellularized

tissues in that they can be delivered minimally invasively through a simple injection. Once gelled, the ECM hydrogels form a complex nanoscale mesh of fibers. This architecture is significant since in the native tissue there are nanoscale cell-matrix interactions via integrins that are important for cellular migration, proliferation, and differentiation [37, 38, 42]. Similar to other nanofibrous materials, ECM hydrogels have a high surface area-to-volume ratio providing increased area for integrin binding [44, 81]. Mauck et al. has emphasized the importance of characterizing tissue engineering constructs from their nanoscale fibrous formations to their macro-level material properties [82]. Scaffolds that provide a nanostructure and biochemical cues designed for tissue engineering and regenerative medicine must be tailored to have the appropriated characteristics and material properties for a given application [17, 38, 44, 45, 80].

In this study an ECM hydrogel developed from porcine myocardial tissue was more fully characterized to increase the understanding of modulating its material properties. Particular interest was placed on the parameters of gelation including temperature, salt concentration, pH, and material concentration since each has been shown to alter properties of collagen hydrogels. These parameters impacted the final material, which was assessed for gelation kinetics, viscosity, fibrous nanostructure, swelling ratio by mass, and stiffness. Soluble collagen is known to form gels at physiological pH and salt concentrations from 4°C to 37°C [60, 61]. However, the myocardial matrix showed a lack of gelation and fiber formation at lower temperatures

(4°C and 22°C), indicating a difference in its response to temperature when compared to collagen. This is a beneficial attribute when considering this material for injection via catheter since it can maintain its liquid form at room temperature and gels once in the body at 37°C [80].

Each condition explored produced nanoscale fibrous structures with porous architectures when gelled at 37°C as shown in Figure 1.5. Heterogeneity between different locations in the gels made it difficult to assess the overall tightness of the fiber matrix of each gel. This point-to-point variation in the composition of the myocardial matrix is consistent with results for collagen. Latinovic et al. showed a dramatic change of mechanical properties from location to location in self-assembled collagen gels indicating structural inhomogeneity [83]. It was hypothesized that this variation is due to the mechanism of self-assembly and the importance of nucleation sites for the formation of the fibrous structure [40, 83]. Thus, based off the local SEM images from this study, the overall organization and tightness of the material at the different conditions could not be determined. Analysis of the mean fiber diameter from the SEM images showed a consistent average fiber diameter of around 100nm with the range from below 30nm to over 250nm. The changes of the explored parameters did not lead to a significant shift of fiber diameter distributions. Collagen gels have showed varied fiber diameters depending on the conditions of gelation and have reported values similar to the myocardial matrix hydrogels [40, 60, 63, 64, 84-86].

Changes in salt concentration had the most dramatic impacts on stiffness and gelation kinetics. As salt concentration was increased, the rate of gelation decreased and half time of gelation significantly increased. For the 6 mg/ml gels at standard conditions, the material had a $t_{1/2}$, as determined by spectrophotometry, of 67.14 ± 3.40 minutes after incubation at 37°C. But, when concentration was increased to 1.5x PBS gelation took longer than 8 hours. Decreasing the salt concentration to 0.5x PBS rapidly decreased the $t_{1/2}$ down to 21.27 ± 2.33 minutes. The change in gelation kinetics with salt concentration was consistent with collagen [87], and was also concurrent with a significant change in gel stiffness. Increasing the salt concentration lead to a decrease in the storage modulus of the gels (Figure 1.3). It has previously been shown that the stiffness of a gel or scaffold can impact cell fate [88], and thus being able to modify this material property may be advantageous.

When increasing pH from 7.4 to 8.5 there was no significant change in storage modulus. Collagen, on the other hand, has shown changes in mechanical properties when pH levels are altered, with increasing stiffness as the pH is increased [87]. However, Rosenblatt et al. had an inversion of this trend for their collagen gels formed at the 25°C compared to 20°C [61]. Williams et al. and Harris and Reiber noted changes and a decrease in fiber formation quality at high pH [60, 89], which was not observed for the myocardial matrix from pH 7.4 to 8.5. Li et al. explored collagen gels over a pH range of 6.6 to 8 with a trend of increasing fiber diameter as assessed with transmission electron microscopy [85]; however, the myocardial matrix did show a significant change

in fiber diameter over the tested parameters. Differences in the material, when compared to collagen, were expected because of the biochemical and structural importance of PG and GAG in the matrix formation [37, 40, 67, 90]. The presence of collagen along with other ECM components in the myocardial matrix material has been previously shown [91, 92].

When either pH or salt concentration was varied, the impact of altering material concentration in the gels was consistent. Increasing material concentration lead to a trend of increasing the storage modulus and a significant increase in complex viscosity, which is consistent with collagen [93]. Gobeaux et al. showed changes in collagen fiber diameter with increasing concentration over large changes at high concentrations from 50-1000 mg/ml [63]. For the myocardial matrix material no significant increase in fiber diameter was observed as material concentration increased.

It was shown for all samples in liquid form at 25°C that as shear rate increased, there was a decrease in complex viscosity. This phenomenon is known as shear-thinning, which also occurs with collagen when in the liquid form [72, 94]. Complex viscosity of the material at 25°C changed only with material concentration, and not with salt concentration or pH. Viscosity is defined as the resistance of flow to a fluid and is affected by the degree of intramolecular and intermolecular interactions. The increase of complex viscosity at higher material concentration can be explained by an increase in intermolecular forces [94]. Although mechanical strength, gelation kinetics, and viscosity were altered it was shown that the swelling ratio by mass is

maintained for all conditions. The mass of the material increased by a factor of over 55 times its original weight when transitioning from a dry powder into a hydrogel. The standard deviations for the swelling ratios had a range of 2-20% of the mean value. Thus, the variation between the groups might have been masked by the large discrepancies within any given group.

The myocardial matrix derived ECM gel was consistent with several material property trends seen with collagen hydrogels. Both materials in liquid form are shear thinning and once over a temperature threshold form into a heterogeneous nanofibrous mesh. The trend of increasing gel stiffness and gelation kinetics when decreasing salt content was conserved. Also, increasing material concentration leads to an increase in viscosity and consequently gel stiffness for the myocardial matrix and collagen. The myocardial ECM is known to be predominately collagen, and given the similarities in material properties between the myocardial matrix and collagen gels, the main driving force for the self-assembling aspect of the myocardial material is likely its inherent collagen components. However, differences in the material when compared to collagen were observed in that the material did not show a significant increase in storage modulus when pH was increased to 8.5 and average fiber diameter did not alter for any of the conditions explored. Also, even though the same trends were conserved for gelation kinetics, the temperature of gelation and the actual times and rates of gelation varied. Variation from collagen gels was expected since the myocardial matrix

hydrogel has previously been shown to contain other ECM components including sulfated GAGs [47, 92].

1.4 Conclusion

Tailoring material properties, as commonly explored for collagen hydrogels, by varying gelation parameters had not been previously investigated for decellularized ECM based hydrogels. From this study we were able to modulate the material properties of the naturally derived ECM material developed from porcine myocardial tissue. Gelation can be inhibited by maintaining the material at or below 22°C, but once brought to body temperature of 37°C, gelation is initiated. Once at 37°C the rate of gelation can be controlled and increased from ~20 minutes to over 8 hours by increasing salt concentration. This increase in salt concentration, or decrease in rate of gelation, correlates to a decrease in the storage modulus of the material. Once gelled at 37°C at any of the explored conditions, a complex network of nanoscale fibers is formed with a mean fiber diameter in the range of 100 nm. By increasing material concentration there is an increase in the complex viscosity of the liquid suspension and the storage modulus once gelled. These parameters could therefore be modulated to tailor the myocardial ECM hydrogels for both *in vitro* and *in vivo* applications.

1.5 Methods and Materials

1.5.1 Tissue Decellularization and Material Processing

Porcine myocardial tissue was harvested and decellularized following a modified version of a previously reported protocol [47]. In brief, the left ventricle was sliced into small pieces and decellularized in a solution of 1% (wt/vol) sodium dodecyl sulfate (SDS) (Fischer Scientific, Hanover Park, IL), phosphate buffered saline (PBS), and 0.5% Penicillin/Streptomycin (GIBCO, Invitrogen, Carlsbad, CA). Once decellularized after 3-5 days with daily solution changes, the tissue was rinsed with water to remove residual SDS then frozen at -80°C. The frozen decellularized material was lyophilized, and milled into a fine powder using a Wiley Mini Mill. The powder was stored at -80°C until needed for use.

1.5.2 ECM Gel Formation

The extracellular matrix material was enzymatically digested by adding a 1 mg/ml solution of pepsin (Sigma, St. Louis, MO) in 0.1 M HCl such that the final concentration of material was 10 mg/ml [47]. The material was digested for 48-60 hours at room temperature with constant stirring until the liquid was homogeneous with no visible particles. The pH (7.4 or 8.5) and salt concentration (0.5x, 1.0x, or 1.5x PBS) was adjusted using 1.0 M NaOH and 10x PBS, respectively, to end with the desired final material concentration (6 mg/ml or 8 mg/ml). The final mixture was then allowed to gel for 24 hours at 4°C, 22°C, or 37°C. Standard conditions are defined as physiological conditions of pH 7.4, 1.0x PBS, and 37°C. Only one parameter (temperature,

salt concentration or pH) at a time was varied away from these standard conditions for any of the following experiments.

1.5.3 Scanning Electron Microscopy

The gels were crosslinked with 2.5% glutaraldehyde (Sigma-Aldrich, Grade II, 25%, St. Louis, MO) for 2 hours then dehydrated with a series of ethanol washes of increasing concentration (30%, 50%, 75%, and 100%). After storing overnight in 100% ethanol, the gels were critical point dried from ethanol in CO_2 using a Tousimis AutoSamdri 815A. Samples were mounted and then sputter coated with Chromium (Cr) or Iridium (Ir) using an Emitech K575X Sputter Coater [95]. Imaging was done with a FEI XL30 UHR SEM. All conditions were done in triplicate and images were taken at 5,000x and 20,000x. Three images taken at random locations at 20,000x were used to measure fiber diameter for each sample. The widths of at least 10 distinguishable fibers per image were measured using AxioVision software. An unbiased method was applied to select the fibers to be measured, which involved drawing a series of diagonal lines across the image [81].

1.5.4 Rheometry: Storage Modulus, Loss Modulus, and Viscosity

Rheological and viscometric measurements were made with a TA Instruments ARG2 Rheometer. Modified from a previous method, a parallel-plate geometry (20mm diameter) at 1.2mm gap height was used on 500 uL gels of the different conditions after 24 hours of gelation [96]. For each condition,

the storage modulus (G') and loss modulus (G'') over frequencies of 0.04-16 Hz were recorded for every gel condition in triplicate. The storage modulus at 1 rad/s or 0.16 Hz was plotted for each condition.

For viscometric measurements, samples were prepared as discussed earlier and kept on ice until experimentation. The rheometer was preheated and maintained at 25°C. Then 200 uL of sample was loaded into the rheometer set at 500 μm gap height such that sample completely filled the gap. Measurements of viscosity were made over a frequency range of 0.1 – 50 Hz as previously reported [94]. The data was best-fit to the following power law:

$$\eta = kf^n \quad (1)$$

In this equation (η) is the complex viscosity and (*f*) is frequency, with (*k*) and (*n*) being constants.

1.5.5 Swelling Ratio

ECM gels of 250 uL for each condition in triplicate were formed in a 48-well plate for 24 hours at 37°C. The gels were transferred to a 12-well plate and were allowed to swell in PBS for 24 hours. The samples were removed, carefully blotted to remove excess surface liquid, and the total swelled weight was measured (W_s). Then the samples were fully dried using a vacuum desiccator overnight and total dry weight was measured (W_d). Swelling ratios were calculated as:

$$Swelling\ Ratio = \frac{W_s - W_d}{W_d} \quad (2)$$

1.5.6 Turbidimetric gelation kinetics

Turbidimetric gelation kinetics were determined through spectrophotometric measurements as previously described [97]. First, a Synergy™ 4 Multi-Mode Microplate Reader (Biotek) was preheated to 37°C. Then 100 uL of each ECM sample, prepared as previously described, was placed into a 96 well plate in triplicate. Absorbance was measured at 405 nm wavelength every minute for 8 hours or until the data plateaued. Absorbance values were averaged within each group, normalized, and plotted over time. From the normalized plot, a linear fit was applied to the linear region of the plot to calculate the half time of gelation ($t_{1/2}$), the lag phase (t_{lag}), and the slope or speed of gelation (S). Half time of gelation was defined as the time when the material reached 50% of the maximum measured absorbance. The lag phase was calculated by finding the time at which the linear-fit was zero for normalized absorbance.

1.5.7 Statistical Analysis

All values were reported as mean ± standard deviation. Samples were run in triplicate and significance accepted at $p < 0.05$. Significance of the data was assessed using either an unpaired student's t-test or a one-way ANOVA with a Tukey or Dunnett's post-test. Complex viscosity in triplicate were averaged and then fit to the power law (1). Significance for complex viscosity was determined by comparing the two concentrations at 10 Hz.

1.6 Acknowledgements

The authors would like to acknowledge Jessica A. DeQuach and Sonya Seif-Naraghi for their technical help, along with the assistance of Carolina Rodgers, in harvesting porcine tissue samples. Also, Ryan Anderson and Patrick Charles of the Nano3 facility for their help with material preparation and scanning electron microscopy. Funding was provided by the National Institutes of Health (NIH) Director's New Innovator Award Program (K.L.C., DP20D004309), which is part of the NIH Roadmap for Medical Research. T.D.J. would like to thank the Powell Foundation for the Powell Fellowship through the Jacobs School of Engineering.

Chapter 1, in full, is a reprint of the material as it appears in Nanotechnology 2011. Lin, Stephen; and Christman, Karen. The dissertation author was the primary investigator and author of this paper.

CHAPTER 2 - Human versus porcine tissue sourcing for an injectable myocardial matrix hydrogel

2.1 Introduction

It was previously shown that the porcine myocardial matrix (PMM) promotes maturation of human embryonic stem cell derived cardiomyocytes and cardiac differentiation of rat cardiac progenitor cells.[27, 28] While this suggests that species specificity may not be critical, it is possible that using a biomaterial sourced from decellularized human tissue could be more desirable and create a better mimic of the native human myocardial ECM. A human derived biomaterial could also bypass some regulatory hurdles since they avoid certain ethical concerns, immunogenic challenges, and issues with xenogeneic disease transfer. In this study, we developed an injectable human myocardial matrix (HMM) hydrogel, derived from decellularized human cadaveric donor hearts, to evaluate whether there are important differences in tissue sourcing when generating a cardiac specific hydrogel for treating MI.

2.2 Results and Discussion

2.2.1 Fabrication of Human Myocardial Matrix Hydrogel

The processing protocol to generate the PMM hydrogel contains 4 main steps: decellularization in SDS, lyophilization, milling, and digestion. Application of this protocol for decellularization of cadaveric human myocardial tissue (Figure 2.1A-C) was insufficient for complete decellularization (Figure 2.1D) and subsequent processing into a hydrogel. Significant DNA content

and lipid content remained (Figure 2.1E-F) leading to a lack of *in vitro* gelation via self-assembly at physiological conditions. Thus, the decellularization process had to be optimized for human tissue including longer decellularization in SDS, and additional DNA and lipid removal steps. This modified decellularization protocol lead to the successful removal of DNA and lipid content as confirmed initially with histology (Figure 2.1G-I). Even after optimizing the protocol for removal of cellular content, including DNA and residual lipids, patient-to-patient variability was observed between the materials. Over fifty percent of the decellularized human hearts did not self-assemble into hydrogels at physiological conditions after digestion, but instead formed a white precipitate after adjusting the pH to 7.4. Thus, this prevented the hearts from being used further, either as an injectable myocardial matrix hydrogel or a liquid substrate coating for cell culture. Similar issues with gelation have not been observed with the PMM and could potentially be correlated to age or species difference for the HMM. The optimized protocol was applied to seven human hearts with patient ages that ranged from 41 to 69 years with an average age of 52 ± 10 years.

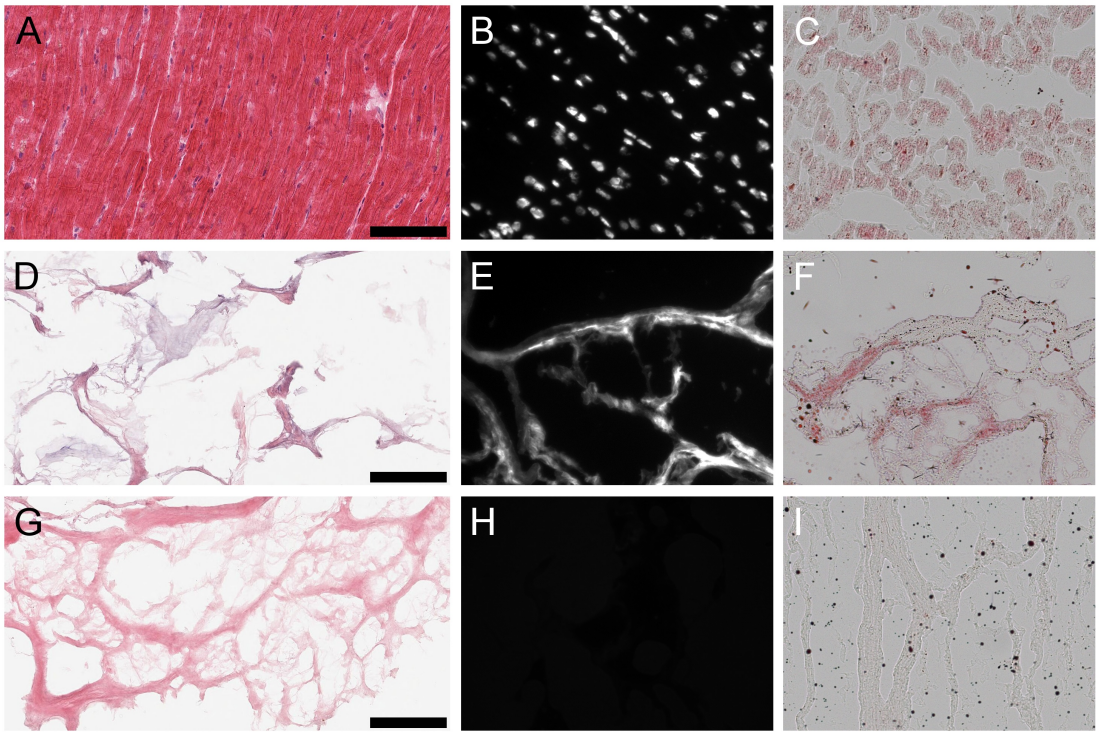

Figure 2.1: Histological analysis of human heart decellularization. Human myocardial tissue fresh (A-C), unsuccessfully decellularized with previously developed porcine myocardial matrix (PMM) protocol (D-F), and fully decellularized with the optimized protocol for human myocardial tissue (G-I). Shown are Hematoxylin and Eosin staining (A, D, G), Hoechst staining for dsDNA (B, E, H), and Oil Red O staining for lipids (C, F, I). The top row shows clear distinguishable nuclei and significant lipid staining in the fresh human myocardial tissue. The middle row indicates incomplete decellularization with positive Hematoxylin in purple, Hoechst, and Oil Red O staining in red. The bottom row shows the optimized human protocol with successful removal of dsDNA and lipid content. Scale bars apply to all images and are 100μm.

Donor age is a significant distinction between the two sources considering tissue was harvested from young adult pigs for PMM, compared to the older human patient donors for HMM. With age there is increased adipose tissue deposition, fibrosis, ECM cross-linking and corresponding stiffening of cardiac tissue.[98-101] These factors could have contributed to the increased challenges observed in decellularization of adult human myocardium. Complete decellularization of a tissue is important for host acceptance and

triggering an appropriate remodeling outcome. The double stranded DNA (dsDNA) content is considered to be a potential indicator of remaining cellular debris and degree of decellularization.[102, 103] Complications with removal of DNA from human myocardium have previously been reported.[104] Preceding decellularization protocols for human myocardium have also needed additional DNA-removal steps beyond the use of decellularization detergents alone.[104, 105] Godier-Furnémont et al. utilized surgical explants of human myocardium as a basis for creating a patch in which the application of DNase and RNase enzymes were also used.[105] Oberwallner et al. used a variety of techniques for decellularizing sheet forms of human myocardium biopsies and removed residual DNA by incubation with fetal bovine serum (FBS).[104] Neither of these protocols investigated the lipid content or removal, potentially due to their use of the ECM scaffold in patch or sheet form. Unlike the porcine hearts, the human hearts contained significant amounts of lipid, which prevented *in vitro* gelation at physiological conditions after digestion. We therefore added an isopropyl alcohol rinse to remove the lipids.

Previous decellularization techniques of human myocardium used small biopsies from living patients,[104, 105] but here we chose to decellularize the entire left ventricle from cadaveric donors who did not present with cardiac disease, but whose hearts were rejected for transplant. This was to achieve larger quantities for application and avoid creating site-specific deficits to healthy patients. The damage inflicted to the myocardium due to tissue biopsies, although small, can never fully regenerate and heal. Additionally,

the patients undergoing open-heart surgery who are candidates for heart biopsies typically have medical conditions involving diseased myocardium. Thus, biopsies are not a clinically relevant approach for sourcing human myocardial tissue to develop an injectable myocardial matrix therapy as diseased myocardium would not contain the same ratio of ECM components.

2.2.2 Biochemical Characterization

To quantitatively characterize the degree of decellularization, the DNA content from both PMM and HMM was isolated and quantified with a PicoGreen assay (Figure 2.2). The PMM had 2.80 ± 0.232 ng of DNA per mg of dry ECM and the HMM had 2.64 ± 0.133 ng DNA per mg of dry ECM, with no significant difference between the two materials. These values are well below a published recommended threshold of 50 ng/mg dry ECM for decellularized biomaterials.[106] Nucleic acid concentrations were also assessed by absorbance using a NanoDrop machine and no measurable signal was detected. It has been previously shown that removal of DNA content is important in decellularized biomaterials for minimizing potentially negative immune responses once implanted.[103, 106] Thus, both biomaterials were successfully decellularized to minimize cellular content within the scaffold.

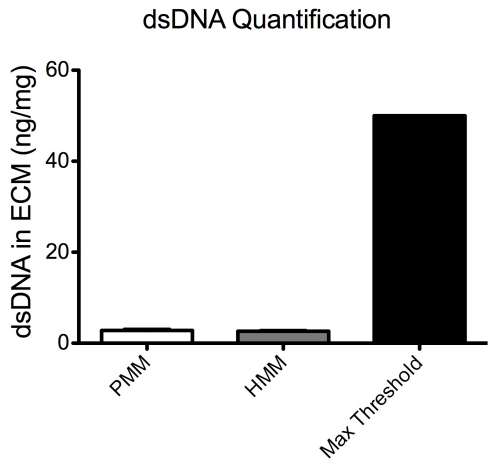

Figure 2.2: Quantification of DNA in the myocardial matrix materials. Plotted is the quantified dsDNA isolated from PMM or HMM per mg of dry ECM. DNA content is very low in both materials and there is no significant difference in the dsDNA content between PMM and HMM.

Next, the sulfated glycosaminoglycan content of the ECM materials was investigated. The sGAG content in these ECM scaffolds is potentially important for their regenerative capacity due to the impact on cellular functions and ability to sequester native growth factors.[107, 108] Utilizing a DMMB assay, the sGAG content of both matrices was quantified and showed a significantly higher level in the PMM compared to HMM (Figure 2.3). This decreased content of sGAG in the human based material potentially correlates with the increased processing that was required for sufficient decellularization. Also, the shift in ECM composition in aging hearts due to increased fibrosis or structural proteins, such as collagen, could be another contributing factor for decreased sGAG content in the HMM.[100, 101]

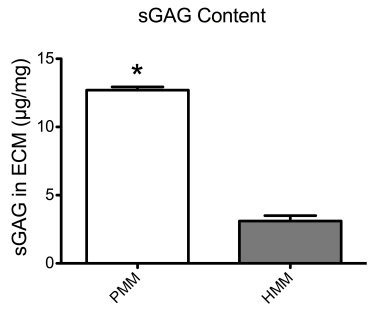

Figure 2.3: Quantification of sulfate glycosaminoglycan (sGAG) content from PMM and HMM as assessed with a DMMB assay. The PMM contains significantly more sGAG than in HMM. *p<0.0001.

The protein and peptide contents for both the PMM and HMM were characterized with mass spectrometry analysis (Table 2.1) and visually assessed with PAGE (Figure 2.4). PAGE showed similar bands to the collagen control as well as numerous other bands over a wide range of molecular weights, indicating the complexity of the materials. The banding patterns of the PMM and HMM were very similar, although there were some slight differences, particularly in the collagen bands. Shifts in ECM composition with increased collagen content and crosslinking have been previously observed in aging myocardium, and in addition to species variation, could account for the differences seen here between HMM and PMM.[98, 100, 101] The diverse protein composition of the PMM and HMM were confirmed with the results from mass spectrometry. The myocardium is known to contain a variety of the structural ECM proteins due to the substantial dynamic requirements of the tissue under regular cyclic contraction.[101] A few additional ECM proteins were identified in HMM compared to PMM (Table 2.1). However, mass spectrometry is not an all-inclusive technique because of

challenges with analyzing a complex ECM sample and with the limitations of current databases. Due to species differences, the materials were analyzed under different peptide databases. There are, however, numerous similarities between the two materials.

Table 2.1: ECM Components Identified from Mass Spectrometry Analysis

	Porcine Myocardial Matrix*	Human Myocardial Matrix
Collagen I	X	X
Collagen II	X	
Collagen III	X	X
Collagen IV	X	X
Collagen V	X	
Collagen VI	X	
Collagen XII		X
Elastin	X	X
Fibrillin - 1	X	X
Fibrinogen	X	X
Fibronectin	X	X
Fibulin - 2		X
Fibulin - 3	X	
Fibulin - 5	X	X
Heparan Sulfate Proteoglycan		X
Laminin	X	X
Lumican	X	
Periostin		X

**Data previously reported.*[27]

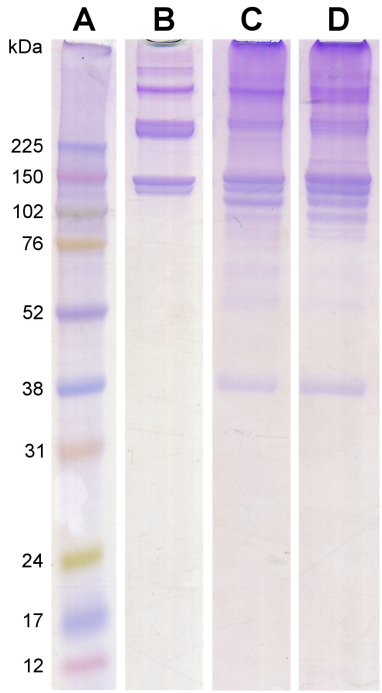

Figure 2.4: PAGE showing molecular weight bands created by the standard ladder (A), rat tail collagen as a control (B), PMM (C), and HMM (D). While PMM and HMM have similar bands and are predominantly collagen, there are some minor differences.

2.2.3 Physical Properties

Complex viscosity of the liquid form of the matrices was measured with parallel plate rheometry (Figure 2.5A). Both matrices had similar linear profiles when plotted on a log-log scale, indicating that they are shear thinning. This is an important characteristic for translation of an injectable biomaterial when a catheter approach is being utilized. A highly viscous or a shear thickening material could potentially impede or hinder delivery through a catheter. *In vitro* gelation and self-assembly of both the PMM and HMM materials was then confirmed and their mechanical properties and nano-scale topography were investigated. Both the HMM and PMM form weak hydrogels

that hold their form. Measured with a parallel plate rheometer, the storage and loss moduli (Figure 2.5B) were both significantly higher for the PMM compared to HMM ($p < 0.0001$). At 1 Hz, the storage modulus of PMM was 6.08 ± 0.38 Pa and the loss modulus was 1.08 ± 0.01 Pa. For the HMM, the storage modulus was 2.53 ± 0.17 Pa and the loss modulus was 0.57 ± 0.04 Pa. This is not surprising, due to the challenges we faced in processing the HMM and the increased issues due to human lipid content within the material, which impedes gelation. From scanning electron microscopy (SEM) it was observed that both matrices self-assembled into very similar complex networks of linear fibers, producing a nano-scale topography (Figure 2.6). This topography is on a scale smaller than a cell and thus can be sensed and manipulated by infiltrating cells upon injection and gelation in host tissue.

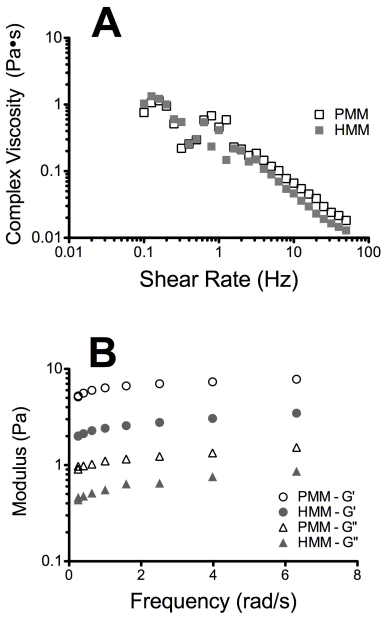

Figure 2.5: Characterization of the mechanical properties using a parallel plate rheometer. Complex viscosity of the liquid form was assessed at 25°C over a range of shear rates (A). Both materials are plotted on a log-log scale and are shear thinning in the liquid form. Storage modulus (G') and loss modulus (G") were measured after incubation for 24 hours at 37°C and example curves over a range of frequencies are plotted (B).

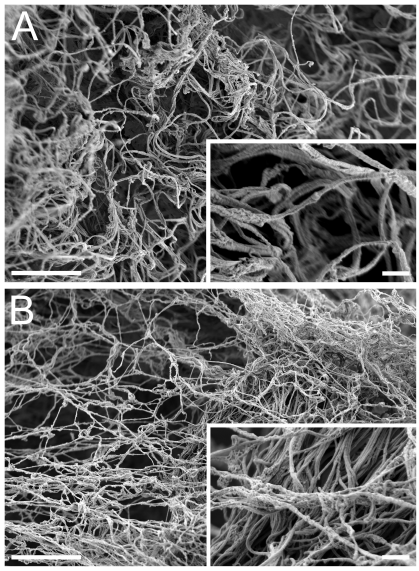

Figure 2.6: Scanning electron microscopy images of both PMM (A) and HMM (B) gels after incubation at 37°C for 24 hours. The materials produced a complex mesh of nano-scale fibers that were formed via self-assembly. Scale bars for the large images are 4μm and the smaller inset images are 400nm.

2.2.4 Bioactivity

After material characterization, the bioactivity of both matrices was tested *in vitro*. Cell culture coatings by adsorption of HMM or PMM were utilized in the following studies. This method of generating ECM cell culture coatings has previously been characterized and shown to produce unique and complex coatings.[27] Either rat aortic smooth muscle cells (RASMCs) or human coronary artery endothelial cells (HCAECs) were cultured for 3 or 5 days on PMM or HMM and relative cellular quantities were measured (Figure 2.7). It has been previously shown that the PMM hydrogel supports infiltration of neovasculature and significant numbers of proliferating cells in rat models.[47, 50] However, *in vitro*, HMM consistently had increased cellular proliferation over the PMM coatings. For both day 3 and day 5, HMM lead to significant

increases in proliferation for RASMCs over PMM coated surfaces. On day 3 the HCAECs had no significant changes in proliferation, but by day 5 the HMM lead to a significant increase again. The differences in proliferation of these vascular cell types is likely not due to species variation since both coatings are xenogeneic for the RASMCs and the HMM is allogeneic for only the HCAECs. However, this trend could be related to the age difference between the material tissue sources. It was previously shown that the degradation products from porcine small intestinal submucosa (SIS) ECM from older tissue sources lead to greater proliferation of perivascular stem cells.[109]

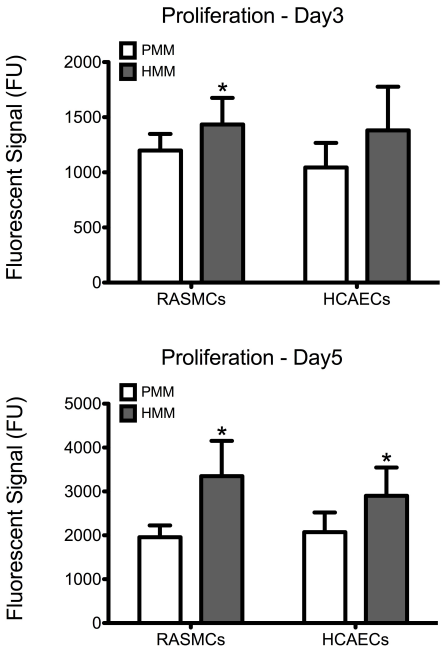

Figure 2.7: Proliferation of rat aortic smooth muscle cells (RASMCs) and human coronary artery endothelial cells (HCAECs) on cell culture coatings of PMM or HMM. Cells were cultured in growth medium for 3 or 5 days and relative proliferation was quantified with a PicoGreen assay. *$p<0.05$.

We also assessed the effect of both matrices on the expression of early cardiac transcription factors with human fetal cardiomyocyte progenitor cells (hCMPCs). After four days of culture on coatings made from gelatin, PMM, or HMM, there was a significant increase in the early cardiac marker Nkx2.5 for the PMM coatings compared to standard culture conditions (Figure 2.8). There was a trend toward an increase for GATA-4 for both myocardial matrices, although this was not statistically significant. In addition, there were no significant differences between the PMM and HMM coatings with regards to gene expression levels and no morphological differences as observed from bright field images (data not shown). The similar levels of gene expression on PMM and HMM for the early cardiac marker, Nkx2.5, and expression of a cardiac sarcomeric protein, troponin T (TnT), were visually confirmed with IHC staining (Figure 2.9). Here we have shown that the biochemical cues from the myocardial matrices enhance early stages of differentiation for hCMPCs, which correlates well with previous studies.[28] French et al. cultured rat c-kit$^+$ cardiac progenitor cells on PMM coatings compared to collagen. By day 2 in culture, they had significant increases in the cardiomyocyte lineage markers Nkx2.5, troponin, and alpha-myosin heavy chain with trends for increases in GATA-4.[28] It has also been shown that the PMM hydrogel supports the infiltration of c-kit$^+$ progenitors,[50] which is hypothesized to play a role in facilitating cardiac regeneration.[29] Overall, there were slight changes in the bioactivity of the two matrices. Only PMM was capable of significantly increasing expression of Nkx2.5, while cells cultured on HMM had increased

proliferation over PMM. These results suggest that PMM may be more effective at promoting differentiation of cardiac progenitors. It is however unclear how these results relate to the *in vivo* setting where both proliferation and differentiation are crucial for myocardial regeneration.

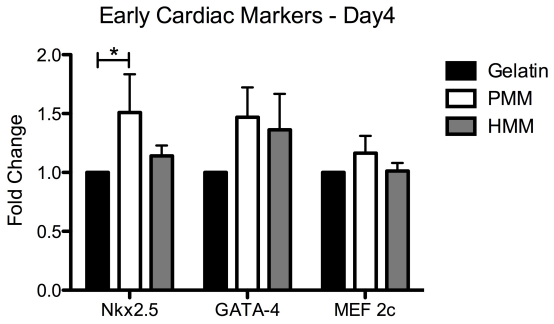

Figure 2.8: RT-PCR for early cardiac markers for human cardiomyocyte progenitor cells (hCMPCs) after culture for four days. Cells were cultured on 2D coatings made from gelatin, PMM, or HMM in proliferation media. *p<0.05.

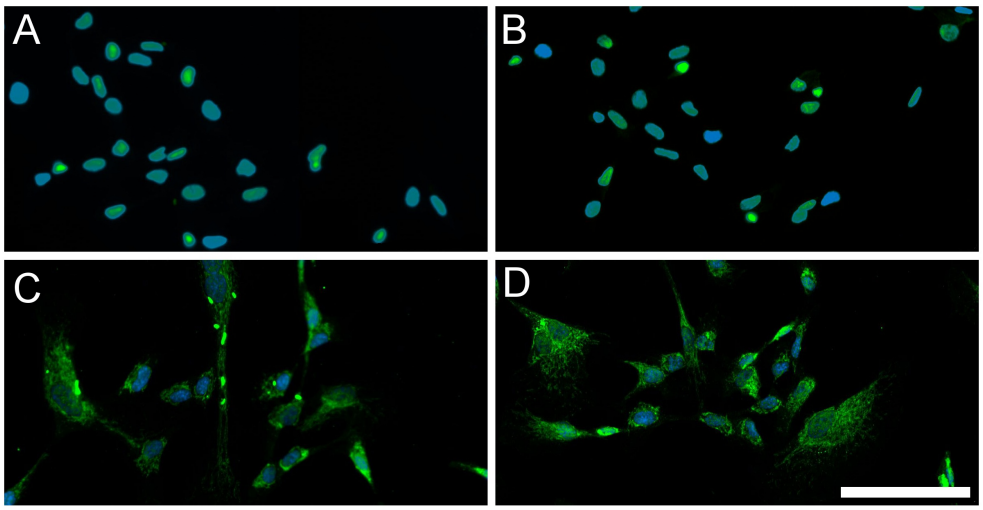

Figure 2.9: hCMPCs after 4 days of culture on PMM (A, C) or HMM (B, D) coatings. Nuclei were stained with Hoechst and shown in blue. An early cardiac marker, Nkx2.5, was stained in green (A, B) and cardiac troponin T was also labeled in green (C,D). The scale bar is 100 μm for all images.

2.2.5 *In Vivo* Gelation

Following the *in vitro* results, the *in vivo* gelation was tested by direct injection into the healthy rat myocardium. Both materials showed successful gelation from the bolus injection within the myocardium (Figure 2.10). It was noted that a similar porous macrostructure of both of the myocardial matrices was observed upon injection, which is potentially important for cellular infiltration.[47] Cellular infiltration, as shown in the previous studies with PMM, is essential for the positive regenerative outcomes that can be stimulated by these injectable biomaterials.[29, 50] After reaching body temperature the matrices self-assemble into a hydrogel form containing a nano-scale ultrastructure. The porous formation is a crucial aspect of these biomaterials, since overly dense materials can block cellular influx and lead to a negative tissue response such as fibrous encapsulation.[110] In a porcine MI model, the influx of cells into the PMM followed by degradation of the biomaterial caused a significant increase in cardiac muscle near the endocardium and a significant decrease in collagen content in the infarcted region.[50]

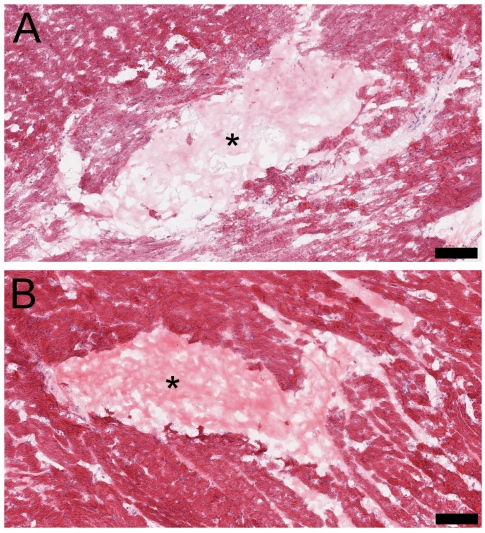

Figure 2.10: In vivo gelation of PMM (A) and HMM (B) in the endocardium of the left ventricle of a Sprague Dawley rat. The injection bolus is indicated with (*) and is surrounded by healthy myocardium. Tissue sections are stained with Hematoxylin and Eosin (H&E). Image scale bars are 100μm.

2.2.6 Assessment of HMM and PMM for Translation

Although some differences between the materials were observed, they contained numerous similarities, such as dsDNA content, ECM protein composition and complexity, shear thinning viscosity profiles, nano-scale fibrous structures from self-assembly, and gelation *in vivo*. Differences between PMM and HMM materials include the methods required for decellularization, sGAG content, collagen banding pattern, and storage and loss moduli. *In vitro* bioactivity analysis indicated that HMM did not cause a significant increase in the expression of Nkx2.5 for hCMPCs like the PMM, but did lead to an increase in proliferation of two vascular cell types over PMM. There are, however, many setbacks that diminish the potential allogeneic benefits of HMM as a viable clinical therapy. For example, complications arose

in producing the HMM material due to significant patient-to-patient variability. Differences between the matrices and complications associated with HMM were potentially correlated to patient age since cadaveric tissue donors were significantly older than the porcine sources. It has also been previously shown that with aging there is an increase in ECM crosslinking and shifts in ECM composition, especially due to increased fibrosis and adipose tissue deposition in aging human hearts.[100, 101] Tissue age for ECM materials has formerly been reported to cause variation in material properties.[109] These changes in ECM due to aging can lead to a decreased regenerative capacity of the corresponding decellularized biomaterials as well.[111] Also, the human hearts collected from this study are relatively rare considering they were rejected as candidates for transplantation and yet were healthy, involving no serious cardiovascular conditions. From a translational and clinical perspective, the variability within the production of the HMM and shifts in ECM composition and bioactivity due to aging indicates that PMM is a more promising choice for the basis of a new therapy. However, HMM still has potential for applications as a cell culture substrate for *in vitro* studies, such as those examining stem cell differentiation and different cardiomyopathies.

2.3 Conclusion

Here we have shown the development of an injectable human myocardial matrix hydrogel that was extensively compared to a previously studied porcine myocardial matrix hydrogel as a potential injectable therapy for

treatment of ischemic cardiomyopathy. Such studies are important due to the increasing evidence of tissue specific cues within ECM constructs for promoting *in vitro* differentiation and *in vivo* regeneration. Increased difficulty in processing and significant patient-to-patient variability of the HMM suggests HMM is not a viable option for translation as an injectable biomaterial therapy; however, the HMM still has potential applications including use as a means for studying diseased human ECM, or as a cell culture coating for differentiation protocols.

2.4 Materials and Methods

2.4.1 Porcine Myocardial Matrix

The porcine myocardial matrix was previously developed and detailed methods are described elsewhere.[47] In brief, fresh porcine myocardial tissue from the left ventricle was isolated and cut into small pieces, rinsed, and then spun in sodium dodecyl sulfate (SDS) solution for 3-5 days with daily solution changes. Once fully decellularized the tissue was rinsed, frozen, lyophilized, and milled into a fine powder. The porcine myocardial matrix powder was then digested with pepsin for 48 hours and brought to physiological conditions for salt and pH. The material was then frozen and lyophilized and kept at -80°C for long-term storage. Before use the material was resuspended with water back to the original concentration of the liquid form of 6 mg/ml.

2.4.2 Human Myocardial Matrix

Human hearts were obtained from organ donors whose hearts could not be used for transplantation under an institutionally approved protocol. The previously published protocol for decellularizing porcine myocardial tissue[47] was not sufficient for decellularizing human myocardial tissue and needed additional modifications. The human heart decellularization protocol starts with the isolation of the entire left ventricle by the removal of epicardial adipose tissue, papillary muscles, chordae tendineae, and valves. The tissue was then cut into small cubes with side lengths of 1-3mm each. The tissue was placed into 1L beakers with 25-35g of tissue per beaker and spun at 125rpm in ultrapure water for 30 minutes. The tissue was then rinsed and spun in 1% (wt/vol) SDS (Fischer Scientific, Fair Lawn, NJ) phosphate buffered saline (PBS), and 0.5% Penicillin Streptomycin (PS) of 10,000 U/mL(Gibco, Life Technologies, Grand Island, NY) for 2 hours. The solution was then replaced daily for 6-8 days until the tissue was white in color. The tissue was then rinsed by spinning in water for 2 hours and placed into isopropyl alcohol (IPA) (Fisher Scientific, Fair Lawn, NJ) for 12-24 hours for lipid removal. Next, the tissue was rinsed twice in water for 15 minutes each and divided into 50mL conicals with a DNase/RNase solution. The DNase/RNase solution consists of 40 U/mL DNase (Sigma-Aldrich, St. Louis, MO) and 1 U/mL RNase A (Qiagen, Hilden, Germany) in 40mM tri-hydrochloric acid (HCl), 6mM magnesium chloride, 1mM calcium chloride, and 10mM sodium chloride at pH 7.4. The conicals with tissue in the

DNase/RNase solution were incubated at 37°C on a shaker plate for 24 hours. Following incubation the tissue was rinsed with water and placed back into the SDS in PBS with PS and spun for 24 hours at 125rpm. The tissue was then briefly shaken in 0.001% Triton X-100 solution (Sigma-Aldrich, St. Louis, MO), then spun in the same solution for 30-45 minutes and finally spun in water again for 24 hours. Then the tissue was shaken in water, frozen, lyophilized and milled using a Wiley® Mini-Mill into a fine powder through a #40 sieve. Two decellularized human hearts were combined for all analysis and testing. The human material was then treated with the same methods as the porcine myocardial matrix powder for all further processing.

2.4.3 Material Characterization

2.4.3.1 Histological Analysis

Tissue samples were fresh frozen before and after decellularization for histological analysis. Then 10μm cryosections were stained with Hematoxylin and Eosin (H&E), Hoechst, and Oil Red O. Slides were imaged with Leica Aperio ScanScope® CS^2, Carl Zeiss Observer D1, and Zeiss Imager A1 respectively.

2.4.3.2 Material Composition

DNA was isolated from the HMM and PMM using a NucleoSpin® Tissue kit (Macherey-Nagel, Duren, Germany). Nucleic acid content was quantified with a Thermo Scientific NanoDrop 2000c spectrophotometer. The

dsDNA content was then quantified (n=3) with a Quant-iT™ PicoGreen® dsDNA Assay Kit (Invitrogen, Eugene, OR). The sulfated glycosaminoglycan (sGAG) content was quantified (n=3) with a DMMB assay.[112] The DMMB protocol was implemented as previously described on the liquid form of the matrices. The DMMB working solution was made fresh each time without dilution and Chondroitin Sulfate (Sigma-Aldrich, St. Louis, MO) was used as the standard. Protein fragment size was characterized using a NuPAGE 12% Bis-Tris Gel (Novex, Life Technologies, Carlsbad, CA). Protein composition was characterized using mass spectrometry. The samples were initially prepared as previously reported.[113] The recovered peptides from the FASP method were then extracted using Aspire RP30 desalting columns (Thermo Scientific) before injection into the mass spectrometer. Trypsin-digested peptides were analyzed by liquid chromatography (LC)-MS/MS with nanospray ionization. All nanospray ionization experiments were performed using a QSTAR-Elite hybrid mass spectrometer (ABSCIEX) interfaced to a nanoscale reversed-phase high-pressure liquid chromatography (Tempo) using a 10 cm-180 ID glass capillary packed with 5-µm C18 Zorbax™ beads (Agilent). The buffer compositions were as follows. Buffer A was composed of 98% H_2O, 2% ACN, 0.2% formic acid, and 0.005% TFA; buffer B was composed of 100% ACN, 0.2% formic acid, and 0.005% TFA. Peptides were eluted from the C-18 column into the mass spectrometer using a linear gradient of 5–60% Buffer B over 60 min at 400 ul/min. LC-MS/MS data were acquired in a data-dependent fashion by selecting the 6 most intense peaks with charge state of 2 to 4 that

exceeds 20 counts, with exclusion of former target ions set to "120 seconds" and the mass tolerance for exclusion set to 100 ppm. Time-of-flight MS were acquired at *m/z* 400 to 1800 Da for 0.5 seconds with 12 time bins to sum. MS/MS data were acquired from *m/z* 50 to 2,000 Da by using "enhance all" function and 24 time bins to sum, dynamic background subtract, automatic collision energy, and automatic MS/MS accumulation with the fragment intensity multiplier set to 6 and maximum accumulation set to 2 s before returning to the survey scan. Peptide identifications were made using Mascot® (Matrix Sciences) and paragon algorithm executed in Protein Pilot 3.0 (ABSCIEX).

2.4.3.3 Viscosity and *In Vitro* Gelation Characterization

The complex viscosities of the resuspended liquid form of both matrices (n=3) were measured with TA Instruments ARG2 Rheometer using a 20mm parallel plate geometry as previously described.[114] Gelation *in vitro* was confirmed by incubation of the liquid form at 37°C for 24 hours. Gels of 500µL in volume were assessed (n=3) for storage (G') and loss moduli (G") as previously described.[114] The storage moduli and loss moduli were assessed over a range of frequencies. For statistical analysis the moduli values at 1Hz were compared.

Gels were imaged for nano-scale fiber formation with scanning electron microscopy (SEM) similar to previously described methods.[114] Samples of 100µL volume were gelled in a 96-well plate for 24 hours at 37°C. The gels

were then fixed in a solution of 4% paraformaldehyde and 4% glutaraldehyde for 24 hours. Then the gels were dehydrated with a series of gradated ethanol rinses. Fixed and dehydrated hydrogels were loaded into Teflon sample holders and processed in an automated critical point drier (Leica EM CPD300, Leica, Vienna), which was set to perform 40 exchange cycles of CO_2 at medium speed and 40% stirring. The fill and heating steps were performed at slow speed, while the venting step was performed at medium speed. Mounted samples were then sputter coated (Leica SCD500, Leica, Vienna) with approximately 7nm of platinum while being rotated. The samples were then imaged on a FE-SEM (Sigma VP, Zeiss Ltd., Cambridge, UK) at 0.6kV using the in-lens SE1 detector.

2.4.4 In Vitro *Cell Culture*

2.4.4.1 ECM Cell Culture Coatings

Cell culture coatings from PMM or HMM were made fresh each time by re-suspending the ECM in 0.1M acetic acid to a concentration of 1 mg/ml. The solution was then incubated on the tissue culture plastic for 1 hour at 37°C. After incubation the solution was removed and the surface was rinsed 2-3 times with PBS before cells were plated as previously reported.[27]

2.4.4.2 Proliferation of Vascular Cells

Two relevant vascular cell types were used for this study: rat aortic smooth muscle cells (RASMCs) and human coronary artery endothelial cells

(HCAECs). The RASMCs were isolated as previously described[47, 115] and cultured on collagen coated plates during expansion in growth media of Dulbecco's Modified Eagle's Medium (DMEM) (Corning Cellgro, Manassas, VA) with 10% Fetal Bovine Serum (FBS) (Sigma-Aldrich, St. Louis, MO) and 1% Penicillin Streptomycin (PS) (Gibco, Life Technologies, Grand Island, NY). The HCAECs were purchased (Cell Applications Inc, San Diego, CA) and cultured in MesoEndo Endothelial cell media (Cell Applications). The wells of a polystyrene 96-well microtiter plate were coated with either PMM or HMM (n=8) as described above. On day 0, a total of 5×10^2 RASMCs or HCAECs were seeded into each well. Then, 24 hours later the media was changed and wells were rinsed twice with PBS. Every two days, the media was exchanged for fresh media and cells were rinsed twice with PBS. Following 3 and 5 day time point intervals, relative cell proliferation was measured by quantifying dsDNA content in each well with Quant-iT^{TM} PicoGreen® dsDNA Assay Kit (Invitrogen, Eugene, OR).

2.4.4.3 Human Cardiomyocyte Progenitor Cells

Human fetal cardiomyocyte progenitor cells (hCMPCs) were isolated from tissue harvested under standard informed consent procedures and prior approval of the ethics committee of the University Medical Center Utrecht. All cell studies were done in compliance with the University of California, San Diego Institutional Review Board. hCMPCs were isolated from human fetal hearts by selection with Sca-1^+ magnetic bead sorting and cultured on 0.1%

gelatin in growth media during expansion and passaged as previously described.[116, 117] Growth media for these studies consisted of 25% EGM-2 (3% EGM-2 single quotes (Cambrex, cat. no. CC-4176) in EBM-2 (Cambrex, cat. no. CC-3156)) and 75% M199 (BioWhittaker, cat. no. BE12-119F), 10% FBS (Hyclone, cat. no. CH30160.30), 1x MEM non-essential amino acids (BioWhittaker, cat. no. BE13-114E) and 1% penicillin/streptomycin (Sigma, cat. no. P4458). For gene expression analysis and immunohistochemistry, the hCMPCs were plated in 6-well plates with 70,000 cells (P7-11) per well on either gelatin, PMM, or HMM coatings in growth media. Cells on day 2 were either analyzed or passaged and re-plated on new coatings, and then analyzed at day 4. All experiments were done in triplicate using cells from four separate donors that were studied in parallel (n=4).

2.4.4.4 RT-PCR on hCMPCs

The hCMPCs RNA was isolated by NucleoSpin RNAII column (Macherey-Nagal, cat no. 740955.250). The RNA concentration and purity was then measured using a Thermo Scientific NanoDrop 2000c spectrophotometer. The cDNA was synthesized using iScript cDNA synthesis Kit (cat. No. 170-8891, Bio-Rad) and quantitative RT-PCR amplification was detected in a MyIQ single-color real-time polymerase chain reaction system using iQ SYBR Green Supermix (170-8884, Bio-Rad). Primers used included the following: GATA-4 (fw – GTTTTTTCCCCTTTGATTTTTGATC, rv – AACGACGGCAACAACGATAAT), hNkx2.5 (fw –

CCCCTGGATTTTGCATTCAC, rv – CGTGCGCAAGAACAAACG), MEF2c (fw – TCGGGTCTTCCTTCATCAG, rv – GTTCATCCATAATCCTCGTAATC), and the house keeping gene GAPDH (fw – CTCTGACTTCAACAGCGACA, rv – TCTCTCTCTTCCTCTTGTGC).

2.4.4.5 IHC on hCMPCs

Cells were fixed with 4% PFA for 15 minutes, permeabilized with 0.1% Trion X-100, 1% BSA in PBS for 10 minutes and blocked with 10% goat serum in PBS for 1 hour. The following primary antibodies were then separately incubated overnight on the samples at 4°C in 1% goat serum: Nkx2.5 (Santa Cruz, sc-14033 at 1:100) and TnT (Santa Cruz, sc-20643 at 1:100). The cells were then incubated for 1 hour at room temperature with a goat anti-rabbit secondary (Alexa488, A11008) in 0.01% Triton X-100, 0.1% BSA in PBS and counterstained with Hoechst.

2.4.5 *In Vivo* Gelation

All experiments in this study were performed in accordance with the guidelines established by the committee on Animal Research at the University of California, San Diego, and the American Association for Accreditation of Laboratory Animal Care. *In vivo* gelation was tested in female Sprague Dawley (SD) rats. Injections were performed as previously described.[47, 118] Both the human and porcine myocardial matrices resuspended in liquid form at 6 mg/ml concentration were separately injected three times each with a

volume of 50μL into the left ventricular free wall. After 20 minutes the animals were sacrificed, then the hearts were harvested and rapidly frozen in OCT. Short axis sections of 10μm were taken and stained with H&E to confirm material spread and gelation within the wall of the heart.

2.4.6 Statistical Analysis

All graphs with error bars are plotted as mean ± standard deviation (SD) and studies were done in triplicate unless otherwise indicated. Significance was determined with an unpaired student's *t*-test or a one-way ANOVA using a Tukey post-hoc test with a $p < 0.05$.

2.5 Acknowledgments

The authors would like to thank Dr. Ghassemian and Matt Joens for their technical expertise in mass spectrometry and scanning electron microscopy, respectively. The authors would also like to thank Lifesharing for their assistance in obtaining the human cardiac tissue. Funding for this study was provided by the NIH Heart, Lung, Blood Institute 5R01HL113468 (KLC) and the Leducq Foundation Transatlantic Career Development Award (RG). TDJ received funding during this project from the NSF as a graduate student fellow, the NHLBI as a training grant recipient, and as a Powell Fellow from the Powell Foundation. KLC is co-founder, board member, and holds equity interest in Ventrix, Inc.

Chapter 2, in full, is a reprint of the material as it appears in Biomaterials Science 2014. DeQuach, Jessica A.; Gaetani, Robert; Ungerleider, Jessica; Elhag, Dean; Nigam, Vishal; Behfar, Atta; Christman, Karen. The dissertation author was the primary investigator and author of this paper.

CHAPTER 3 – Humanized Mouse Model as a Tool for Testing the Human Immune Response to Xenogeneic and Allogeneic Decellularized Biomaterials

3.1 Introduction

While both xenogeneic and allogeneic sources for decellularized ECM have been widely used to date, preclinical understanding of these scaffolds is based off the immune response of these matrices in rodents and a few large animals [29, 119, 120]. Given the difficulties with obtaining sequential biopsies in patients, no one has thoroughly monitored or understood the human immunes response to these materials. Although connected evolutionarily, rodents typically used for biocompatibility testing do not fully mimic the human immune system. When compared to the closest evolutionary relatives, differences have been observed with human T-cells including a decrease in Siglec expression and T-cell hyperactivity leading to a unique human immune response [121]. Even non-human hominids have various biomedical differences from humans [122]. Thus, the animal models typically used in preclinical studies do not properly mimic all aspects of the human immune response. This combined with our incomplete understanding of the human immune system as a whole has lead to removal of several very well characterized materials from the market [123, 124].

One method for preclinical assessment of the human immune response is the use of a humanized mouse model. This model has been significantly improved over the last 20 years and has become a valuable model for mimicking the human immune response [125-127]. In particular, the humanized

mouse model developed by implantation of human fetal thymus tissue and injection of human $CD34^+$ fetal liver cells into an immune compromised NSG mouse has shown to be robust and contain human T-cells, B-cells, and dendritic cells, allowing for the ability to reject xenogeneic tissue [128]. This model has been used extensively for studying autoimmune disease, virus infections, xenogeneic transplantation [127], and more recently allogeneic stem cell transplantation [129]; however, it has yet to be exploited in the field of biomaterials. In this study, we utilized this model to assess the human immune response to decellularized ECM biomaterials, specifically injectable hydrogels derived from either porcine or human myocardium, which were initially developed to treat myocardial infarction [29, 47, 50, 130]. We hypothesized that the model would demonstrate a different immune response to human vs. xenogeneic ECM, unlike the wild type rodent model, thereby providing a new preclinical tool for more accurately determining the immune response to biomaterials prior to clinical translation.

3.2 Results

3.2.1 Study Design

We assessed two hydrogels, a porcine myocardial matrix (PMM) and a human myocardial matrix (HMM) in the humanized model (Hu-mice) versus age matched wild type Balb/c mice. Both biomaterials are derived from decellularized myocardium, are processed into injectable liquids that self-assemble into hydrogels with nanofibrous architecture (Figure 3.1), and were

previously shown to have similar structure and mechanical properties (~2.5-6 Pa storage modulus) [130]. We confirmed that this processing substantially removes the alpha-Gal epitope in the porcine derived material (images not shown). As a control we also examined these materials in age matched NSG mice, which lack T-cells, B-cells, and natural killer cells, and are used to create the Hu-mice. Each material was injected subcutaneously, which a common delivery route for ISO standard biocompatibility tests, and at least eight different injections (n=8-12) were analyzed histologically one-week post injection. One week post-injection was selected as it is beyond the initial neutrophil infiltration stage and into when polarized macrophages and lymphocytes are present within the region [131]. Longer time points were not investigated here since these biomaterials are degradable and typically only persist for a couple weeks *in vivo* [29].

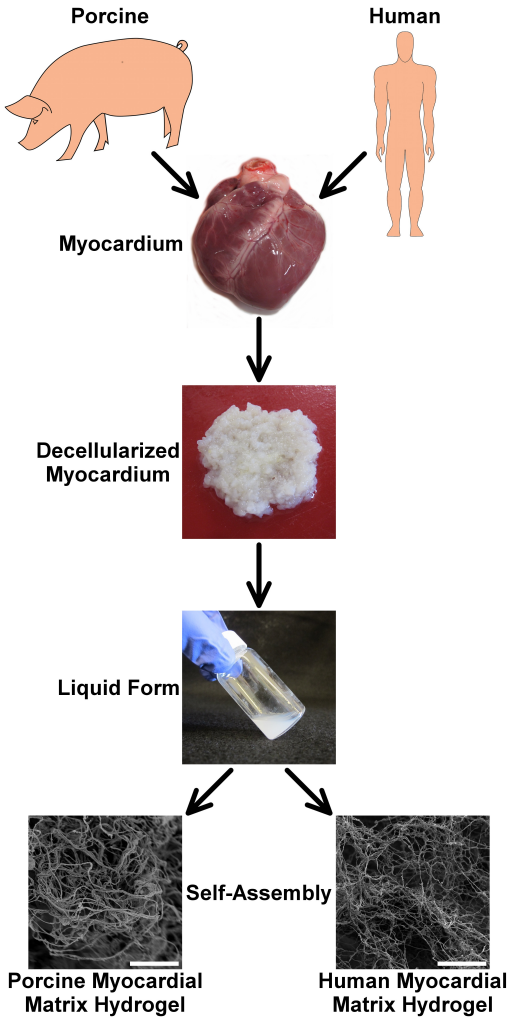

Figure 3.1: Injectable myocardial matrix hydrogels derived from porcine or human tissue. The biomaterials were derived from either fresh porcine or human cadaveric left ventricular myocardium. The tissues were decellularized and then processed into an injectable form by enzymatic digestion. Once in the liquid form, the materials self-assemble into myocardial matrix hydrogels at physiological conditions. The hydrogels contain a similar nano-scale architecture as shown via SEM images. Scale bars are 5 μm.

3.2.2 Histology and Cellular Infiltration

Paraffin embedded samples were sectioned and stained with Hematoxylin and Eosin (H&E) for histological analysis (Figure 3.2A). Both decellularized biomaterials, PMM and HMM, showed moderate to minimal

infiltration of mononuclear cells in all three animal models. No foreign body giant cells or other signs of material rejection were observed. Cellular infiltration into each biomaterial was quantified; both the injection as a whole and also the core region were analyzed for cellular density (Figure 3.2B-E). The densities of the infiltrating cells into the whole biomaterial were lower for both biomaterials in the Hu-mice when compared to wild type Balb/c animals (Figure 3.2B, C). This is to be expected since it is known that the model produces a moderate response compared to a fully competent or wild type immune system [132]. Differences between xenogeneic and allogeneic responses were observed in terms of cellular density and infiltration into the core of the biomaterial (Figure 3.2D, E). Injection of PMM into the Hu-mice and Balb/c mice, which is xenogeneic ECM in both models, resulted in a similar degree of cell infiltration into the core (Figure 3.2D); however, the HMM material had significantly less infiltration into the core region when implanted in the Hu-mice group as an allogeneic material compared to the Balb/c group where it is xenogeneic (Figure 3.2E). Finally, both materials had similar responses in the immunocompromised NSG animals with significantly less cellular infiltration into the core of either material when compared to the Balb/c animals (Figure 3.2D, E).

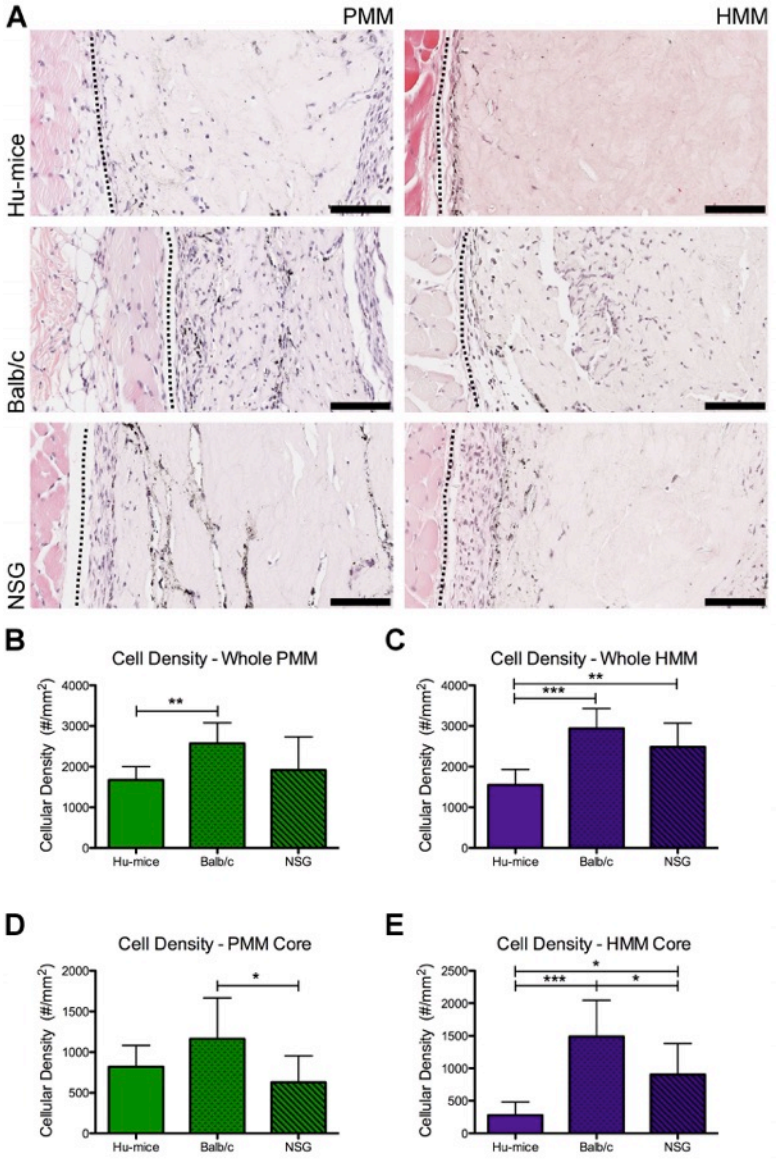

Figure 3.2: Representative Hematoxylin and Eosin (H&E) staining. (A) Images represent local tissue immune response one week after subcutaneous injections of porcine myocardial matrix (PMM) or human myocardial matrix (HMM) in a humanized mouse model (Hu-mice), an immune competent Balb/c mouse, or an immune compromised NOD scid gamma (NSG) mouse. Quantification of cellular density for the whole biomaterial (B, C) and infiltration into the core (D, E) of the biomaterial for each group is also shown (*p<0.05, **p<0.01, ***p<0.001). Data is presented as mean ± SD. On the left of each image is the panniculus carnosus muscle layer of the dermal tissue and on the right is the injected biomaterial. The biomaterial and dermal tissue are separated by a black dotted line. Scale bars (100 μm).

3.2.3 Minimal Human Cellular Infiltration for Allogeneic ECM

After the investigation of the PMM and HMM biomaterials by H&E staining and histological analysis we then investigated the degree of human cellular infiltration for the Hu-mice groups. First, immunohistochemistry was used to confirm the presence of human cells in the model by staining the spleen (images not shown), and that transmigration of human cells from the circulatory system into the peripheral tissue occurred for both materials (Figure 3.3A). A notable difference in the prevalence and location of human nuclei between PMM and HMM was observed. Of the cells within the PMM biomaterial, approximately 25% were human. Whereas, in the HMM biomaterial only about 9% of the cells were labeled positively for human nuclei (Figure 3.3B). Not only was there a shift towards a higher percentage (p=0.055), but this was reflected in an increase in human nuclei density as well (p=0.067) (Figure 3.3C). Upon investigating infiltration into the core of the biomaterial, there was a trend for higher percentage of human cells and a significant increase in he density of human cells in PMM compared to HMM (Figure 3.3D,E). Thus, a significantly different response in human cellular infiltration was observed for the allogeneic HMM material compared to the xenogeneic PMM material in the Hu-mice.

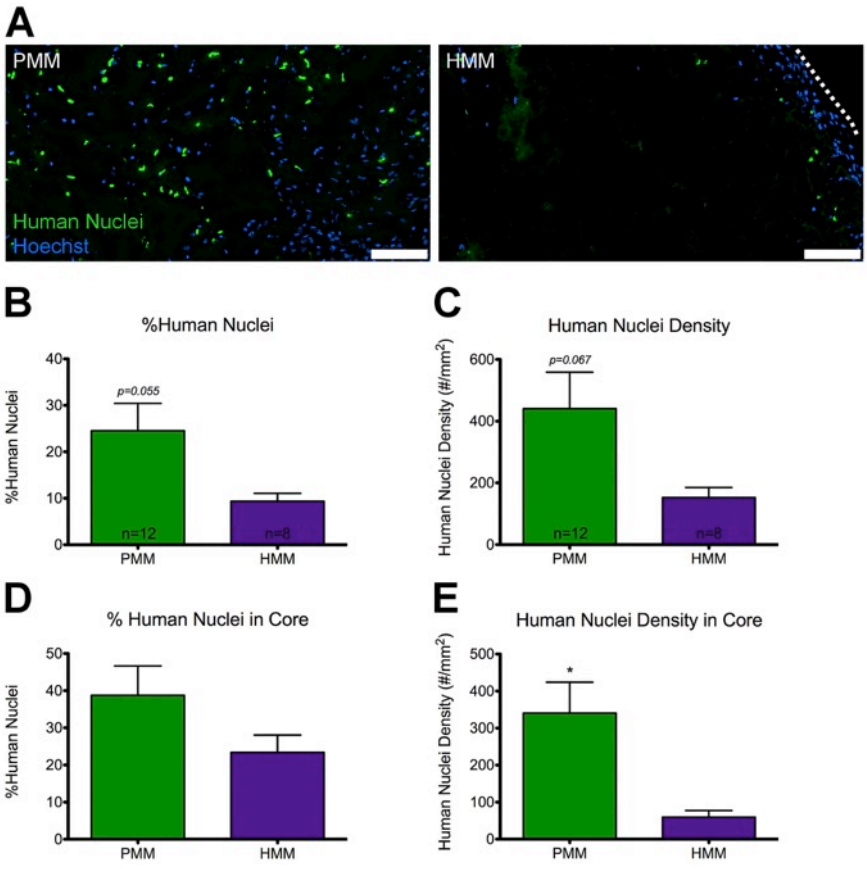

Figure 3.3: Human nuclei infiltration for PMM and HMM in Hu-mice. (A) Representative images of Hoechst stained nuclei (blue) and human nuclei staining (green) of Hu-mice injected with either PMM or HMM. Dotted white line indicates edge of HMM biomaterial. Quantification of percent and density of human nuclei in the biomaterial (B, C) and into the core (D, E) of the biomaterial (*$p<0.05$). Scale bars (100 μm).

3.2.4 T-Cell and Macrophage Infiltration into Xenogeneic ECM

The Hu-mice model showed significant differences in the number of infiltrating human cells between the allogeneic and xenogeneic materials, but there could also be shifts in the different types of recruited immune cells. Both T-cells and macrophages have been shown as important cell types for characterizing the immune response to ECM biomaterials. Thus, here we utilized immunohistochemistry to visual cell infiltration and spatial resolution of

T-helper cells, cytotoxic T-cells and macrophages in the PMM and HMM materials in the Balb/c and Hu-mice. In the Balb/c mice, both T-helper cells ($mCD3^+mCD4^+$) and cytotoxic T-cells ($mCD3^+mCD8^+$) were detected in the biomaterials (Figure 3.4) and positive staining was confirmed in spleen tissue as well (images not shown). T-helper cells were found in small clusters around the perimeter of the biomaterials and occasionally infiltrated into the core. Cytotoxic T-cells were rarely identified in either PMM or HMM injected groups. Macrophages were identified and evenly dispersed around each biomaterial and also infiltrated into the core of both materials. Given the larger numbers of infiltrating cells in the Balb/c model, presence of each of these cell types was further confirmed with flow cytometry later in the study. Similar patterns of infiltration of macrophages, human T-helper cells, and human cytotoxic T-cells, the latter two of which were identified by co-staining with a human specific antibody, were also observed with PMM in the Hu-mice (Figure 3.4). In contrast, there was limited infiltration and presence of T-cells and only a thin layer of macrophages present around the perimeter of the biomaterial in the allogeneic response observed for HMM in Hu-mice (Figure 3.4). Spleens were also utilized as a positive control for staining of each human specific T-cell antibody (images not shown). This supports the histological data and quantitative cellular infiltration data showing limited cellular response to the allogeneic material in contrast to the xenogeneic material in the Hu-mice.

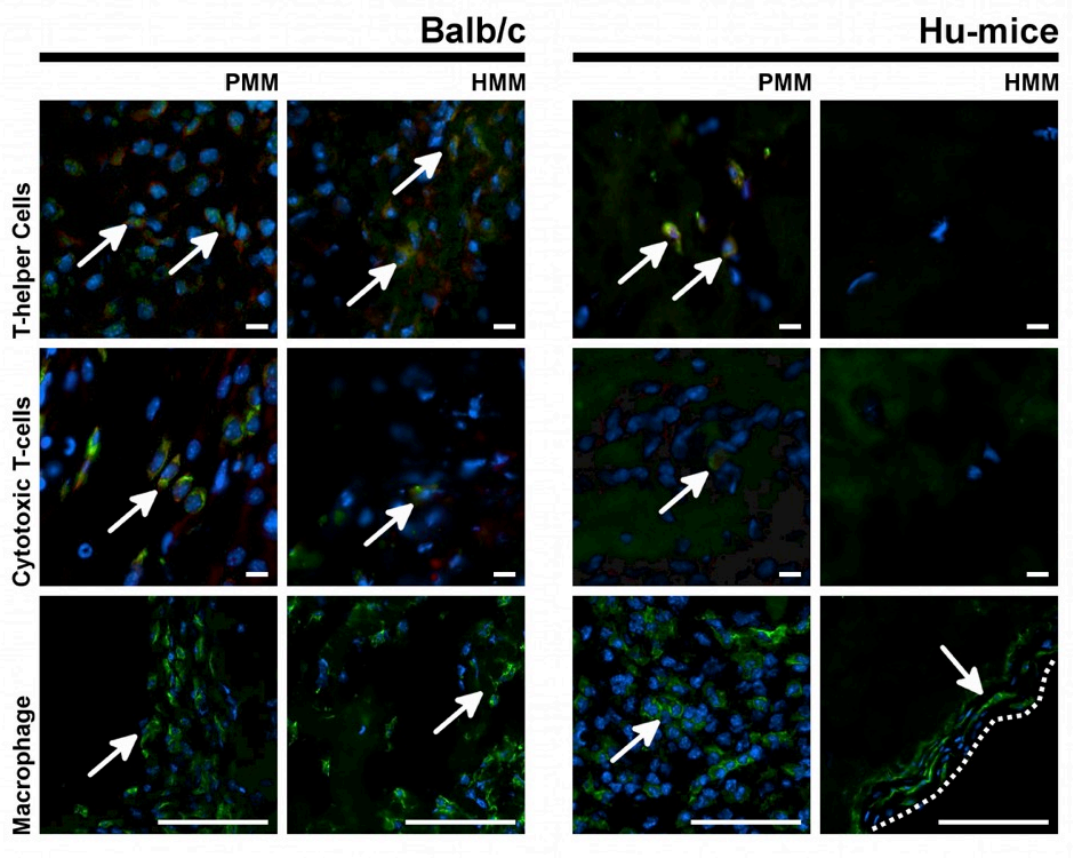

Figure 3.4: Immunohistochemistry images for T-helper Cells, Cytotoxic T-cells and Macrophages in PMM or HMM in Balb/c or Hu-mice. Hoechst staining was used to label cellular nuclei (blue). T-helper cells were labeled by co-staining with CD3 (red) and CD4 (green). Cytotoxic T-cells were labeled by co-staining with CD3 (red) and CD8 (green). Macrophages were labeled with a pan-macrophage antibody (green). Dotted white line indicates edge of biomaterial. Small scale bars (10 μm) and large scale bars (100 μm).

3.2.5 ECM Biomaterials Favor Pro-remodeling Immune Cell Polarization

T-helper cells and macrophages are known to polarize and show dramatically different phenotypes depending on their local niche [133, 134]. For example, infiltrating T-helper cells that are $CD4^+$ can be associated with not only a pro-remodeling response, but can be connected with graft rejection as well [135], and thus we wanted to more fully characterize T-helper cell polarization. T-helper cells can be further divided into two sub-cell types

called Th1 and Th2 [134, 136]. To quantify the degree of T-helper cell polarization, qRT-PCR was applied to all of the treatment groups from the Balb/c animals including the NDM material as a control, and the PMM group in the Hu-mice model. The NDM control group was not repeated in the Hu-mice model since it has previously been shown to have the capacity for xenogeneic tissue rejection [128] and the HMM group was not included due to the lack of cellular infiltration into the biomaterial as observed and quantified with histology and immunohistochemistry. Polarization towards the Th2 phenotype was measured by comparing the ratio of expression of GATA3 (Th2) to TBX21 (Th1) for the PMM and HMM groups compared to the non-decellularized matrix (NDM) control [136]. Previous characterization of Th1/Th2 phenotype expression for an another ECM derived material was done in comparison to a xenogeneic graft rejection as a control [137]. Here we present a similar approach in the use of NDM as an injectable control, which elicits a negative immune response that favors the Th1 phenotype. PMM in both Balb/c and Hu-mice showed significant increases towards the Th2 cell type lineage and HMM also showed a similar trend compared to NDM (Figure 3.5A). The polarization of T-helper cells towards the Th1 or Th2 phenotypes have been correlated to macrophage polarization [138, 139]. Macrophage polarization is plastic and complex [140-142], but is often simplified into M1 and M2 phenotypes [143]. A ratio of related genes expressed in M1 (iNOS) and M2 (Arg-1) can be used to measure macrophages polarization with qRT-PCR [144]. By one week after injection of the biomaterials, both PMM and HMM in Balb/c mice showed a

shift towards the M2 phenotype and PMM in Hu-mice had a significant shift towards M2 when compared to the NDM control (Figure 3.5B). Thus, both biomaterials promoted polarization towards the Th2 and M2 pro-remodeling phenotypes in Balb/c mice; this shift also occurred with PMM in the Hu-mice.

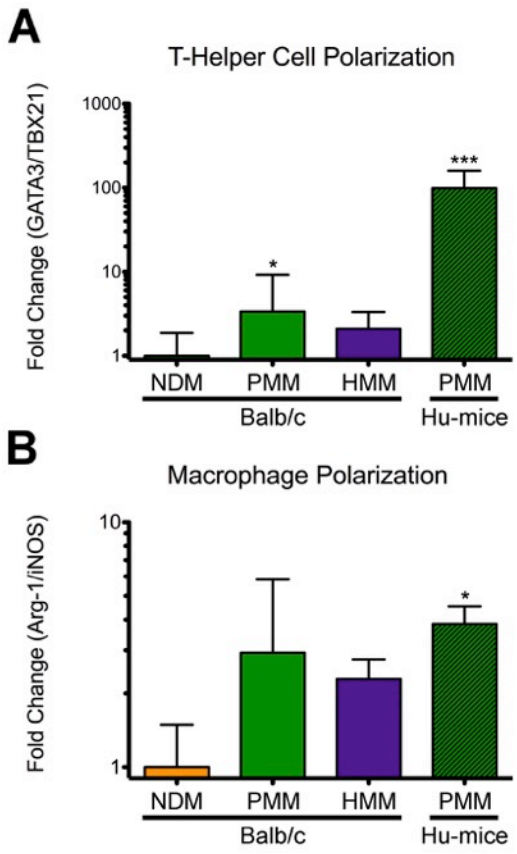

Figure 3.5: T-helper Cell and Macrophage polarization. qRT-PCR was utilized to determine the degree of polarization of T-helper cells and macrophages compared to the NDM in Balb/c control group. (A) T-helper cell polarization of Th2/Th1 was measured as fold change ratio of GATA3/TBX21 gene expression. (B) Macrophage polarization of M2/M1 was measure as fold change ratio of Arg-1/iNOS gene expression (*p<0.05, ***p<0.001).

3.2.6 ECM Biomaterials Favor T-Helper Cell Infiltration

After confirming the presence of macrophages, T-Helper cells and lack of Cytotoxic T-cells, and characterizing their polarization we next wanted to directly quantify the relative percentage of each cell type within and around the

biomaterial in the local host tissue using flow cytometry. Flow cytometry was implemented only on the Balb/c groups to characterize the xenogeneic immune response cellular profile. This method of approach was selected since there was limited cellular infiltration for the allogeneic response in the Hu-mice for HMM. Thus, characterizing the immune response of the decellularized materials in the Balb/c compared to the NDM control was implemented to more fully understand xenogeneic ECM immune response. In Balb/c animals, injections of each biomaterial were harvested after one week. The biomaterial and neighboring tissue were digested to isolate a single cell suspension for labeling and quantification using flow cytometry. Although their use has been debated, isotype controls were utilized as a negative control in this study due to high amounts of cellular debris still present after digestion and to help remove non-specific antibody binding from the measured signal [145, 146]. The results of this analysis in the immune competent animals are presented in Figure 3.6. In Figure 3.6A are representative plots of the blank or unlabeled cells and cells isolated from each biomaterial treatment group as labeled for macrophages (mCD68+), T-Helper cells (mCD3+mCD4+), and Cytotoxic T-cells (mCD3+mCD8+). Both CD4 and CD8 markers alone are known to provide clear strong signal with good positive T-cell population identification and were co-stained with CD3, a pan T-cell marker [146]. Cells were also labeled for B-cells (mCD19+) but were not detected in the isolated region. The averages for each group are presented in Figure 3.6B. The percentage of macrophages or T-Helper cells of the total

isolated population did not vary between the groups, but a significant shift in the NDM group towards Cytotoxic T-cells was consistently observed. Thus, the decellularized xenogeneic biomaterials favored a T-Helper cell population over Cytotoxic T-cells (Figure 3.6C).

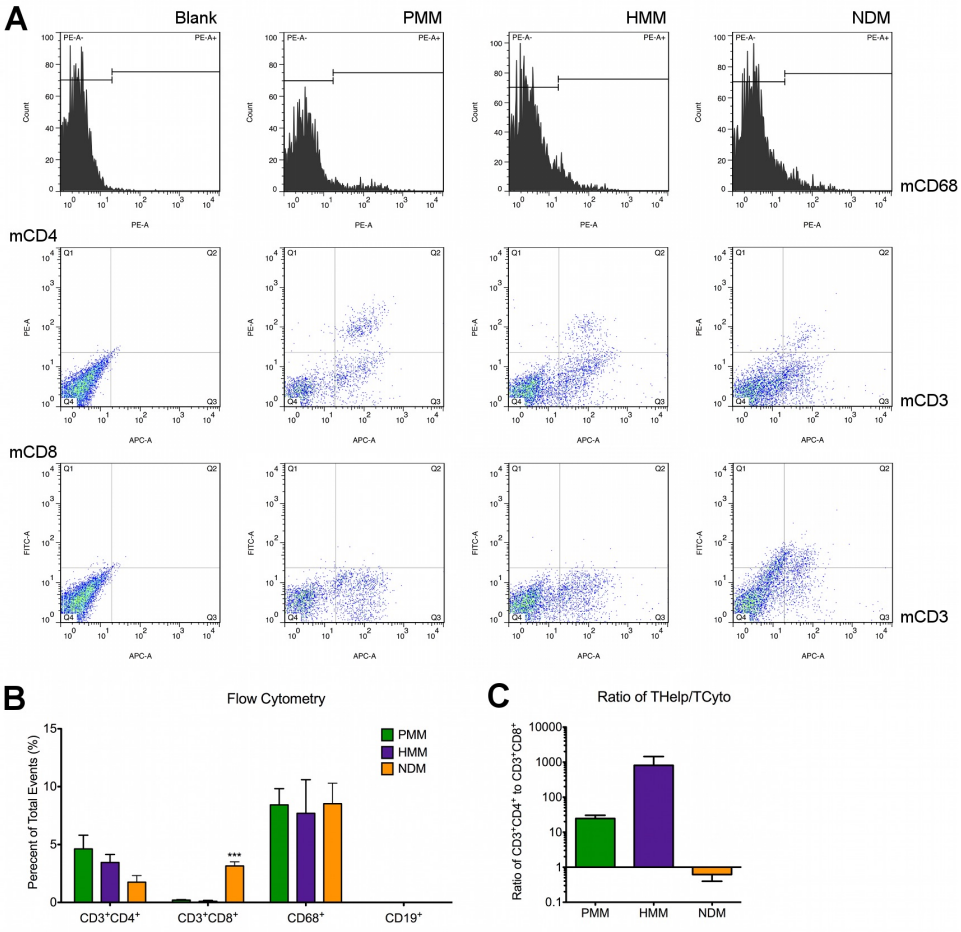

Figure 3.6: Flow cytometry cellular quantification in Balb/c animals for either PMM, HMM, or NDM. (A) Representative histograms or scatter plots for staining of macrophages (mCD68+), T-Helper cells (mCD3+mCD4+), and Cytotoxic T-cells (mCD3+mCD8+). B-cells (CD19+) were not detected in the biomaterials. (B) Averages and standard deviations for each treatment group and cell type analyzed with flow cytometry (***p<0.001). (C) Ratio of T-Helper cells to Cytotoxic T-cells showing PMM and HMM favoring T-Helper cells and NDM favoring Cytotoxic T-cells.

3.3 Discussion

In this study, we investigated the ability of a humanized mouse model, which had previously shown the ability to reject xenogeneic tissue via a human T-cell mediated immune response [128], to differentiate between allogeneic and xenogeneic decellularized ECM. We tested a xenogeneic biomaterial sourced from porcine myocardial matrix (PMM), which was developed as a potential therapy for treating MI [47], and a similarly produced material derived from human cadaveric donor hearts (HMM) as an allogeneic alternative [130]. The Hu-mice model showed significant differences in the immune response to the allogeneic and xenogeneic materials, unlike the wild type model, suggesting that the Hu-mouse model could be an advantageous tool in studying the biocompatibility of human based, allogeneic materials.

Investigation of the infiltrating cellular profiles into each material showed significant differences in the density of human cells in the Hu-mice between the PMM and HMM groups with more migration into the core of PMM compared to HMM. Cells within the PMM biomaterial included macrophages, T-helper cells ($CD3^+$, $CD4^+$) and very few cytotoxic T-cells ($CD3^+$, $CD8^+$). Substantially lower to almost zero quantities of these cells were observed in the allogeneic condition (HMM) for the Hu-mice. However, when the same HMM material was implanted into wild type Balb/c mice, and is thus xenogeneic, cellular infiltration contained both types of T-cells and macrophages similar to the PMM in the Balb/c mice. The infiltrating T-helper cells observed in all three xenogeneic conditions were then further

characterized with qRT-PCR since they can be polarized into two the subtypes of Th1 and Th2. The two lineages were identified by the expression of cell-specific master transcription factors TBX21 (T-bet) or GATA3 for Th1 and Th2, respectively. This expression is directly correlated with separate phenotypes involving the production of IL-2 and interferon-γ (IFNγ) for Th1 and IL-4, IL-5, and IL-10 for Th2 [147]. Both biomaterials created a shift towards the Th2 phenotype when compared to the NDM control, indicating a pro-remodeling immune response. In addition to T cells, macrophages can be polarized to either a pro-inflammatory or a pro-remodeling phenotype [133, 148]. Rather than discrete phenotypes, macrophage polarization is plastic and should be considered on a sliding scale with a variety of degrees of polarization depending on the local niche [148, 149]. This includes the more classically defined M1 and M2 phenotypes, which correspond to the Th1 and Th2 profiles, respectively [150]. M1 macrophages are known to produce inflammatory cytokines of TNF, IL-6, and IL-1β with high levels of IL-12 and IL-23, and low levels of IL-10. Whereas, the M2 polarized macrophages have low levels of IL-12 and IL-23 with high levels of IL-10 [143]. Macrophage phenotypic expression has been shown to be an important indicator of tissue remodeling outcomes for ECM based biomaterials [151, 152]. For ECM scaffolds, the M2 or Th2 cell profile has been correlated with positive or pro-remodeling inflammatory response leading to constructive outcomes. Polarized macrophages of the M1 and M2 phenotypes are classified by numerous different markers and commonly include iNOS and ARG-1 expression,

respectively [153]. A ratio of ARG-1/iNOS gene expression was previously used to measure macrophage polarization towards the M2 phenotype [144]. Here we showed that both biomaterials under xenogeneic conditions (HMM in Balb/c, and PMM in Balb/c and Hu-mice) favored the M2 or pro-remodeling polarization when compared to the control group. Thus, the polarization of PMM in the Hu-mice model was recapitulated appropriately in the Balb/c model as a xenogeneic material under both conditions. These results therefore suggest that testing a xenogeneic biomaterial in preclinical studies in a wild type or immune competent animal could be sufficient for modeling the human immune response. However, a wild type rodent model is likely to be insufficient to test a human derived, allogeneic material, and the Hu-mouse model could be used to more thoroughly model the human immune response to these materials.

These results also demonstrate the insufficiency of immunocompromised NSG mice in modeling the response to biomaterials. There was significantly less cellular infiltration in NSG animals compared to immunocompetent Balb/c animals. Macrophages are present in both animal models, but T-cells are not present in the NSG mice. Therefore, macrophages alone are potentially not sufficient to produce a full immune response to these materials. This is not surprising since the more severe xenogeneic tissue rejection has been shown to be largely a T-cell mediated response and involves the subsequent activation of macrophages [127, 128]. Thus, this brings about concern in utilizing immune compromised animals in studies when a

naturally derived material is used, either as the therapy itself or as a platform for delivering cells or other biologics.

The efficacy of tissue decellularization, tissue source age, and potential addition of chemical cross-linkers are crucial parameters that can significantly impact the host inflammatory response [131]. Thus, every decellularized biomaterial should be appropriately tested for their elicited immune response in an immune component animal model since all decellularized materials will not cause the same degree of immune response stimulation. For example, compared to previously published histological images of decellularized small intestinal submucosa (SIS) implanted subcutaneously [154], the immune response elicited by our injectable biomaterials tested here are relatively mild with substantially fewer cells infiltrating from the surrounding tissue. Furthermore, variations in immune response for biomaterials can be observed due to differences in the delivery method, the implantation site, and the form of the biomaterial. In our studies, the biomaterials were implanted via injection into the subcutaneous space. In terms of physical and mechanical properties these injectable materials are relatively soft hydrogels unlike the solid surgically implanted SIS decellularized grafts. Under these conditions we showed successful differentiation of the xenogeneic and allogeneic biomaterials in the humanized model. One limitation of the humanized mouse model is that it is not able to measure the role of certain xenogeneic specific epitopes, including the anti-Gal epitope, which is involved in xenogeneic tissue rejection in humans [128]. However, processed xenogeneic acellular materials,

which have dramatically lower levels of the alpha-Gal epitopes, such as the materials used in this study, have not shown or been proven to cause adverse reactions in human patients [131]. Despite this model limitation, the Hu-mouse model was able to distinguish between the xenogeneic versus allogeneic ECM in this study.

3.4 Conclusion

In conclusion, we have utilized a xenogeneic material, PMM, and an allogeneic material, HMM, in a humanized mouse model, demonstrating its potential as a new tool for preclinical biomaterial testing. This work confirms that these naturally derived biomaterials elicit a T-cell mediated immune response, with a pro-remodeling Th2 and M2 polarization, and utilizing an immune compromised animal does not properly mimic the tissue response to ECM derived materials. Both PMM and HMM in an immune competent animal favored a T-helper cell population with almost zero cytotoxic T-cells present. However, differences between the materials were then observed in the Hu-mouse model, namely a similar response to the xenogeneic PMM as in the wild type mouse, but a significantly reduced and minimal response to the allogeneic HMM. Thus, while wild type mice may be sufficient to model a xenogeneic response, the Hu-mice model could be a useful tool to better mimic the potential human immune response to allogeneic biomaterials prior to clinical translation.

3.5 Materials and Methods

All experiments in this study were performed in accordance with the guidelines established by the committee on Animal Research at the University of California, San Diego, and the American Association for Accreditation of Laboratory Animal Care.

3.5.1 Fabrication of PMM, HMM, and NDM

Both the porcine myocardial matrix (PMM) and human myocardial matrix (HMM) were previously developed and characterized [47, 130]. Human hearts were obtained from donor patients who hearts could not be used for transplantation under an institutionally approved protocol. In brief, left ventricular tissue (porcine or human) was isolated and chopped into small pieces. The tissue was spun in phosphate buffered saline (PBS) containing 1% (wt/vol) sodium dodecyl sulfate (SDS) (Fischer Scientific, Fair Lawn, NJ) with 0.5% penicillin streptomycin (PS) (Gibco, Life Technologies, Grand Island, NY) of 10,000 U/mL until fully decellularized. The human tissue was treated with additional lipid and DNA/RNA removal steps that were needed to fully decellularize the tissue [130]. Once decellularized, the remaining ECM was lyophilized, milled, and partially digested with pepsin into a liquid form as previously described [47, 130]. Non-decellularized myocardial matrix (NDM) was made from porcine ventricular tissue as a control. The tissue was simply rinsed in the PBS and PS solution with no SDS for one day. Then the non-decellularized porcine tissue was processed into an injectable form using the

same methods as with the decellularized myocardial matrix. Finally, the materials were lyophilized and stored at -80°C until re-suspending with sterile water before injection.

3.5.2 Hydrogel Characterization

Porcine and human myocardial matrix hydrogels were imaged for nano-scale topography and fiber formation with scanning electron microscopy (SEM) as previously described [114, 130]. In brief samples were gelled for 24 hours at 37 °C and then fixed in a solution of 4% paraformaldehyde and 4% glutaraldehyde for 24 hours. Next, the gels were dehydrated with a series of gradated ethanol rinses. Then, fixed and dehydrated hydrogels were processed in an automated critical point drier (Leica EM CPD300, Leica, Vienna). Mounted samples were then sputter coated (Leica SCD500, Leica, Vienna) with platinum while being rotated. The samples were then imaged on a FE-SEM (Sigma VP, Zeiss Ltd, Cambridge, UK) at 0.6 kV using the in-lens SE1 detector.

Immunohistochemistry was performed on the porcine derived material to assess removal of the alpha-gal epitope. Freshly isolated porcine left ventricular tissue, decellularized porcine myocardium, and porcine myocardial matrix hydrogels were fresh frozen in OTC for cyrosectioning. Sections (20 μm) were mounted onto glass slides and fixed in 4% paraformaldehyde for 10 minutes and permeabilized in acetone for 1.5 min. Slide samples were either stained with Hematoxylin and Eosin (H&E) or prepared for

immunohistochemistry. Samples were blocked with a buffered solution containing bovine serum albumin (BSA) and stained for at least 12 hours at 4°C with M86 anti-alpha-gal (1:10, Enzo Life Sciences, Framingdale, NY) followed by incubation for 30 minutes with secondary anti-mouse Alexa Fluor 488 antibody (1:100, Life technologies, Carlsbad, CA) [155]. Hoechst 33342 was used to stain nuclei. Slides were imaged with a Carl Zeiss Observer D1 and Zeiss AxioVision SE64 software (Carl Zeiss, Jena, Germany).

3.5.3 Humanized Mouse Model

NOD.Cg-Prkdc^{scid}Il2rg^{tm1wjl}/SzJ (NSG) (The Jackson Laboratory) mice of 6-10 weeks of age after conditioning with sublethal (2.25 Gy) total body irradiation underwent the following procedure, as previously described, to create the humanized mouse model (Hu-mice) [126]. First, the mice were transplanted under the kidney capsule with a piece of human fetal thymic tissue of about 1 mm^3 that had been previously frozen. Next, the animals were transfused intravenously with 1-5 x 10^5 human CD34$^+$ fetal liver cells from the same patient donor. Human fetal tissue, from Advanced Bioscience Resource, of gestational ages of 17-20 days was utilized.

3.5.4 Biomaterial Injection and Harvesting

Animals were briefly put under anesthesia using either 2.5% Isoflurane or via injection with ketamine and xylazine. Each mouse was injected with only one biomaterial and received four 250 µL evenly spaced subcutaneous

injections in the dorsal region. Each injection was premixed with 0.5 µL of sterile india ink to visually label the matrices for ease of identification upon harvesting. The injections with neighboring dermal tissue and spleens were harvested 1-week later for analysis with histology and immunohistochemistry (n=8-12), flow cytometry (n=4), or qRT-PCR (n=4-12). Along with the Hu-mouse, both male NSG and male Balb/c (Jackson Laboratories or Harlan Laboratories) of the same ages were used for immune compromised and wild type immune system controls, respectively.

3.5.5 Quantitative Real-Time Polymerase Chain Reaction (qRT-PCR)

After harvesting, tissue was immediately flash frozen in liquid nitrogen and stored at -80°C until processed. Tissue was homogenized and then run through an RNEasy kit (Qiagen) along with an on-column DNase digestion step (Qiagen) to extract RNA with minimal genomic DNA contamination. Superscript III Reverse Transcriptase kit (Applied Biosystems) was used to synthesize cDNA. Then, SYBR Green PCR Master Mix (Applied Biosystems) was used with forward and reverse primers at a final concentration of 1 µM. Primers for macrophages were designed to be mouse specific while primers for T-helper cells were co-reactive for their specific gene of interest in both the mouse and human genome to allow for comparisons between the Balb/c and Hu-mice study groups. Primers used included: Arg-1 (F: 5'-GAACACGGCAGTGGCTTTAAC-3', R: 5'-TGCTTAGTTCTGTCTGCTTTGC-3'), iNOS (F: 5'-CAGCTGGGCTGTACAAACCTT-3', R: 5'-

CATTGGAAGTGAAGCGTTTCG-3'), GATA3 (F: 5'-CTCGGCCATTCGTACATGGAA-3', R: 5'- GGATACCTCTGCACCGTAGC-3'), TBX21 (F: 5'-AGCAAGGACGGCGAATCTT-3', R: 5'-GGGTGGACATATAAGCGGTTC-3') and GAPDH (F: 5'-CATCAAGAAGGTGGTGAAGC-3', R: 5'-GTTGTCATACCAGGAAATGAGC-3'). Samples were run in technical duplicates along with negative controls without template cDNA to confirm lack of contamination in PCR reagents. PCR reactions were run on a CFX95™ Real-Time System (Biorad) with the following thermal cycler settings: 2 min at 50°C, 10 min at 95°C, followed by 40 cycles of 15s at 95°C and 1 min at 62°C. After completing 40 cycles of PCR amplification, automated melting curve analysis, consisting of increasing the thermo cycler temperature from 50°C to 95°C at 5°C increments lasting 5s each, was used to confirm formation of a singular PCR amplicon for each primer set. Bio-Rad CFX Manager™ 3.0 (Biorad) was used for determining cycle threshold (ct) values from recorded SYBR green signal.

Gene expression ratios for assessing immune cell response polarization were calculated by modification of methods by Livak et al. for relative gene expression analysis [156]. The Δct was calculated between representative genes for either macrophage and T-helper cell polarized phenotypes. Fold change was then determined by $2^{-(\text{Gene 1} - \text{Gene 2})}$ and normalized to fold change of corresponding NDM ratios for comparison. Ratios of Arg-1/iNOS and GATA3/TBX21 were selected to quantify

macrophage and T-helper cell polarization. GAPDH values were used to confirm consistent loading between PCR reactions.

3.5.6 Histology and Immunohistochemistry

Each injection was harvested and divided in half for either paraffin embedding or fresh frozen in OCT for cryosectioning. Samples were sectioned to obtain a transverse section of the biomaterial and neighboring dermal tissue. Paraffin embedded samples were de-paraffinized and then stained with Hematoxylin and Eosin (H&E) from slides taken from five evenly spaced locations. Cryosections from three different evenly spaced locations were used for all immunohistochemistry. Slides were fixed with acetone or 4% paraformaldehyde and blocked with a buffered solution containing bovine serum albumin. The following primary antibodies were incubated for 1 hour at room temperature or for 12-18 hours at 4°C: anti-Macrophage (1:200 dilution, Abcam), anti-mCD3 (1:100 dilution, Abcam), anti-mCD4 (1:200 dilution, Bioss), anti-mCD8 (1:200 dilution, Bioss), anti-human nuclei (1:250 dilution, Millipore), anti-hCD3 (1:50 dilution, Abcam), anti-hCD4 (1:50 dilution, Becton Dickinson), anti-hCD8 (1:500 dilution, Becton Dickinson). The following secondary antibodies were incubated for 30-45 minutes: anti-rat Alexa Fluor 568 (1:250 dilution), anti-rabbit Alexa Fluor 488 (1:500 dilution), anti-mouse Alexa Fluor 488 (1:500 dilution), anti-rat Alexa Fluor 488 (1:400 dilution), anti-rabbit Alexa Fluor 568 (1:200 dilution). Bright field images were taken with Leica Aperio ScanScope® CS^2, and fluorescent images with the Leica Ariol®

system. Cellular density and human nuclei quantification were done via an automated counting program as part of the Leica Ariol® system. An individual blinded to the study groups identified the biomaterial outline and the core of the biomaterial was defined as 200 μm interior to the exterior perimeter of the biomaterial.

3.5.7 Flow Cytometry

Cells were isolated from injected tissue and spleens by first chopping the tissue into small pieces and digesting with 4 Wunsch Units of Liberase Blendzyme TM (Roche), 4 Wunsch Units of Liberase Blendzyme TH (Roche), 100 Kunitz Units of DNase 1 (Stem Cell), and 200 μL of 1 M HEPES (Gibco) in 10 mL of 199 Media (Gibco) at 37°C. The reaction was quenched and then filtered through a 40 μm cell filter. Cells were rinsed and suspended in a concentration of 1 x 10^6 cells/mL or less in FACS buffer. Cells were then divided and stained for 45 minutes on ice with following conjugated primary antibodies or their corresponding isotope control antibody to remove non-specific binding: APC-anti-mCD3 (1:40 dilution, Biolegend), PE-anti-mCD4 (1:80 dilution, Biolegend), FITC-anti-mCD8 (1:50 dilution, Biolegend), APC-anti-mCD19 (1:20 dilution, Biolegend), PE-anti-mCD68 (1:80 dilution, Biolegend). Cells were either analyzed immediately or fixed and then analyzed on a FACSCanto Flow Cytometer machine using FACS Diva software (Becton Dickinson).

3.5.8 Statistics

All data and plots are presented as mean ± SEM unless otherwise stated. Significance was determined with a one-way ANOVA using a Tukey post-hoc test for histology and flow cytometry, an unpaired student's *t*-test for human nuclei data, and a one-way ANOVA using a Dunnett's post-hoc test for qRT-PCR data with a $p<0.05$.

3.6 Acknowledgements

The authors would like to thank Matt Joens for his technical expertise in scanning electron microscopy. The authors would also like to thank Lifesharing for their assistance in obtaining the human cardiac tissue. Funding for this work was provided by CIRM (TR3-05559 and TR1-01277 to YX) and the NIH NHLBI (HL113468 to KLC). TDJ received funding during the project as a Powell Fellow from the Powell Foundation, the NHLBI as a training grant recipient, and the NSF as a graduate student fellow. KLC is co-founder, board member, and holds equity interest in Ventrix, Inc.

Chapter 3, in full, is currently being prepared for submission for publication of the material. Rong, Zhili; Wang, Raymond M.; He, Jingjin; Wong, Michelle; Nigam, Vishal; Behfar, Atta; Xu, Yang; and Christman, Karen L. The dissertation author was the primary investigator and author of this material.

CHAPTER 4 – Tissue Specific Extracellular Matrix Hydrogel Promotes Tissue Remodeling and Increased Arteriogenesis and Perfusion in a Peripheral Artery Disease Model

4.1 Introduction

As previously discussed, our lab has developed a porcine skeletal muscle matrix (SKM) and shown the potential of this biomaterial as a stand-alone therapy [58]; however, the effect on functional perfusion, which is a mainstay of translational studies for PAD, was not assessed. Moreover, the importance of treating the tissue with a tissue specific biomaterial was not demonstrated. In this study we investigated the tissue specific SKM hydrogel compared to a new non-tissue specific hydrogel derived from decellularized human umbilical cord matrix (hUC) in a rodent hindlimb ischemia model to test their ability to improve hindlimb tissue perfusion and muscle fiber remodeling. Decellularized materials from younger sources have been shown to stimulate increased regeneration upon implantation [111], and therefore, the hUC hydrogel was developed and tested in this study. Also, hUC represents a readily available neonatal allogeneic tissue source for an extracellular matrix (ECM) hydrogel that could avoid both immunologic and ethical concerns surrounding porcine derived products. Here we show that both decellularized ECM based hydrogels are capable of improving perfusion over a saline control; however, the SKM hydrogel potentially had a greater effect on tissue remodeling.

4.2 Results

4.2.1 Decellularized tissues can be processed into injectable hydrogels

For comparison to our previously fabricated porcine SKM hydrogel, we developed a new non-tissue specific injectable biomaterial from hUC. The general process for both materials is shown in Figure 4.1A. Starting material for each hydrogel (either porcine psoas muscle or human umbilical cords) was decellularized with detergent. The resulting ECM was then lyophilized and milled into a fine powder, followed by partial enzymatic digestion to create a liquid form, which can be injected and form a hydrogel *in situ* at physiological conditions. Decellularization of the SKM and hUC was confirmed with Hematoxylin and Eosin (H&E) staining (Figure 4.1B), which demonstrated lack of nuclei, as well as by measuring dsDNA content, which showed 1.09 ± 0.053 ng of DNA per mg of dry ECM for SKM and 0.92 ± 0.047 ng of DNA per mg of dry ECM for hUC with no significant difference between the two (Figure 4.1C). This was well below the previously published recommended maximum threshold for decellularized matrices of 50 ng of DNA per mg of dry ECM [106]. Nucleic acid concentrations were also measured and found to be undetectable by absorption measurement using a NanoDrop Spectrophotometer. Sulfated glycosaminoglycan (sGAG) content, an important ECM parameter, which can sequester native growth factors and mediate cellular functions [107, 108], was also quantified in the liquid ECMs. The SKM contained significantly (P<0.05) more sGAGs with 6.1 ± 0.15 μg of sGAG per mg of dry ECM compared to hUC with 5.5 ± 0.15 μg of sGAG per mg of dry ECM, although the difference was

relatively minimal. The molecular weights of the protein and peptides in each material were compared using PAGE (Figure 4.1D). Both materials displayed bands matching the control collagen (Col) lane; however, there were distinct differences between the two ECM materials in the band pattern, both at high and low molecular weights. Upon gelation and self-assembly at physiological conditions, both materials created a complex mesh of nano-scale fibers as shown with scanning electron microscopy (SEM) (Figure 4.1E). The macro structures were different in morphology with the SKM hydrogel forming a consistent fine mesh and the hUC hydrogel forming a more irregular structure with larger associations of fibers.

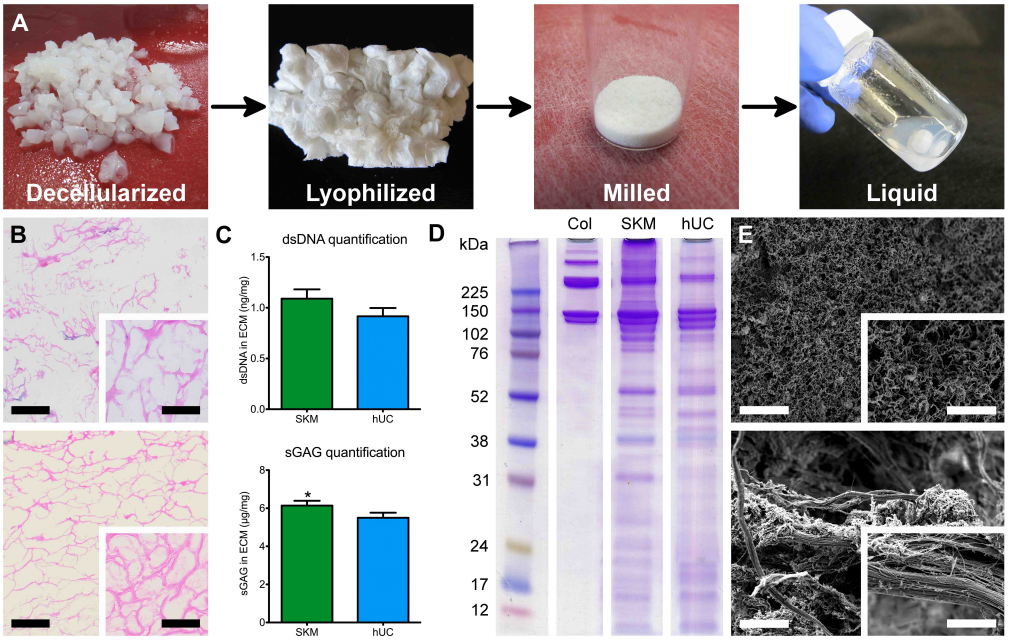

Figure 4.1: Development and characterization of hUC and SKM. (**A**) Flow chart showing the decellularized tissue (hUC), which is then lyophilized, milled into a fine powder, and digested into a liquid form for injection. (**B)** Histological confirmation of decellularization of SKM (top) and hUC (bottom) with H&E staining. Scale bars for main images and inset images are 400 µm and 50 µm, respectively. (**C**) Quantification (n=3) of the dsDNA content (top) and the sGAG composition (bottom) in each biomaterial. (**D**) PAGE shows the molecular weight bands of each biomaterial compared to a single ECM component, collagen (Col). (**E**) Scanning electron microscopy (SEM) demonstrates the differences in nano-scale topography of the SKM (top) and hUC (bottom) hydrogels. Scale bars for main SEM images and inset images are 20 µm and 4 µm, respectively. *$P < 0.05$ (Students *t* test).

4.2.2 SKM and hUC affect cell proliferation and migration *in vitro*

An important ability for a therapy for PAD is to stimulate new vessel growth into the ischemic region and encourage healing of the ischemic damaged muscle. Young ECM, such as in the umbilical cord, contains higher quantities of GAGs [157, 158], which have been show to promote proliferation and migration of a variety of cell types [159]. We therefore assessed the ability of hUC, which is fetal tissue derived ECM, to stimulate proliferation and migration of smooth muscle cells, endothelial cells, and skeletal myoblasts compared to

the SKM. After 3 days of culture on SKM or hUC coated tissue culture plastic there was a significant increase in proliferation on coatings of hUC over SKM for both smooth muscle cells ($p<0.05$) and skeletal myoblasts ($p<0.001$), but not for endothelial cells (Figure 4.2A). Also, proliferation on hUC coatings was significantly increased ($p<0.001$) over culture on SKM for skeletal myoblasts after 5 days in culture, but this trend was not maintained for the smooth muscle cells (Figure 4.2B). In terms of migration, there was a significant increase ($p<0.001$) observed for smooth muscle cells on SKM coatings with both endothelial cells and skeletal myoblasts having no differences after 24 hours. This trend at 24 hours was continued after 48 hours of culture (Figure 4.2D) for smooth muscle cells ($p<0.001$). In addition, migration was significantly increased for skeletal myoblasts after 48 hours in culture on hUC coatings ($p<0.001$).

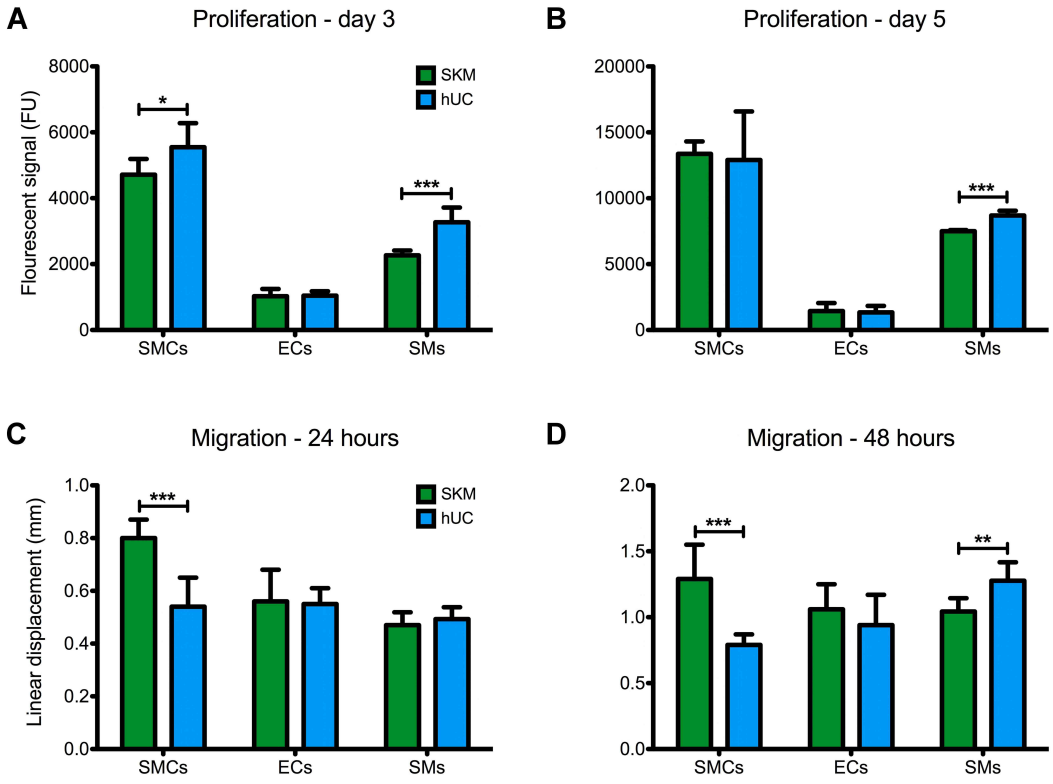

Figure 4.2: Migration and proliferation of smooth muscle cells (SMCs), endothelial cells (ECs) and skeletal muscle myoblasts (SMs). All *in vitro* work was performed on 2D coatings of SKM or hUC. (**A**) Proliferation (n=8) after 3 days and (**B**) 5 days of culture as quantified by a PicoGreen assay. (**C**) Migration (n=6) using a tilt assay after 24 hours and (**D**) 48 hours of culture. **P*<0.05, ***P*<0.01, and ****P*<0.001 (Students *t* test).

4.2.3 Injectable ECM hydrogels increase hindlimb tissue perfusion

To mimic PAD, a hindlimb ischemia model was utilized in this 42 day study (Figure 4.3A). Here we used an ischemia model with the excision of a substantial segment of the femoral artery and vein from one of the animal's hindlimbs (Figure 4.3B). This allowed for the healthy or non-operated limb to serve as an internal control. Tissue perfusion was assessed utilizing a newer *ex vivo* imaging technology, laser speckle contrast analysis (LASCA) (Figure 4.3C). To better simulate treating the chronic state of the disease, the therapy

was injected (Figure 4.3D) one-week after the acute injury to allow for the immediate inflammatory response to resolve. Perfusion readings were taken on each animal regularly throughout the study to day 42 post-surgery. LASCA allowed for continuous monitoring and instantaneous full field analysis of a single animal with readings lasting at least 20 minutes to reach perfusion equilibrium (Figure 4.3E). As shown in the example reading in Figure 4.3D, percent perfusion of the ischemic limb to healthy limb was calculated once the animal had been under anesthesia for 5 minutes, 10 minutes, and then after reaching perfusion equilibrium. Equilibrium was defined as the point when the perfusion in either limb did not change for at least a five-minute period. This sampling of the continuous perfusion readings at discrete time intervals allowed for comparison to other currently published Doppler data, which is measured once the animal is under anesthesia for fixed time [160, 161]. The day 0 pre- and immediately post-surgery perfusion measurements for each treatment group were compared and shown to not be statistically different (Figure 4.3F).

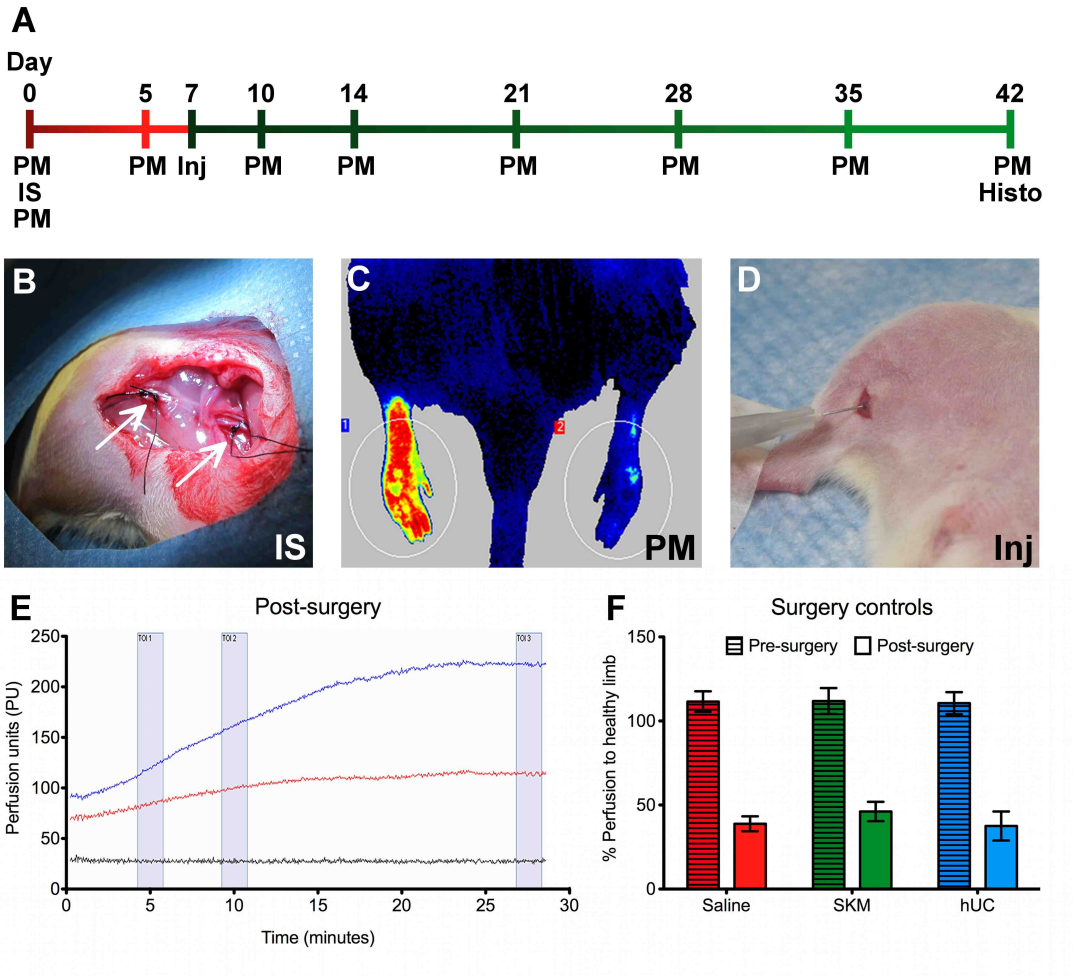

Figure 4.3: The *in vivo* functional perfusion study design in a rat hindlimb ischemia model. (**A**) *In vivo* study timeline. (**B**) The hindlimb ischemia surgery in a rat hindlimb. The arrows indicate the two locations for ligation and excision of both the femoral artery and vein. (**C**) Hindlimb perfusion measurements were taken using laser speckle contrast analysis (LASCA). Image shown is of an animal post-surgery with a significant decrease in perfusion of the ischemic (right) limb compared to the healthy (left) limb. (**D**) The biomaterial therapy was injected into the gracilis muscle on day 7 post-surgery. (**E**) An example perfusion measurement for a single ischemic animal is shown. The healthy limb (blue line), the ischemic limb (red line), and total body (black line) are plotted over time in arbitrary units or Perfusion Units. (**F**) Plotted are the pre-surgery and immediately post-surgery readings for each treatment group showing no significant difference between the groups. PM = perfusion measurement, IS = Ischemia surgery, Inj = Injection, and Histo = Histology.

Both of the injected hydrogels alone, SKM or hUC, lead to a significant increase in percent perfusion as early as day 28 and this improvement was maintained until the end of the study on day 42 (Figure 4.4A). Perfusion in the

saline treated group plateaued after day 14 while treated groups continued to show improvements beyond day 21. Significant separation in the biomaterial treated groups from the control group was observed in perfusion measurements plotted for each individual animal at day 42 (Figure 4.4B). For example, the day 42 measurements after under anesthesia for 10 minutes (a typical time for laser Doppler measurements) [160, 162] showed the ischemic damaged limb to be perfused at 65.7 ± 13.3% for saline, 96.4 ± 13.8% for SKM (P<0.001, compared to saline), and 84.2 ± 14.3% for hUC (P<0.05, compared to saline). Overall, the SKM group trended higher than the hUC alone therapy at 5 and 10 minute readings, although this was not significant. Representative perfusion images show that the SKM and hUC hydrogel treated limbs more closely matched their respective healthy limbs than the saline treated limb (Figure 4.4C). Due to the ability of LASCA to monitor a given animal continuously while under anesthesia, we were able to watch the animals' cardiovascular adjustment through the transition of anesthesia levels. The animals were initially anesthetized with 5% Isoflurane for a fixed period of time and then immediately transferred to 2.5% when the perfusion reading started. Decreasing the level of Isoflurane creates an increase in cardiac output and perfusion of blood in the peripheral skeletal muscle [163]. Thus, from the start of the reading, the perfusion increased in the hindlimbs as the animal rested on the deck (Figure 4.3E). From this, perfusion kinetics can then be reported to show the rate of change of perfusion over time. This was calculated as a ratio of the slopes from the linear region of the ischemic foot to

the healthy foot. The healthy animals pre-surgery were assessed to confirm symmetric perfusion rates in each limb, leading to perfusion kinetics values near one (Figure 4.4D). Immediately post-surgery, the ischemic damaged tissue did not re-perfuse sufficiently due to femoral artery and vein excision, which is indicated by the perfusion kinetics being closer to zero for all groups (Figure 4.4D). By day 5 post-ischemia, but still pre-injection, the animals had partially recovered due to endogenous healing mechanisms and produced consistently improved perfusion kinetics of approximately 0.4 (Figure 4.4E). Finally, by the end of the study, perfusion kinetics for the SKM and hUC hydrogels showed significant improvements over the saline (P<0.001 for SKM; P<0.05 for hUC) control, which was maintained at approximately 0.4 (Figure 4.4F). This result indicates that for the treated animals, the vessel network perfusion kinetics of their ischemic damaged limb had improved to match initial healthy kinetics. From this new perfusion kinetics parameter, calculated from the LASCA perfusion measurements, we were able to provide further potential insight into vessel network function.

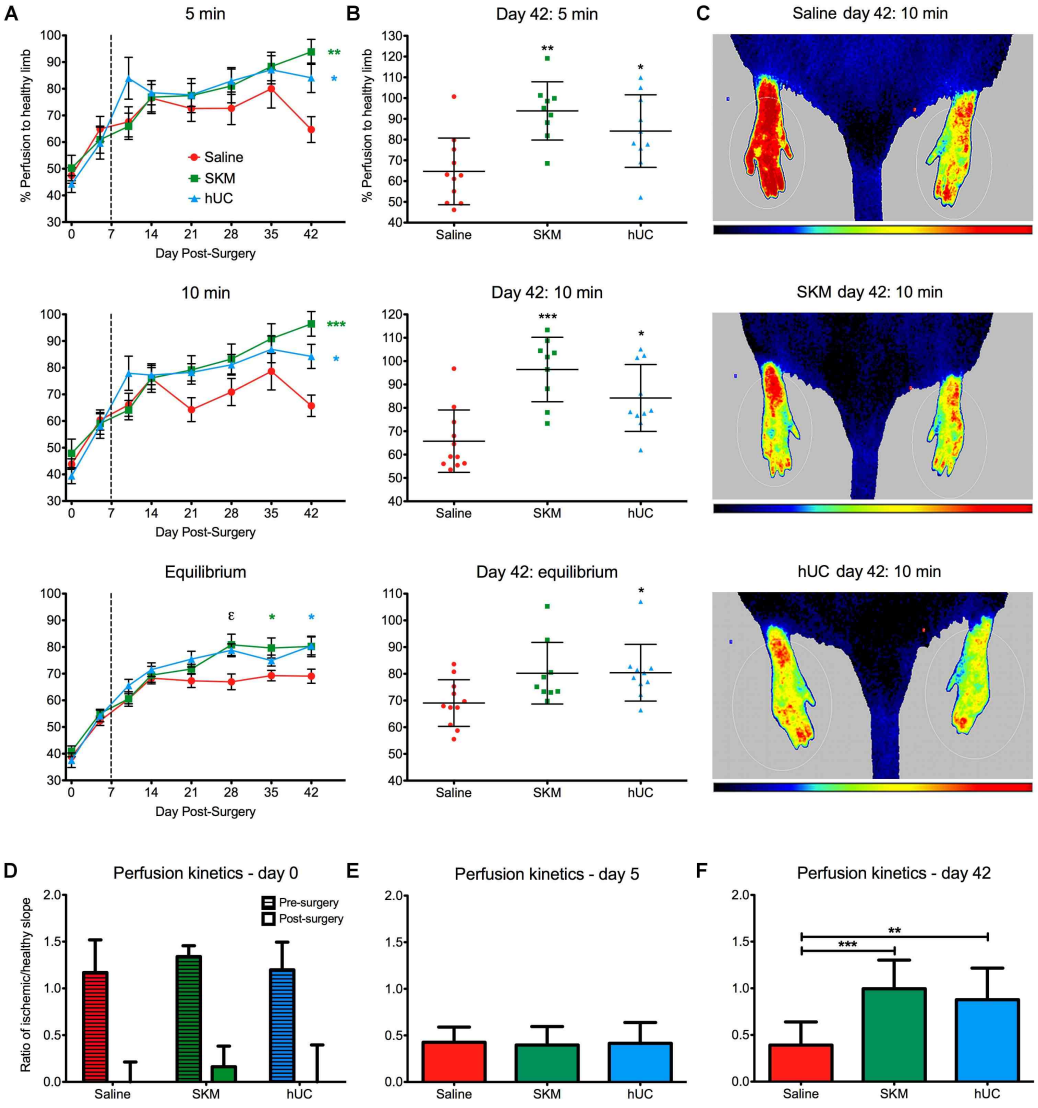

Figure 4.4: Hindlimb tissue perfusion and perfusion kinetics. (**A**) Hindlimb perfusion measurements over the 42 day period showed an increase in perfusion due to treatment with either the SKM (n=9) or hUC (n=10) hydrogels alone over saline (n=11). Readings are shown after the animal had been under anesthesia for 5 min, 10 min, and after reaching perfusion equilibrium. Vertical dotted line indicates time of treatment injection on day 7. (**B**) Scatter plots showing individual animal perfusion readings on day 42 are plotted to show the significant population shifts. (**C**) Example representative perfusion images for each treatment group after the animal was under anesthesia for 10 min. Note: Since the units for perfusion are arbitrary, color comparisons between limbs can only be done on the same animal and not between two different animals. (**D**) Perfusion kinetics for pre-surgery and post-surgery are shown with no significant differences between the treatment groups. (**E**) Pre-injection perfusion kinetics on day 5 are slightly improved from post-surgery day 0. (**F**) By day 42 both SKM or hUC treatment lead to significant improvements in hindlimb tissue perfusion kinetics. **P*<0.05, ***P*<0.01, ****P*<0.001, and **ε***P*<0.05 for both treatment groups (One-way ANOVA with a Tukey post-hoc test). All plotted error bars are standard deviation (SD) except for in **A**.

4.2.4 ECM hydrogels stimulated increased density of larger vessels

After significant increases in hindlimb tissue perfusion with the biomaterials alone were shown with LASCA, both the arterial vessel population and capillary density were investigated via histology on day 42. Although average capillary (Figure 4.5A) and arteriole density (Figure 4.5B) did not vary between treatment groups, there was a significant increase in the average arteriole diameter for SKM animals compared to saline (Figure 4.5C). More specifically there was a dramatic increase in density of larger arterioles, including those with a diameter of greater than 75 μm for the SKM group (Figure 4.5D). The percent lumen area compared to total tissue area analyzed also significantly improved for SKM over saline (Figure 4.5E). Similar trends were observed for these measurements with the hUC hydrogel, but were not statistically significant compared to saline. A representative image of capillary staining for the SKM group is shown in Figure 4.5F, while example arteriole staining from all treatment groups and healthy limbs is shown in Figure 4.5G-J. These findings of increased density of larger arterioles confirm and correlate to the increased hindlimb perfusion and perfusion kinetics as measured from LASCA. The biomaterials were able to increase the density of larger arterioles and concurrently the distal hindlimb tissue perfusion.

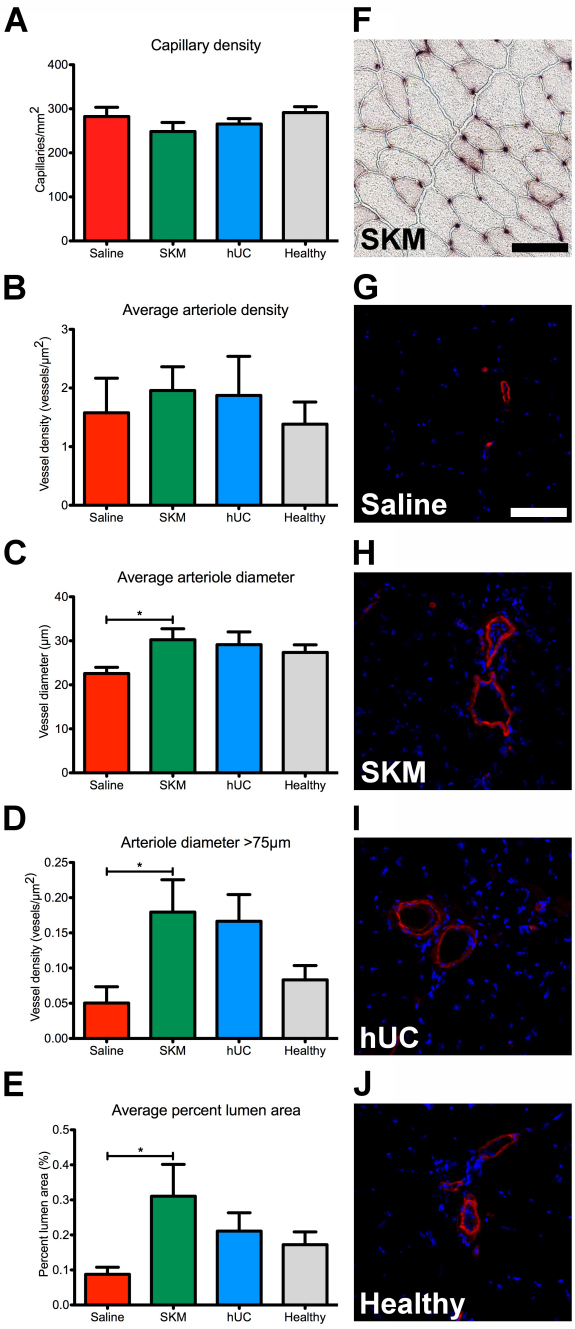

Figure 4.5: Histological assessment of arteries and capillaries. (**A**) Capillary density quantification showed no differences between the groups. (**B**) There were no differences in arteriole density between all groups, but the average arteriole diameter (**C**) and density of arterioles with diameter greater than 75 μm (**D**) was significantly increased in the SKM group. **(E)** Average percent lumen area was also significantly improved for the SKM group. (**F**) Example representative image of capillaries stained by alkaline phosphatase for the SKM treatment group. **(G**) Example arteriole staining with anti-αSMA (red) and nuclei (blue) for Saline, (**H**) SKM, (**I**) hUC, and (**J)** healthy tissue. *P<0.05 (One-way ANOVA with a Dunnett's post-hoc test) and scale bars are 100 μm.

4.2.5 Hydrogels were fully degraded and promoted healthy tissue integrity

On day 42 post-surgery or 5 weeks post-injection, hindlimb muscle tissue cross-sections were stained with Hematoxylin and Eosin (H&E) and analyzed by a histopathologist blinded to the treatment groups (Figure 4.6A). Histological analysis concluded that the biomaterial had fully degraded, no scarring or interstitial inflammatory response was observed, and the resulting skeletal muscle fibers were predominantly healthy. No observable differences were seen between the treatment groups and healthy hindlimb skeletal muscle. Mason's Trichrome stained slides were surveyed (Figure 4.6B) as a further assessment of fibrous collagen scar formation and no scarring was seen in either treatment group. Chronic inflammation is a concern after implanting a new biomaterial, so presence of macrophages was examined. Macrophages in the tissue were very low in density in all groups and were seen as only single cells evenly spaced throughout the tissue. Macrophage density in the treated animals was observed to be similar to that of the healthy tissue. A representative image from the SKM group is shown in Figure 4.6C. Next, laminin staining (Figure 4.6D) was utilized to measure area fraction of ECM to assess interstitial ECM deposition [164]. No significant differences were observed with about 20% of the surveyed area being covered by positively stained laminin (Figure 4.6E).

Fibers with centrally located nuclei can be an indicator of abnormal or damaged muscle [165]. No significant differences in the percentage of fibers with centrally located nuclei were observed in the tissue between all study

groups, showing an average of about 2% of the fibers containing centrally located nuclei (Figure 4.6F). Individual fiber morphology (cross-sectional area, circularity, and roundness) was also measured and the batched quantified fiber populations were analyzed for animals treated with saline (7,946 fibers), SKM hydrogel (8,302 fibers), and hUC hydrogel (6,000 fibers) compare to healthy tissue (9,130 fibers). First, the distribution of fiber cross-sectional area was determined to confirm there were no dramatic morphological changes as shown by all treatment groups having similar distribution curves (Figure 4.6G). For example, the average fiber area may not have changed, but a shift to a bimodal population distribution could have occurred, which would indicate abnormal muscle tissue. Fiber population averages (Figure 4.6H) showed that the SKM hydrogel was not significantly different than the healthy tissue. In contrast, the hUC hydrogel was significantly higher than the SKM hydrogel ($P<0.001$) and healthy tissue ($P<0.01$), and saline was significantly less ($P<0.001$) than all three other groups. Next, fiber circularity was measured by calculating the ratio of the short axis diameter to the long axis diameter. A histogram of the circularity distribution showed no major shifts in the total analyzed muscle fiber population (Figure 4.6I); however, all three treatment groups were measured to be significantly less ($P<0.001$) than healthy tissue, with the SKM hydrogel being the closest, and significantly greater than the hUC hydrogel ($P<0.001$) and saline ($P<0.05$). Lastly, fiber roundness was assessed as a means of investigating roughness or angularity of the muscle fibers. Both saline and the SKM hydrogel were not significantly different from

the healthy tissue, but hUC was significantly less (P<0.05). Thus, muscle fiber population analysis indicates that the treatments did not cause dramatic shifts in fiber cross-sectional area, circularity, or roundness population distributions, but averages of these values indicated that the SKM treated animals' muscle fibers most closely matched those of the healthy tissue for all three measured parameters.

Muscle fiber types were then labeled with ATPase staining and quantification of the percent cross-sectional area of the gracilis muscle staining for Type-1 fibers averaged around 6% with no significant variation between the treatment groups and the healthy tissue (Figure 4.6M). It was noted that significant regional variation of the Type-1 (dark staining) fibers was observed (Figure 4.6N) in the healthy tissue and all treatment groups. Typical morphology was seen with Type-1, slow oxidative, fibers being present near the larger vessel clusters. This morphology produced regions with a low-density of Type-1 fibers (Figure 4.6O) as well as regions of high-density (Figure 4.6P). Thus, undesirable shifts after treatment were not observed in the total fiber content type or regional organization.

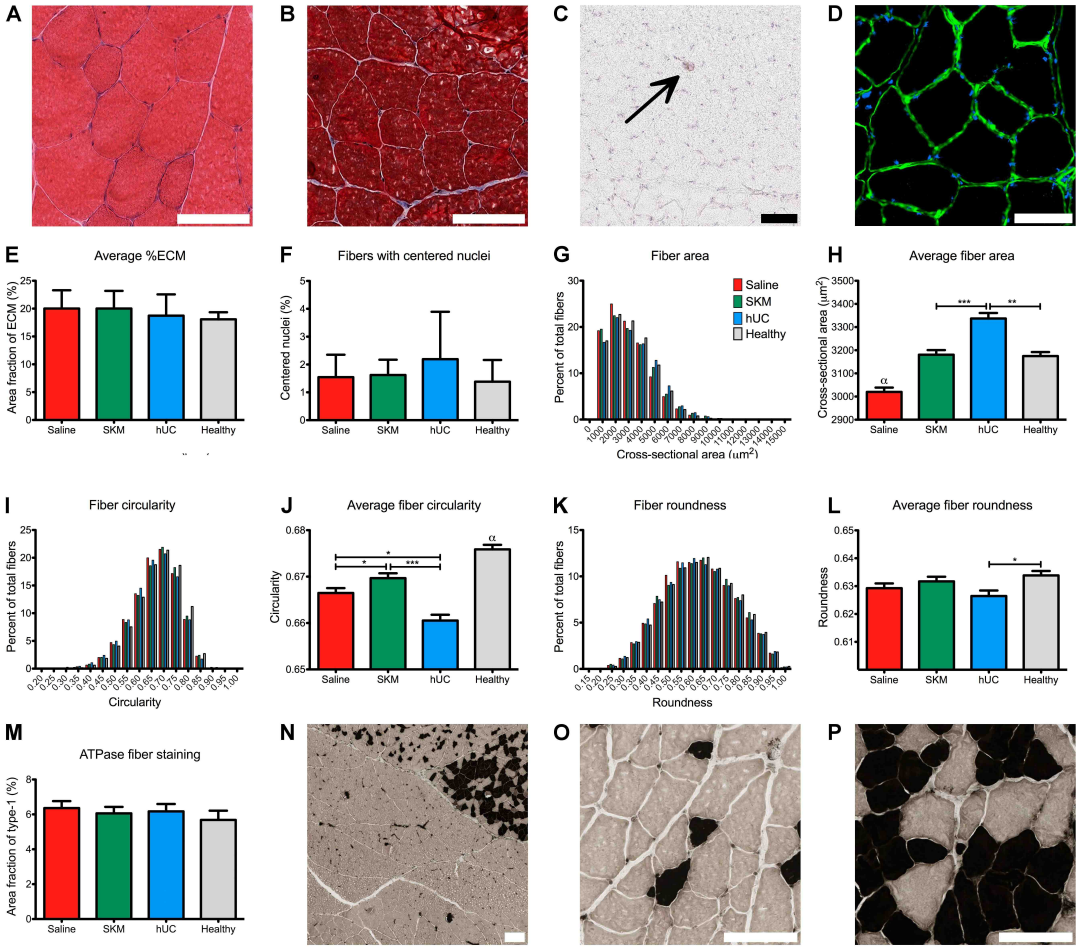

Figure 4.6: Biocompatibility assessment and muscle fiber morphology quantification. (**A**) Representative image of a hematoxylin and eosin (H&E) stained transverse section of muscle tissue from a SKM hydrogel treated animal showing healthy fiber morphology. (**B**) An image of a section stained with Mason's Trichrome, which was analyzed and indicated no macro-scar formation. (**C**) The potential for chronic inflammation was assessed by staining macrophages with CD68 as shown (black arrow) and no regions of inflammation were observed. (**D**) The ECM was stained with a laminin antibody (green) and nuclei were counter stained (blue) providing an outline of the muscle fibers. (**E**) Percent ECM was measured from laminin stained slides and showed no increase in interstitial ECM deposition compared to the healthy tissue. (**F**) Percent of fibers with centrally located nuclei did not vary compared to healthy tissue. (**G**) Histogram of fiber cross-sectional area analysis. (**H**) Average fiber area from the SKM group most closely matched the healthy tissue. (**I**) Histogram of fiber circularity analysis. (**J**) Average fiber circularity was significantly higher in the SKM group, which was closest to the healthy tissue. (**K**) Histogram of fiber roundness analysis. (**L**) Average fiber roundness was only significantly less for the hUC treatment group. (**M**) ATPase staining was used to quantify percent area of Type-1 muscle fibers. (**N**) Regional variation of Type-1 (dark staining) fiber density was observed for all groups (scale bar is 200 μm). (**O**) Regions of low-density Type-1 fibers and (**P**) high-density are shown. Unless noted, scale bars are 100 μm and all images are representative from an SKM hydrogel treated animal. **P*<0.05, ***P*<0.01, ****P*<0.001, and α*P*<0.001 compared to all other groups (Kruskal-Wallis Test followed by a Dunn's Multiple Comparison Test). Error bars are standard deviation (SD) for **E** and **F**.

4.3 Discussion

Patients with advanced PAD who are not eligible for revascularization interventions have limited options and often require partial or complete limb amputation. Various therapeutic angiogenesis approaches including cells, growth factors, and gene therapy have been explored, but have been met with mixed results in clinical trials [166]. Here, we take a novel approach using an injectable biomaterial scaffold to stimulate neovascularization and recruitment of endogenous progenitors. A biomaterial only therapeutic approach could have several advantages compared to the existing paradigm including off-the-shelf availability, reduced cost, and the ability to stimulate endogenous cell recruitment over multiple days or weeks. In this study, we demonstrate proof-of-concept for using an injectable ECM based hydrogel for treating PAD, showing increased perfusion in a hindlimb ischemia model.

To quantify hindlimb tissue perfusion in our study, we utilized laser speckle contrast analysis (LASCA). Previous hindlimb ischemia studies have typically utilized the older technology of Doppler imaging, which takes a single static snapshot at a given time point after the onset of anesthesia to assess tissue perfusion [160, 161]. In contrast, with LASCA we were able to assess perfusion with dynamic full field instantaneous analysis to allow continuous monitoring of the perfusion in the limbs. This allowed for more accurate perfusion assessment and provided insight into the change in perfusion over the time course of a single reading. For comparison to these publications using Doppler, we reported perfusion measurements at 5 min and 10 min, in

addition to the equilibrium measurement. All three measurements showed a significant increase in hindlimb tissue perfusion after injection of the SKM or hUC hydrogels alone over the saline control. This improvement in perfusion started as early as day 28 (day 21 post-injection) and persisted out to day 42 post-surgery (day 35 post-injection). By using LASCA, hindlimb perfusion kinetics, defined as the ratio of the rate of change of perfusion in each limb during a single reading, was assessed for the first time in this study. Perfusion kinetics is a relevant clinical parameter for PAD as well. Patients with PAD have shown a decreased or slowed rate of perfusion in transition from states of lower perfusion to higher perfusion. The decreased rate of change of perfusion is associated with decreased vessel health in diseased patients [167]. Thus, this new perfusion kinetics measurement provides potential insight into the health or function of the vascular network and its ability to transition through a change in cardiovascular output. Animals in this study were initially placed under anesthesia using 5% Isoflurane and transitioned to 2.5% at the start of the perfusion readings. This change in level of anesthesia is associated with increased cardiac output and increased skeletal muscle blood flow [163]. By day 42 the perfusion kinetics were shown to return to healthy or initial starting levels only in the biomaterial treated animals. This indicates that the biomaterial may cause improved vessel network remodeling, leading to perfusion kinetics that more closely match a healthy animal. The increase in perfusion and restoration of hindlimb perfusion kinetics directly correlated with histological quantification, which showed an increased density of arterioles

with diameters over 75 μm. Capillary density at the sight of biomaterial injection was also quantified but showed no change between the treatment groups. This, along with other previously published data, indicates that a therapy impacting arteriogenesis and not angiogenesis may be more desirable for PAD patients [168, 169].

Decellularized ECMs, including those from xenogeneic sources and those processed into hydrogels, have been shown to promote tissue remodeling and healing in a variety of applications [29, 58, 170-172]. For example, one of the most widely studied decellularized ECMs, porcine small intestine submucosa (SIS), has shown minimal immune response and complete degradation leading to acceptance and not rejection as seen with xenogeneic full tissue implants [137]. This positive tissue remodeling process has been associated with Th2 lymphocytes [137, 173], which secrete anti-inflammatory and pro-remodeling cytokines including interleukin (IL)-10 [174]. Several studies have also shown this response shifts macrophages to a more M2 phenotype [111, 144, 175]. In this study, we likewise demonstrated the biocompatibility of both ECM derived hydrogels by examining the resolution 35 days post-injection, at which point both ECM hydrogels were completely degraded. Review of the tissue by a histopathologist concluded no differences between healthy tissue and the treated ischemic damaged tissue. Scarring, both macro scale and interstitially between muscle fibers, was not present in either treatment group. Chronic inflammation was also not present showing a positive end resolution after complete biomaterial degradation. Finally, there was no significant shift in the

number or regional distribution of Type-1 muscle fibers (slow oxidative) after treatment with either biomaterial. Thus, this histological analysis confirms that the delivery of either of these degradable ECM biomaterials resulted in a pro-remodeling response and did not cause tissue trauma, chronic inflammation, or scaring within the local tissue.

While several *in vitro* studies have shown the importance of ECM tissue specificity [27, 28, 176-178], limited studies have been performed to examine whether tissue specificity is necessary *in vivo*. In this study, we tested two different ECM derived hydrogels. The SKM hydrogel represents a tissue specific ECM approach for treating skeletal muscle, and had previously shown promising results in a short-term histology study in a rat hindlimb ischemia model [58]. For comparison, a new injectable hydrogel derived from human umbilical cords was developed as a non-tissue specific approach. This was an attractive tissue source because it is allogeneic and readily available with a potential for increased regeneration because of its age. *In vitro*, we show that there are some differences regarding the two tissue sources with respect to their effects on cell proliferation and migration, but *in vivo*, we demonstrate that both materials were capable of significantly enhancing perfusion over the saline control. When we examined various measures of skeletal muscle remodeling post-ischemic injury, we found that overall the SKM hydrogel treated animals most closely matched the morphology of healthy skeletal muscle and were significantly different than the hUC hydrogel treated animals. Taken together, these results indicate that non-specific responses such as

vascularization may be possible with non-tissue specific ECM derived hydrogels, but they also indicate that tissue specificity could be important for overall tissue remodeling. These results are not surprising given that each tissue in the body is derived of a unique ECM composition that creates a specific cellular niche and can be correlated to total tissue function. Previously, several *in vitro* studies for cells derived from cardiac, neuronal, skeletal muscle, lung, cartilage, and liver tissues have shown increased differentiation or maturation when cultured on tissue specific ECM coatings [27, 28, 176-178]. In earlier studies, we showed that SKM increased differentiation of skeletal myoblasts [27], and that intramuscular injection of the SKM hydrogel led to a significant increase in proliferating cells ($Ki67^+$) with Desmin co-staining and an increase in muscle progenitor ($MyoD^+$) cell infiltration during the first two weeks post-injection [58]. These data suggest that the SKM hydrogel may be acting on resident progenitors to improve skeletal muscle remodeling.

Limitations of this study are due to the inherent weaknesses of hindlimb ischemia preclinical models. This is one of the major challenges in testing and translating therapies for PAD patients. The first limitation is intrinsic to the baseline mechanism of the disease, which is chronic decreased blood flow. This chronic state is difficult to simulate from an acute injury as done in current animal models due to the natural formation of collateral vessels [179]. Even large animal models and other rodent models with modifications to further mimic aspects of the patient population, such as those that are hyperhomocysteinemic, diabetic, hypercholesterolemic, and/or aged, still show

collateral vessel formation [179]. To address this limitation and more closely model the PAD patient population, we selected a more severe vessel ligation and excision protocol and injected the biomaterial 7 days post-ischemic injury. The surgery alone elicits an acute immune response and a wound-healing cascade. Waiting a week before applying the therapy allows for the initial formation of collaterals in the native tissue and some tissue recovery. Thus, the application of the biomaterial stimulated increased perfusion above this native healing process. Here, our model shows decreased resting perfusion after saline injection out to 42 days post-surgery (~65 %) with the majority of recovery occurring in the first two weeks. The small scale is another limitation of these animal models. Here we delivered a single bolus into the ischemic damaged region, whereas in human patients multiple injections would be utilized. Also, multiple treatment time points could be used to continuously stimulate the vessel growth over a period of months instead of weeks as shown here. Notably, all of these animal models show stimulation and increased perfusion from preexisting healthy vasculature whereas human patients with PAD have diseased vasculature, which could alter responses to these therapies.

In conclusion, we have shown the efficacy of an injectable biomaterial alone (SKM or hUC) to increase tissue perfusion in a hindlimb ischemia study. Significant differences in muscle remodeling indicate that utilizing a tissue specific therapy for PAD may be more desirable. GMP manufacturing and additional toxicology studies will be required prior to translation; however, this

functional study combined with a previous histological study [58] provides support for the advancement of the SKM hydrogel into clinical trials for treating patients with PAD.

4.4 Materials and Methods

4.4.1 ECM hydrogel development and characterization

The methods for producing the porcine skeletal muscle matrix (SKM) were modified from our previously published protocol [27, 58]. Briefly, psoas muscle was harvested from Yorkshire farm pigs, approximately 30-45 kg, immediately after euthanasia. All dermal tissue, subcutaneous fat and connective tissue were dissected away. The tissue was then chopped into small cubed pieces about 3-5 mm in length and rinsed in water for 30-45 min. After rinsing, the tissue was spun in 1% (w/v) sodium dodecyl sulfate (SDS) (Fischer Scientific, Fair Lawn, NJ) in phosphate buffered saline (PBS) with 0.5% penicillin streptomycin (PS) of 10,000 U/mL (Gibco, Life Technologies, Grand Island, NY) for 2 hours. The tissue was then rinsed and transferred to new SDS solution with PS for 3-5 days with daily solution changes to remove the cellular content. Once fully white, the tissue was rinsed in ultra pure water for 2 hours and then placed into isopropyl alcohol (IPA) (Fischer Scientific, Fair Lawn, NJ) for 18-24 hours for lipid removal. Next, tissue was rinsed twice and then spun for 30-45 min in 0.001% Triton X-100 solution (Sigma-Aldrich, St. Louis, MO). Finally the tissue was rinsed in water for 24 hours following by 2-5 additional rinses in water, freezing at -80 °C, and lyophilizing. The lyophilized

material was then milled into a fine powder using a Wiley® Mini-Mill and a #40 sieve. ECM samples from three different pigs were combined to form a batched material that was used for all analysis and testing.

For human umbilical cord tissue (hUC) collection, pregnant subjects delivering viable fetuses between 36-42 weeks gestation, without complications that would affect the umbilical cord, were consented under an institutionally approved protocol. Excess hUC tissue was collected after routine delivery procedures were completed. Fresh tissue was kept on ice during transfer and immediately processed with the following optimized decellularization protocol. Regions damaged by surgical clamping were removed and the healthy tissue was cut transversely into 0.5 cm length disks. Each disk was cut into 5-8 even pieces and 15-20 grams of tissue were rinsed in ultra pure water for 30-45 minutes to remove remaining blood. Next, the tissue was placed into SDS solution as used for the porcine skeletal muscle matrix decellularization described above for 2 hours and then for 5-7 days with daily solution changes. After complete decellularization the material was shaken twice and spun in Triton solution for 30-45 min as described above. After rinsing for 24 hours by spinning in water, the tissue was placed into 50 mL conicals contain a DNase/RNase solution and incubated on a shaker place at 37 °C for 18-24 hours. The DNase/RNase solution was comprised of 40 U/mL DNase (Sigma-Aldrich, St. Louis, MO) and 1 U/mL RNase A (Qiagen, Hilden, Germany) in 10 mM sodium chloride, 1 mM calcium chloride, 6 mM magnesium chloride, and 40 mM tri-hydrochloric acid at pH 7.4. The tissue

was rinsed and placed into new SDS solution for 24 hours and then rinsed for 30-45 minutes in 0.001% Triton X-100. The ECM was then rinsed, frozen, and lyophilized as described for the SKM. The lyophilized hUC was milled with a Wiley® Mini-Mill and a #60 sieve. ECM from four different patients was combined to form a batched material that was used for all analysis and testing.

Both SKM and hUC milled materials were digested using a previously described protocol [58]. Briefly, the powder form was digested at 10 mg/mL in a solution of pepsin at 1 mg/mL (Sigma, St. Louis, MO) in 0.1 M HCl for 48 hours. Once digested into a liquid form, the material was brought to a pH of 7.4 on ice while stirring using chilled 1.0 M NaOH. Next, the salt concentration was adjusted to 1x PBS by addition of 10x PBS. Finally, the ECM concentration was lowered to 6 mg of ECM/ml with 1x PBS. All solutions used were sterile filtered and pre-chilled in an ice and water slurry. The material was then frozen and lyophilized for storage in at -80 °C. Upon use, the material was thawed and brought back to a material concentration of 6 mg of ECM/mL with sterile ultra pure water.

Fresh frozen samples of decellularized tissue were cryo-sectioned and stained with Hematoxylin and Eosin (H&E). Bright field images were taken with a Carl Zeiss Observer D1 or Leica Aperio ScanScope® CS^2. The dsDNA content was isolated (n=3) using a NucleoSpin® Tissue kit (Macherey-Nagel, Duren, Germany). The nucleic acid composition was quantified (n=3) with a Thermo Scientific NanoDrop 2000c spectrophotometer and the dsDNA content was measured (n=3) by using a Quint-iT™ PicoGreen® dsDNA Assay Kit

(Invitrogen, Eugene, OR). Sulfated glycosaminoglycan (sGAG) content was quantified (n=3) with a previously published DMMB protocol [112, 130]. Protein fragment molecular weights were characterized with SDS-PAGE and the fiber formation after self-assembly or gelation of each matrix was confirmed with scanning electron microscopy (SEM) as previously published [130].

4.4.2 *In vitro* proliferation and migration

The proliferation and migration of skeletal myoblasts (C2C12s) and two vascular cell types were investigated. The C2C12 cells were expanded on collagen-coated plates and studies were performed with P10-14 cells. The two vascular cell types were rat aortic smooth muscle cells (RASMCs) and human coronary artery endothelial cells (HCAECs). The RASMCs were expanded on collagen-coated plates using P6-10 and were isolated as previously described [47, 115]. Growth culture media consisting of Dulbecco's Modified Eagle's Medium (DMEM) (Corning Cellgro, Manassas, VA) with 1% Penicillin Streptomycin (PS) (Gibco, Life Technologies, Grand Island, NY) and 10% Fetal Bovine Serum (FBS) (Sigma-Aldrich, St. Louis, MO) was used for expanding and experimentation of the C2C12 cells and RASMCs. The HCAECs (Cell Applications Inc., San Diego, CA) of passage P6-8 were cultured in MesoEndo Endothelial cell media (Cell Applications).

All *in vitro* experiments were done with ECM coatings created by using a previously published protocol [27]. Briefly, coatings were applied to polystyrene TC plastic surfaces by dilution the matrices down to 1 mg/mL with

sterile 0.1 M Acetic Acid. This ECM coating solution was then incubated on the culture surface for 1 hour at 37 °C and the surface then rinsed with PBS 2-3 times before plating cells. Proliferation of all three cell types was implemented following a previously reported protocol [130]. Experiments were run in a 96-well microtiter plate and coated with SKM or hUC . Each well (n=8) was seeded with 5 x 10^2 cells and cultured for 24 hours before the first media change. Cells were then cultured for a total of 3 or 5 days with media changes every two days. Relative proliferation was then quantified by measuring the dsDNA content using a Quanti-iT™ PicoGreeen® dsDNA Assay Kit (Invitrogen, Eugene, OR). Migration for all cells types was assessed using a tilt migration assay to measure the progression of a linear moving cell front on each of the coated surfaces based on a previously published protocol [180]. The horizontal surface or primary floor of T75 (C2C12s and RASMCs) or T25 (HCAECs) flasks was coated with SKM or hUC as described above. The flasks were then placed vertical for seeding with 5 x 10^3 cells in each flask. After culturing for 24 hours until confluence, the media was changed and the flasks were tilted to 75 degrees from horizontal to transition the linear cell front onto the primary horizontal surface for 24 hours. Media was once again replaced and the flasks were placed horizontally for the remainder of the experiment. Cell front displacements were measured using bright field microscopy. Migration was measured after 24 hours and 48 hours of culture on each coated surface (n=6).

4.4.3 Hindlimb ischemia surgery and biomaterial injection

All experiments in this study were performed in accordance with the guidelines established by the Institutional Animal Care and Use Committee at the University of California, San Diego, and the American Association for Accreditation of Laboratory Animal Care. Studies were done with 30 female Sprague Dawley (SD) rats ranging in weights of 220-265 g.

For the hindlimb ischemia surgery, animals were anesthetized with 2.5% Isoflurane gas using a Kent Scientific PhysioSuite^{TM} ventilator system. Unilateral ischemia damage was applied to the animals' right limb by ligation and removal of segments from the femoral artery and vein starting proximal to the epigastric artery. First, the surgical site was shaved and cleaned with betadine and isopropanol along with delivery of 1% licocaine subcutaneously along the incision site. The targeted vessels were visualized by creating an incision overlying the proximal, medial portion of the right hindlimb. The femoral artery and vein were dissected away from the femoral nerve and ligated to target the proximal removal of a 2 cm segment. Any major branches along the 2 cm segment, including the epigastric artery, were cauterized or ligated before excision to minimize bleeding. The entry incision through the skin was then closed using a mattress suture (5-O silk). Postoperatively, all animals were regularly monitored and analgesia (Buprenorphine at 0.05 mg/kg) was administered immediately upon regaining consciousness.

Animals were arbitrarily selected for treatment with the SKM hydrogel (n=9), hUC hydrogel (n=10), or saline (n=11) on day 7 post-ischemia. The

injection site was prepared by shaving if needed followed by cleaning with betadine and isopropanol. A single injection of 150 µL was performed using a 25 G needle through a small incision in the skin to visualize the muscle for consistent delivery into the gracilis muscle. The small incision in the skin was then closed using a single square knot suture (5-O silk).

4.4.4 Hindlimb functional perfusion measurements

Perfusion measurements were implemented using Laser Speckle Contrast Analysis (LASCA) with a PeriCam PSI System (PeriMed, Stockholm, Sweden). LASCA can instantaneously visualize real-time blood perfusion through measuring dynamic backscattering of light from a 785 nm laser leading to full-field high-resolution analysis [181, 182]. All readings were done with the following settings: working distance of 20 cm, high point density, 0.42 images/s, frame rate of 25 images/s, recorded with averaging of 50 images, effective frame rate of 0.5 images/s, and intensity filter from 0.20-10.0. Intensity filter was used to exclude all background signal and only include signal created by the animal. Animals were initially anesthetized with 5% Isoflurane under constant flow and then transferred to 2.5% Isoflurane using a Kent Scientific PhysioSuite™ ventilator system in the prone position. Readings were performed at the same time of day, with constant light exposure and room temperature. The animals were maintained on a heated insulated deck and internal body temperature was monitored during the full length of the reading. Readings were continuously taken for a minimum of 20

min or until the perfusion measurements reached a plateau for at least 5 min. Regions of interest (ROIs) were utilized to target each hairless plantar sole region individually [161] for assessment after 5 min, 10 min, and final or equilibrium perfusion readings. Percent perfusion was calculated as a ratio of the ischemic limb (right) to the healthy limb (left). Measurements were taken on day 0 before and immediately after the ischemic surgery and then on days 5, 10, 14, 21, 28, 35, and 42. Perfusion kinetics were calculated by dividing the slope of the linear region of the ischemic limb by the slope of linear region of the healthy limb. Readings were excluded from perfusion kinetics analysis if the animal woke up during the initial reading or no linear region was identifiable due to an irregular perfusion measurement.

4.4.5 Histological analysis

On day 42 the injected hindlimb muscle region and corresponding healthy limb tissue was excised. The tissue was placed in physiological orientation and morphology on a filter paper and flash frozen in isopentane chilled with liquid nitrogen. The tissue was then blocked in OCT to allow for transverse sectioning of the tissue and flash frozen again in isopentane chilled with liquid nitrogen. Sections of 10 μm thickness were taken at seven different locations evenly spaced spanning the majority of the muscle segment. All histological imaging was done with either a Leica Aperio ScanScope® CS^2 or a Leica Ariol®. Tissue was stained with Hematoxylin and Eosin (H&E) or Mason's Trichrome for histological analysis. Immunohistochemistry was used

to stain vessels, laminin, and macrophages. Arterioles were labeled with an alpha-smooth muscle actin (αSMA) antibody (Dako, Carpinteria, California; 1:75) and an Alexa Fluor 488 conjugated secondary antibody (Invitrogen, Carlsbad, California; 1:500), and nuclei were counterstained with Hoechst 33342. Arterioles were quantified from 8 randomly selected 10x images from 5 different slides per limb for a total of 40 images per sample. For arterioles with a diameter of over 10 μm the major axis, minor axis, and total internal lumen area were measured with ImageJ (NIH, Bethesda, MD). Arteriole diameter was reported as the average of the major and minor axis. Capillaries were stained using Alkaline Phosphatase chromagen (BCIP/NBT) (Abcam, Cambridge, MA) staining on fresh frozen slides. Capillary density was automatically quantified using a custom assay as part of the Leica Ariol® system and was applied to 10 randomly selected 20x regions from 5 slides per sample. Macrophages were labeled with an anti-CD68 antibody (Santa Cruiz Biotechnology, Santa Cruz, CA; 1:50) and visualized with horseradish peroxidase (HRP) conjugated goat anti-mouse IgG (Abcam, Cambridge, MA; 1:100) and Metal Enhanced DAB Substrate Kit (Thermo Scientific, Rockford, IL). The interstitial ECM was labeled with an anti-laminin antibody (Sigma-Aldrich, St. Louis, MO; 1:200) and an Alexa Fluor 568 conjugated secondary antibody (Invitrogen, Carlsbad, California; 1:500), and nuclei were counterstained with Hoechst 33342. The percent ECM was calculated by using threshold analysis from an automated assay as part of the Leica Ariol® system from 5 randomly selected 10x regions from 5 different slides per

sample. Fibers with centered nuclei and fiber morphology were measured from 5 randomly selected 20x images from 5 different slides per sample. Fibers with centered nuclei were manually counted and divided by the total number of fibers assessed to calculate percent fibers with centered nuclei. Fiber morphology was measured using a custom ImageJ Macro for a total of about 1,000 fibers per sample. Fiber type staining was done at pH 4.31 following previously published methods [183, 184]. Fiber type quantification was implemented by total tissue analysis using intensity threshold gating with Positive Pixel Count as part of the Aperio ImageScope software. The entire tissue section from five different slides per sample was analyzed excluding all sectioning artifacts, large vessels, and background regions. Percent Type-1 fiber area was calculated by dividing the total positive area for Type-1 fiber staining (high color intensity) by total tissue area analyzed.

4.4.6 Statistical analysis

Material characterization data and all *in vitro* data was analyzed with a Students *t*-test. The perfusion data was analyzed using a one-way ANOVA with a Tukey post-hoc test. Vessel quantification was analyzed using a one-way ANOVA with a Dunnett's post-hoc test. Total fiber population morphology data was analyzed using a Kruskal-Wallis test followed by a Dunn's Multiple Comparison Test. Data are means ± SEM unless otherwise noted. Significance was accepted at $P<0.05$.

4.5 Acknowledgments

The authors would like to thank Carolina Rodgers and Sandra Leon-Garcia (supervised by Dr. Louise Laurent) for their help with harvesting tissue samples, and Matt Joens from the Waitt Advanced Biophotonics Center at the Salk Institute for his expertise with SEM. Funding: Funding was provided in part by the NIH Heart, Lung, Blood Institute 5R01HL113468 and an American Heart Association Western States Innovative Sciences Award. Ms. Leon-Garcia and Dr. Laurent were supported by funds from the UCSD Department of Reproductive Medicine. TDJ would like to thank his funding sources including the NSF as a Graduate Student Research Fellow, the NHLBI as a Training Grant Recipient, and the Charles Lee Powel Foundation as a Powell Fellow. Author contributions: KLC and EM obtained the funding. KLC, EM, and TDJ designed the experiments. TDJ and RLB executed all small-animal surgeries. The acquisition and/or analysis of data was handled by TDJ, DIE, JLU, and KGO. Drafting and/or revising the manuscript for critical content was executed by TDJ, JLU, DIE, RLB, KGO, EM and KLC. Administrative, technical, or supervisory tasks were handled by KLC. Competing interests: KLC is co-founder, board member, and holds equity interest in Ventrix, Inc. KLC is an inventor on patent applications (US20110189140, US2012054058) associated with this work and owned by the University of California, San Diego.

Chapter 4, in full, is submitted for publication. Ungerlieder, Jessica; Hernandez, Melissa; Elhag, Dean; Braden, Rebecca; Osborn, Kent; Mahmud,

Ehtisham; and Christman, Karen L. The dissertation author was the primary investigator and author of this paper.

CONCLUSION

In this thesis several major advances to the field of naturally derived injectable biomaterials for treating cardiovascular disease were presented. These studies more specifically focused on the treatment of heart failure after a heart attack and treating peripheral artery disease in the limbs. Both diseases have several similarities including being caused by the build of atherosclerotic plaque that then leads to down stream ischemic damaged muscle. The main difference between the two diseases is that MI is an acute trauma whereas PAD is a chronic disease. The first step in this thesis was to gain a greater understanding of these ECM materials by studying a porcine myocardial matrix (PMM), a previously developed therapy for treating heart failure after MI, and to study its gelation parameters. From this it was shown that the gelation of the material is sensitive to variations in temperature and salt concentration leading to the conclusion that these materials can be altered or modified depending on the application. The next advancement of note was the development of two novel human sourced biomaterials including a human umbilical cord matrix (hUC) and a human myocardial matrix (HMM). Each of these materials was then utilized as a tool for testing important questions in the field.

The HMM material was initially compared to the previously developed PMM to investigate the importance of human versus porcine tissue sourcing. Although the human sourced material performed relatively similarly to the porcine material several issues arose in the handling and processing stages.

Most notable was the dramatic variability between the human cadaveric hearts in terms of gross anatomy with lipid deposition on the epicardial surface, size of the hearts, and time needed to fully decellularize the tissue. Also, most of the decellularized human hearts could not form hydrogels at physiological conditions and thus were not usable for analysis. These unfortunate differences, potentially due to increased age of the tissue source, lead to the conclusion that human cadaveric hearts are not an appropriate source for developing a myocardial matrix and that future preclinical and clinical studies should be continued with the PMM. This conclusion of increased challenges and variability can be applied for any new therapy attempting to utilize aged cadaveric human tissue for developing ECM biomaterials.

Although not a viable candidate for clinical translation, the HMM can still be utilized as a tool for other *in vivo* and *in vitro* tests. For example, the HMM was used as an allogeneic material to help test the hypothesis that a humanized mouse model would be able to differentiate between xenogeneic and allogeneic biomaterials. After investigation with histology, qRT-PCR, immunohistochemistry and flow cytometry it was shown that the humanized mouse model could differentiate between a xenogeneic or allogeneic material. It was also shown that these decellularized biomaterials elicit a T-cell mediate immune response and should be tested in immune competent animals. This supported the conclusion that if testing an allogeneic material for preclinical work it would be desirable to use a humanized mouse model since the human immune response would not be properly mimicked by a wild type non-human

immune system. This study also confirmed reports in the literature that a xenogeneic material causes a pro-remodeling response by Th2 and M2 polarization and this desirable outcome was maintained in the humanized mouse model as well.

The second new biomaterial, hUC, was utilized for comparison against a tissue specific material, porcine skeletal muscle matrix (SKM), to test the importance of tissue sourcing in developing new ECM therapies. After testing in a hindlimb ischemia model both materials were successful in increasing the non-tissue specific related parameter of total tissue perfusion, but some differences were seen after histological analysis. One of the main differences was that the SKM material produced muscle fibers that most closely matched muscle fibers from the healthy limb in terms of cross-sectional area, roundness, and circularity. Thus, this supports the conclusion that a tissue specific ECM therapy could produce more desirable clinical outcomes than a non-tissue specific therapy.

Although these studies show an advancement in our understanding of these biomaterials including the gelation parameters, species tissue sourcing, and tissue specific sourcing, there are several areas that should be investigated in future studies. Theses areas include optimizing of currently tested therapies for the clinic, expanding into investigating the impact of diseased ECM on tissue health, and understanding their mechanism of action for stimulating regeneration. Currently investigated therapies including the SKM material, are on the verge of moving towards clinical translation.

However, several steps for the SKM material need to be investigated first, such as scale up manufacturing and optimization for delivery into humans. Present studies involved a single bolus delivery of the material into a rat hindlimb. In human patients this will need to be scaled up and will probably include multiple injections over the whole leg and at numerous different time points as well. Even with these hurdles in transitioning into the clinic the SKM material has shown great promise for treating patients with PAD.

Although all the current studies presented in this thesis involved the use of healthy sourced ECM to treat damaged tissue the same methods could be used to isolate diseased ECM. For example, the decellularization techniques could be applied to isolate ECM from ischemic damaged tissue. The material could then be used as a tool *in vitro* in 2D or 3D to model a diseased environment. Culturing relevant cells types on this diseased ECM could provide insight into the importance of ECM composition on cellular pathological states. From this a greater understanding of disease conditions could help guide the design of future therapies.

The next major step in the development of these decellularized biomaterials for clinic is to gain a greater understanding of their mechanism of action. Although advancements have been made in understanding the type of immune response elicited by these biomaterials, as investigated in this thesis, a more detailed and thorough understanding is needed. Studying the mechanism of action should start by investigating the impact of the materials on local tissue gene expression. From this studies should be targeted at the

corresponding shift of transcription factors and a full proteomics analysis to determine a change in the cytokine profile as well. This data would then be analyzed with a systems approach to characterize shifts in the metabolic processes, thus indicating the specific mechanisms of action caused by these materials. Creating a detailed understanding of the mechanism of action will provide further insight into how the materials can be optimized for improved clinical outcomes.

Impacts to the Field

The work presented here impacts the future of the field of naturally derived biomaterials by exploring the development of allogeneic biomaterials, utilizing the humanized mouse model, presenting a biomaterial alone therapy for PAD, and showing potential for tissue specific therapies. First, allogeneic biomaterials have several advantages as previously presented, but in terms of scale up and clinical translation they are not always a viable option. In this thesis, two new human based biomaterials were presented. The first, human myocardial matrix was from aged human cadaveric donor hearts and showed significant patient-to-patient variability. This along with other challenges with tissue access severely limited the capacity for this materials use in the clinic. However, these issues were not seen with the human umbilical cord. Sourced from young readily available tissue, this material showed promise for clinical translation and scale up. Thus, not all allogeneic tissue sources are

appropriate for clinical translation and the challenges for development vary depending on tissue type and patient age.

The second impact for the field was the utilization of the humanized mouse model for preclinical biomaterial testing. It was shown that the model could differentiate between allogeneic and xenogeneic materials, this potentially changes the way naturally derived biomaterials should be tested. Allogeneic materials could have a different immune response in human patients that is not properly mimicked by the current standards for biomaterial biocompatibility testing. The humanized mouse model could improve the *in vivo* modeling of the human immune response for these materials. This work shows the value and potential application to help improve the testing of these biomaterials by providing a new tool for the field to model the human immune response.

The use of the humanized mouse also brought up concern about the potential clinical outcomes of using an allogeneic material. Here the infiltration of cells into the region was so low that it would likely not cause a regenerative response to the local tissue. As previously discussed, the immune response to these materials has been shown to be an important factor in creating a pro-remodeling outcome. With thorough decellularization of human tissue the remaining human ECM components are inherently not immunogenic. However, the humanized mouse is known to cause a weaker immune response and the subcutaneous space has a lesser response as well due to lower levels of vascularization as compared to other tissues, such as cardiac

tissue. Thus, further studies should be implemented in other tissues of the humanized mouse model and eventually in human patients to test the potential efficacy of allogeneic materials.

Thirdly, was showing the efficacy of a biomaterial alone approach for treating PAD. The biomaterial alone addressed the major parameter for PAD patients by increasing tissue perfusion after ischemic injury. This study paves the way for exploring biomaterial therapies further for treating PAD. Although the method still needs to be optimized including scaling up to multiple injections along the limb and studying the potential for numerous treatments over time. Future studies should be used to improve upon this work and optimize a biomaterial alone therapy for clinical translation to threat PAD.

Finally, the impact of tissue specific therapies was investigated. This work showed that an acceptable outcome could be achieved by non-tissue specific solutions. This could indicate the potential benefit that numerous diseases or tissues could be treated with a single naturally derived biomaterial, such as the human umbilical cord matrix. However, based off the data presented here and previous *in vitro* work, benefits could arise from a tissue specific solution. Even though a tissue specific therapy was not needed for increasing tissue perfusion, tissue specific benefits were observed in muscle fiber morphology. This type of tissue specific response could be crucial for other diseases, such as MI. Increasing perfusion alone would not be sufficient for an MI therapy. Additional cardiac specific benefits for remodeling of the local diseased myocardium would be crucial for improved cardiac functional

outcomes. Thus, although a tissue specific solution may not be required for all clinical diseases, such as PAD, it could have significant impact for certain diseases, such as MI.

In conclusion this work supports the continuation of SKM for further investigation and translation to the clinic as a therapy for treating PAD. Additional studies should be implemented in a large animal model of hind limb ischemia. This scale up would be important for testing the use of numerous smaller injections over a larger area and to test the application of numerous injections over a period of weeks to months. Also, perfusion should be more thoroughly analyzed with micro-CT in order to directly visualize and quantify the remodeling of the vessel network. Following the success of these studies would be the need to scale up production of the material and begin clinical trials in human patients.

Finally, efforts should be additionally focused on increasing our knowledge of the mechanism of action of these ECM biomaterials. Here we showed that our decellularization process produced matrices that favored a pro-remodeling inflammatory response in support of previous claims in the literature. However, the exact mechanism of action, in terms of shifts in metabolic processes, is unknown. This could be investigated by measuring changes in gene expression and corresponding proteome due to the presence of the biomaterial alone. Elucidating the mechanism of action will provide a stronger foundation of knowledge from which future materials can be designed and optimized for improved clinical outcomes.

References

1. Go AS, Mozaffarian D, Roger VL, Benjamin EJ, Berry JD, Borden WB, Bravata DM, Dai S, Ford ES, Fox CS, Franco S, Fullerton HJ, Gillespie C, Hailpern SM, Heit JA, Howard VJ, Huffman MD, Kissela BM, Kittner SJ, Lackland DT, Lichtman JH, Lisabeth LD, Magid D, Marcus GM, Marelli A, Matchar DB, McGuire DK, Mohler ER, Moy CS, Mussolino ME, Nichol G, Paynter NP, Schreiner PJ, Sorlie PD, Stein J, Turan TN, Virani SS, Wong ND, Woo D, Turner MB. Heart disease and stroke statistics--2013 update: A report from the american heart association. *Circulation*. 2013;127:e6-e245

2. Sutton MGSJ, Sharpe N. Left ventricular remodeling after myocardial infarction : Pathophysiology and therapy. 2000

3. Hirsch AT, Haskal ZJ, Hertzer NR, Bakal CW, Creager MA, Halperin JL, Hiratzka LF, Murphy WR, Olin JW, Puschett JB, Rosenfield KA, Sacks D, Stanley JC, Taylor LM, Jr., White CJ, White J, White RA, Antman EM, Smith SC, Jr., Adams CD, Anderson JL, Faxon DP, Fuster V, Gibbons RJ, Hunt SA, Jacobs AK, Nishimura R, Ornato JP, Page RL, Riegel B. Acc/aha 2005 practice guidelines for the management of patients with peripheral arterial disease (lower extremity, renal, mesenteric, and abdominal aortic). *Circulation*. 2006;113:e463-654

4. Lawall H, Bramlage P, Amann B. Stem cell and progenitor cell therapy in peripheral artery disease. A critical appraisal. *Thrombosis and haemostasis*. 2010;103:696-709

5. Adam DJ, Beard JD, Cleveland T, Bell J, Bradbury AW, Forbes JF, Fowkes FG, Gillepsie I, Ruckley CV, Raab G, Storkey H, participants Bt. Bypass versus angioplasty in severe ischaemia of the leg (basil): Multicentre, randomised controlled trial. *Lancet*. 2005;366:1925-1934

6. Giles KA, Pomposelli FB, Spence TL, Hamdan AD, Blattman SB, Panossian H, Schermerhorn ML. Infrapopliteal angioplasty for critical limb ischemia: Relation of transatlantic intersociety consensus class to outcome in 176 limbs. *Journal of vascular surgery*. 2008;48:128-136

7. Pomposelli FB, Kansal N, Hamdan AD, Belfield A, Sheahan M, Campbell DR, Skillman JJ, Logerfo FW. A decade of experience with dorsalis pedis artery bypass: Analysis of outcome in more than 1000 cases. *Journal of vascular surgery*. 2003;37:307-315

8. Dormandy J, Heeck L, Vig S. The fate of patients with critical leg ischemia. *Seminars in vascular surgery*. 1999;12:142-147

9. Marston WA, Davies SW, Armstrong B, Farber MA, Mendes RC, Fulton JJ, Keagy BA. Natural history of limbs with arterial insufficiency and chronic ulceration treated without revascularization. *Journal of vascular surgery*. 2006;44:108-114

10. Inferiori). TICAIGGdSdICCdA. Long-term mortality and its predictors in patients with critical leg ischaemia. *European journal of vascular and endovascular surgery : the official journal of the European Society for Vascular Surgery*. 1997;14:91-95

11. Tongers J, Roncalli JG, Losordo DW. Therapeutic angiogenesis for critical limb ischemia: Microvascular therapies coming of age. *Circulation*. 2008;118:9-16

12. Christman KL, Lee RJ. Biomaterials for the treatment of myocardial infarction. *Journal of the American College of Cardiology*. 2006;48:907-913

13. Rane AA, Christman KL. Biomaterials for the treatment of myocardial infarction: A 5-year update. *Journal of the American College of Cardiology*. 2011;58:2615-2629

14. Johnson TD, Christman KL. Injectable hydrogel therapies and their delivery strategies for treating myocardial infarction. *Expert Opin. Drug Deliv.* 2012:1-14

15. Li Z, Guan J. Hydrogels for cardiac tissue engineering. *Polymers*. 2011;3:740-761

16. Tous E, Purcell B, Ifkovits JL, Burdick JA. Injectable acellular hydrogels for cardiac repair. *Journal of cardiovascular translational research*. 2011;4:528-542

17. Wang H, Zhou J, Liu Z, Wang C. Injectable cardiac tissue engineering for the treatment of myocardial infarction. *Journal of Cellular and Molecular Medicine*. 2010

18. Ungerleider JL, Christman KL. Injectable biomaterials for the treatment of myocardial infarction and peripheral artery disease: Translational challenges and progress *Stem Cells Translational Medicine* 2014:In Press

19. Leor J, Tuvia S, Guetta V, Manczur F, Castel D, Willenz U, Petneházy Ö, Landa N, Feinberg MS, Konen E, Goitein O, Tsur-Gang O, Shaul M, Klapper L, Cohen S. Intracoronary injection of in situ forming alginate hydrogel reverses left ventricular remodeling after myocardial infarction

in swine. *Journal of the American College of Cardiology*. 2009;54:1014-1023

20. Dib N, Campbell A, Jacoby DB, Zawadzka A, Ratliff J, Miedzybrocki BM, Gahremanpour A, Diethrich EB, Opie SR. Safety and feasibility of percutaneous autologous skeletal myoblast transplantation in the coil-infarcted swine myocardium. *J Pharmacol Toxicol Methods*. 2006;54:71-77

21. Gilbert T, Sellaro T. Decellularization of tissues and organs. *Biomaterials*. 2006

22. Hoshiba T, Lu H, Kawazoe N, Chen G. Decellularized matrices for tissue engineering. *Expert Opin. Biol. Ther.* 2010;10:1717-1728

23. Crapo PM, Gilbert TW, Badylak SF. An overview of tissue and whole organ decellularization processes. *Biomaterials*. 2011;32:3233-3243

24. Schaner PJ, Martin ND, Tulenko TN, Shapiro IM, Tarola NA, Leichter RF, Carabasi RA, Dimuzio PJ. Decellularized vein as a potential scaffold for vascular tissue engineering. *J. Vasc. Surg.* 2004;40:146-153

25. Ott HC, Matthiesen TS, Goh S-K, Black LD, Kren SM, Netoff TI, Taylor DA. Perfusion-decellularized matrix: Using nature's platform to engineer a bioartificial heart. *Nat Med*. 2008;14:213-221

26. Elkins R, Dawson P, Goldstein S, Walsh S, Black K. Decellularized human valve allografts. *Ann Thorac Surg*. 2001;71:S428-S432

27. DeQuach JA, Mezzano V, Miglani A, Lange S, Keller GM, Sheikh F, Christman KL. Simple and high yielding method for preparing tissue specific extracellular matrix coatings for cell culture. *PloS one*. 2010;5:e13039

28. French KM, Boopathy AV, DeQuach JA, Chingozha L, Lu H, Christman KL, Davis ME. A naturally derived cardiac extracellular matrix enhances cardiac progenitor cell behavior in vitro. *Acta biomaterialia*. 2012

29. Seif-Naraghi SB, Singelyn JM, Salvatore MA, Osborn KG, Wang JJ, Sampat U, Kwan OL, Strachan GM, Wong J, Schup-Magoffin PJ, Braden RL, Bartels K, DeQuach JA, Preul M, Kinsey AM, Demaria AN, Dib N, Christman KL. Safety and efficacy of an injectable extracellular matrix hydrogel for treating myocardial infarction. *Science translational medicine*. 2013;5:173ra125

30. Cortiella J, Niles J, Cantu A, Brettler A, Pham A, Vargas G, Winston S, Wang J, Walls S, Nichols JE. Influence of acellular natural lung matrix on murine embryonic stem cell differentiation and tissue formation. *Tissue engineering. Part A*. 2010;16:2565-2580

31. Sellaro TL, Ravindra AK, Stolz DB, Badylak SF. Maintenance of hepatic sinusoidal endothelial cell phenotype in vitro using organ-specific extracellular matrix scaffolds. *Tissue engineering*. 2007;13:2301-2310

32. Cheng NC, Estes BT, Awad HA, Guilak F. Chondrogenic differentiation of adipose-derived adult stem cells by a porous scaffold derived from native articular cartilage extracellular matrix. *Tissue engineering. Part A*. 2009;15:231-241

33. Leor J, Amsalem Y, Cohen S. Cells, scaffolds, and molecules for myocardial tissue engineering. *Pharmacol Ther*. 2005;105:151-163

34. Badylak SF. The extracellular matrix as a biologic scaffold material. *Biomaterials*. 2007;28:3587-3593

35. Lutolf MP, Hubbell JA. Synthetic biomaterials as instructive extracellular microenvironments for morphogenesis in tissue engineering. *Nat Biotechnol*. 2005;23:47-55

36. Brown L. Cardiac extracellular matrix: A dynamic entity. *Am J Physiol Heart Circ Physiol*. 2005;289:H973-974

37. Alberts B, Johnson A, Lewis J, Raff M, Roberts K, Walter P. *Molecular biology of the cell. Fifth edition*. Garland Science; 2008.

38. Flemming RG, Murphy CJ, Abrams GA, Goodman SL, Nealey PF. Effects of synthetic micro- and nano-structured surfaces on cell behavior. *Biomaterials*. 1999;20:573-588

39. Barnes CP, Sell SA, Boland ED, Simpson DG, Bowlin GL. Nanofiber technology: Designing the next generation of tissue engineering scaffolds. *Advanced Drug Delivery Reviews*. 2007;59:1413-1433

40. Silver FH, Freeman JW, Seehra GP. Collagen self-assembly and the development of tendon mechanical properties. *Journal of Biomechanics*. 2003;36:1529-1553

41. Ingber D. How cells (might) sense microgravity. *The FASEB journal : official publication of the Federation of American Societies for Experimental Biology*. 1999;13 Suppl:S3-15

42. Koochekpour S, Merzak A, Pilkington GJ. Extracellular matrix proteins inhibit proliferation, upregulate migration and induce morphological changes in human glioma cell lines. *Eur J Cancer*. 1995;31A:375-380

43. Parenteau-Bareil R, Gauvin R, Berthod F. Collagen-based biomaterials for tissue engineering applications. *Materials*. 2010;3:1863-1887

44. Li W-J, Ko FK. Electrospun nanofibrous structure: A novel scaffold for tissue engineering. 2001:1-9

45. Drury JL, Mooney DJ. Hydrogels for tissue engineering: Scaffold design variables and applications. *Biomaterials*. 2003;24:4337-4351

46. Badylak SF, Gilbert TW. Immune response to biologic scaffold materials. *Semin. Immunol.* 2008;20:109-116

47. Singelyn JM, DeQuach JA, Seif-Naraghi SB, Littlefield RB, Schup-Magoffin PJ, Christman KL. Naturally derived myocardial matrix as an injectable scaffold for cardiac tissue engineering. *Biomaterials*. 2009;30:5409-5416

48. Okada M, Payne TR, Oshima H, Momoi N, Tobita K, Huard J. Differential efficacy of gels derived from small intestinal submucosa as an injectable biomaterial for myocardial infarct repair. *Biomaterials*. 2010;31:7678-7683

49. Seif-Naraghi SB, Salvatore MA, Schup-Magoffin PJ, Hu DP, Christman KL. Design and characterization of an injectable pericardial matrix gel: A potentially autologous scaffold for cardiac tissue engineering. *Tissue engineering. Part A*. 2010;16:2017-2027

50. Singelyn JM, Sundaramurthy P, Johnson TD, Schup-Magoffin PJ, Hu DP, Faulk DM, Wang J, Mayle KM, Bartels K, Salvatore M, Kinsey AM, Demaria AN, Dib N, Christman KL. Catheter-deliverable hydrogel derived from decellularized ventricular extracellular matrix increases endogenous cardiomyocytes and preserves cardiac function post-myocardial infarction. *Journal of the American College of Cardiology*. 2012;59:751-763

51. Raval Z, Losordo DW. Cell therapy of peripheral arterial disease: From experimental findings to clinical trials. *Circulation Research*. 2013;112:1288-1302

52. Powell RJ. Update on clinical trials evaluating the effect of biologic therapy in patients with critical limb ischemia. *Journal of vascular surgery*. 2012;56:264-266

53. Ouma GO, Jonas RA, Usman MH, Mohler ER, 3rd. Targets and delivery methods for therapeutic angiogenesis in peripheral artery disease. *Vascular medicine*. 2012;17:174-192

54. Menasche P. Cell therapy for peripheral arterial disease. *Curr Opin Mol Ther*. 2010;12:538-545

55. Segers VF, Lee RT. Local delivery of proteins and the use of self-assembling peptides. *Drug Discov Today*. 2007;12:561-568

56. Gupta R, Tongers J, Losordo DW. Human studies of angiogenic gene therapy. *Circ Res*. 2009;105:724-736

57. Radhakrishnan J, Krishnan UM, Sethuraman S. Hydrogel based injectable scaffolds for cardiac tissue regeneration. *Biotechnology advances*. 2014;32:449-461

58. Dequach JA, Lin JE, Cam C, Hu D, Salvatore MA, Sheikh F, Christman KL. Injectable skeletal muscle matrix hydrogel promotes neovascularization and muscle cell infiltration in a hindlimb ischemia model. *Eur Cell Mater*. 2012;23:400-412

59. Lee CH, Singla A, Lee Y. Biomedical applications of collagen. *Int J Pharm*. 2001;221:1-22

60. Williams BR, Gelman RA, Poppke DC, Piez KA. Collagen fibril formation. Optimal in vitro conditions and preliminary kinetic results. *The Journal of biological chemistry*. 1978;253:6578-6585

61. Rosenblatt J, Devereux B, Wallace DG. Injectable collagen as a ph-sensitive hydrogel. *Biomaterials*. 1994;15:985-995

62. Hayashi T, Nagai Y. Factors affecting the interactions of collagen molecules as observed by in vitro fibril formation. Iii. Non-helical regions of the collagen molecules. *Journal of biochemistry*. 1974;76:177-186

63. Gobeaux F, Mosser G, Anglo A, Panine P, Davidson P, Giraud-Guille M-M, Belamie E. Fibrillogenesis in dense collagen solutions: A physicochemical study. *Journal of molecular biology*. 2008;376:1509-1522

64. Raub CB, Unruh J, Suresh V, Krasieva T, Lindmo T, Gratton E, Tromberg BJ, George SC. Image correlation spectroscopy of multiphoton images correlates with collagen mechanical properties. *Biophysical journal*. 2008;94:2361-2373

65. Roeder BA, Kokini K, Sturgis JE, Robinson JP, Voytik-Harbin SL. Tensile mechanical properties of three-dimensional type i collagen extracellular matrices with varied microstructure. *Journal of Biomechanical Engineering*. 2002;124:214

66. Ott HC, Matthiesen TS, Goh S-K, Black LD, Kren SM, Netoff TI, Taylor DA. Perfusion-decellularized matrix: Using nature's platform to engineer a bioartificial heart. *Nature medicine*. 2008;14:213-221

67. Daamen WF, van Moerkerk HTB, Hafmans T, Buttafoco L, Poot AA, Veerkamp JH, van Kuppevelt TH. Preparation and evaluation of molecularly-defined collagen-elastin-glycosaminoglycan scaffolds for tissue engineering. *Biomaterials*. 2003;24:4001-4009

68. Ellis DL, Yannas IV. Recent advances in tissue synthesis in vivo by use of collagen-glycosaminoglycan copolymers. *Biomaterials*. 1996;17:291-299

69. Voytik-Harbin SL, Brightman AO, Waisner BZ, Robinson JP, Lamar CH. Small intestinal submucosa: A tissue-derived extracellular matrix that promotes tissue-specific growth and differentiation of cells in vitro. *Tissue engineering*. 1998;4:157-174

70. Badylak SF, Freytes DO, Gilbert TW. Extracellular matrix as a biological scaffold material: Structure and function. *Acta Biomaterialia*. 2009;5:1-13

71. Seif-Naraghi SB, Salvatore MA, Schup-Magoffin PJ, Hu DP, Christman KL. Design and characterization of an injectable pericardial matrix gel: A potentially autologous scaffold for cardiac tissue engineering. *Tissue engineering. Part A*. 2010;16:2017-2027

72. Freytes D, Martin J, Velankar S, Lee A. Preparation and rheological characterization of a gel form of the porcine urinary bladder matrix. *Biomaterials*. 2008

73. Young DA, Ibrahim DO, Hu D, Christman KL. Injectable hydrogel scaffold from decellularized human lipoaspirate. *Acta Biomaterialia*. 2011;7:1040-1049

74. Knapp PM, Lingeman JE, Siegel YI, Badylak SF, Demeter RJ. Biocompatibility of small-intestinal submucosa in urinary-tract as augmentation cystoplasty graft and injectable suspension. *J Endourol*. 1994;8:125-130

75. Singelyn JM, Christman KL. Modulation of material properties of a decellularized myocardial matrix scaffold. *Macromol Biosci*. 2011;11:731-738

76. Duan Y, Liu Z, O'Neill J, Wan LQ, Freytes DO, Vunjak-Novakovic G. Hybrid gel composed of native heart matrix and collagen induces cardiac differentiation of human embryonic stem cells without supplemental growth factors. *J. of Cardiovasc. Trans. Res.* 2011;4:605-615

77. Christman KL, Lee RJ. Biomaterials for the treatment of myocardial infarction. *J Am Coll Cardiol*. 2006;48:907-913

78. Singelyn JM, Christman KL. Injectable materials for the treatment of myocardial infarction and heart failure: The promise of decellularized matrices. *J Cardiovasc Transl Res*. 2010;3:478-486

79. Nelson DM, Ma Z, Fujimoto KL, Hashizume R, Wagner WR. Intra-myocardial biomaterial injection therapy in the treatment of heart failure: Materials, outcomes and challenges. *Acta Biomater*. 2011;7:1-15

80. Singelyn JM, Christman KL. Injectable materials for the treatment of myocardial infarction and heart failure: The promise of decellularized matrices. *Journal of Cardiovascular Translational Research*. 2010;3:478-486

81. Baker SC, Atkin N, Gunning PA, Granville N, Wilson K, Wilson D, Southgate J. Characterisation of electrospun polystyrene scaffolds for three-dimensional in vitro biological studies. *Biomaterials*. 2006;27:3136-3146

82. Mauck RL, Baker BM, Nerurkar NL, Burdick JA, Li W-J, Tuan RS, Elliott DM. Engineering on the straight and narrow: The mechanics of nanofibrous assemblies for fiber-reinforced tissue regeneration. *Tissue engineering. Part B, Reviews*. 2009;15:171-193

83. Latinovic O, Hough LA, Ou-Yang HD. Structural and micromechanical characterization of type i collagen gels. *Journal of Biomechanics*. 2010;43:500-505

84. Yeo I-S, Oh J-E, Jeong L, Lee TS, Lee SJ, Park WH, Min B-M. Collagen-based biomimetic nanofibrous scaffolds: Preparation and characterization of collagen/silk fibroin bicomponent nanofibrous structures. *Biomacromolecules*. 2008;9:1106-1116

85. Li Y, Asadi A, Monroe M. Ph effects on collagen fibrillogenesis in vitro: Electrostatic interactions and phosphate binding. *Materials Science and …*. 2009

86. Wood GC, Keech MK. The formation of fibrils from collagen solutions 1. The effect of experimental conditions: Kinetic and electron-microscope studies. *Biochemical Journal*. 1960;75:588

87. Achilli M, Mantovani D. Tailoring mechanical properties of collagen-based scaffolds for vascular tissue engineering: The effects of ph, temperature and ionic strength on gelation. *Polymers*. 2010;2:664-680

88. Engler AJ, Griffin MA, Sen S, Bönnemann CG, Sweeney HL, Discher DE. Myotubes differentiate optimally on substrates with tissue-like stiffness: Pathological implications for soft or stiff microenvironments. *The Journal of cell biology*. 2004;166:877-887

89. Harris JR, Reiber A. Influence of saline and ph on collagen type i fibrillogenesis in vitro: Fibril polymorphism and colloidal gold labelling. *Micron (Oxford, England : 1993)*. 2007;38:513-521

90. Brightman A, Rajwa B, Sturgis J. Time-lapse confocal reflection microscopy of collagen fibrillogenesis and extracellular matrix assembly in vitro. *Biopolymers*. 2000

91. Singelyn JM, DeQuach JA, Seif-Naraghi SB, Littlefield RB, Schup-Magoffin PJ, Christman KL. Naturally derived myocardial matrix as an injectable scaffold for cardiac tissue engineering. *Biomaterials*. 2009;30:5409-5416

92. DeQuach JA, Mezzano V, Miglani A, Lange S, Keller GM, Sheikh F, Christman KL. Simple and high yielding method for preparing tissue specific extracellular matrix coatings for cell culture. *PLoS One*. 2010;5:e13039

93. Yang Y-l, Kaufman LJ. Rheology and confocal reflectance microscopy as probes of mechanical properties and structure during collagen and collagen/hyaluronan self-assembly. *Biophysical journal*. 2009;96:1566-1585

94. Chan RW, Titze IR. Viscosities of implantable biomaterials in vocal fold augmentation surgery. *The Laryngoscope*. 1998;108:725-731

95. Pogorelov AG, Selezneva II. Evaluation of collagen gel microstructure by scanning electron microscopy. *Bulletin of experimental biology and medicine*. 2010;150:153-156

96. Lutolf MP, Hubbell JA. Synthesis and physicochemical characterization of end-linked poly(ethylene glycol)-co-peptide hydrogels formed by michael-type addition. *Biomacromolecules*. 2003;4:713-722

97. Gelman RA, Williams BR, Piez KA. Collagen fibril formation. Evidence for a multistep process. *The Journal of biological chemistry*. 1979;254:180-186

98. Burgess ML, McCrea JC, Hedrick HL. Age-associated changes in cardiac matrix and integrins. *Mechanisms of Ageing and Development*. 2001;122:1739-1756

99. Leeuwenburgh C, Wagner P, Holloszy JO, Sohal RS, Heinecke JW. Caloric restriction attenuates dityrosine cross-linking of cardiac and skeletal muscle proteins in aging mice. *Arch. Biochem. Biophys.* 1997;346:74-80

100. Anna Biernacka NGF. Aging and cardiac fibrosis. *Aging and Disease*. 2011;2:158

101. de Souza RR. Aging of myocardial collagen. *Biogerontology*. 2002;3:325-335

102. Keane TJ, Londono R, Turner NJ, Badylak SF. Consequences of ineffective decellularization of biologic scaffolds on the host response. *Biomaterials*. 2012;33:1771-1781

103. Zheng MH, Chen J, Kirilak Y, Willers C, Xu J, Wood D. Porcine small intestine submucosa (sis) is not an acellular collagenous matrix and contains porcine DNA: Possible implications in human implantation. *J. Biomed. Mater. Res.* 2005;73B:61-67

104. Oberwallner B, Brodarac A, Choi Y-H, Saric T, Anić P, Morawietz L, Stamm C. Preparation of cardiac extracellular matrix scaffolds by decellularization of human myocardium. *J. Biomed. Mater. Res.* 2013

105. Godier-Furnémont AFG, Martens TP, Koeckert MS, Wan L, Parks J, Arai K, Zhang G, Hudson B, Homma S, Vunjak-Novakovic G. Composite scaffold provides a cell delivery platform for cardiovascular repair. *Proc. Natl. Acad. Sci. U.S.A.* 2011;108:7974-7979

106. Reing JE, Brown BN, Daly KA, Freund JM, Gilbert TW, Hsiong SX, Huber A, Kullas KE, Tottey S, Wolf MT, Badylak SF. The effects of processing methods upon mechanical and biologic properties of porcine dermal extracellular matrix scaffolds. *Biomaterials*. 2010;31:8626-8633

107. Seif-Naraghi SB, Horn D, Schup-Magoffin PJ, Christman KL. Injectable extracellular matrix derived hydrogel provides a platform for enhanced retention and delivery of a heparin-binding growth factor. *Acta biomaterialia*. 2012

108. Raman R, Sasisekharan V, Sasisekharan R. Structural insights into biological roles of protein-glycosaminoglycan interactions. *Chemistry & Biology*. 2005;12:267-277

109. Tottey S, Johnson SA, Crapo PM, Reing JE, Zhang L, Jiang H, Medberry CJ, Reines B, Badylak SF. The effect of source animal age upon extracellular matrix scaffold properties. *Biomaterials*. 2011;32:128-136

110. Valentin JE, Badylak JS, McCabe GP, Badylak SF. Extracellular matrix bioscaffolds for orthopaedic applicationsa comparative histologic study. *J Bone Joint Surg Am*. 2006;88:2673-2686

111. Sicari BM, Johnson SA, Siu BF, Crapo PM, Daly KA, Jiang H, Medberry CJ, Tottey S, Turner NJ, Badylak SF. The effect of source animal age upon the in vivo remodeling characteristics of an extracellular matrix scaffold. *Biomaterials*. 2012;33:5524-5533

112. Barbosa I, Garcia S, Barbier-Chassefière V, Caruelle J-P, Martelly I, Papy-García D. Improved and simple micro assay for sulfated glycosaminoglycans quantification in biological extracts and its use in skin and muscle tissue studies. *Glycobiology*. 2003;13:647-653

113. Wisniewski JR, Zougman A, Nagaraj N, Mann M. Universal sample preparation method for proteome analysis. *Nature methods*. 2009;6:359-362

114. Johnson TD, Lin SY, Christman KL. Tailoring material properties of a nanofibrous extracellular matrix derived hydrogel. *Nanotechnology*. 2011;22:494015

115. San Antonio JD, Karnovsky MJ, Ottlinger ME, Schillig R, Pukac LA. Isolation of heparin-insensitive aortic smooth muscle cells. Growth and differentiation. *Arteriosclerosis and thrombosis : a journal of vascular biology / American Heart Association*. 1993;13:748-757

116. Gaetani R, Doevendans PA, Metz CHG, Alblas J, Messina E, Giacomello A, Sluijter JPG. Cardiac tissue engineering using tissue printing technology and human cardiac progenitor cells. *Biomaterials*. 2012;33:1782-1790

117. Smits AM, van Vliet P, Metz CH, Korfage T, Sluijter JP, Doevendans PA, Goumans M-J. Human cardiomyocyte progenitor cells differentiate into functional mature cardiomyocytes: An in vitro model for studying human cardiac physiology and pathophysiology. *Nat Protoc*. 2009;4:232-243

118. Christman KL, Fok HH, Sievers RE, Fang Q, Lee RJ. Fibrin glue alone and skeletal myoblasts in a fibrin scaffold preserve cardiac function after myocardial infarction. *Tissue Eng.* 2004;10:403-409

119. Badylak SF. The extracellular matrix as a biologic scaffold material. *Biomaterials*. 2007;28:3587-3593

120. Pashuck ET, Stevens MM. Designing regenerative biomaterial therapies for the clinic. *Science translational medicine*. 2012;4:160sr164

121. Nguyen DH, Hurtado-Ziola N, Gagneux P, Varki A. Loss of siglec expression on t lymphocytes during human evolution. *Proc. Natl. Acad. Sci. U.S.A.* 2006;103:7765-7770

122. Varki NM, Strobert E, Dick EJ, Benirschke K, Varki A. Biomedical differences between human and nonhuman hominids: Potential roles for uniquely human aspects of sialic acid biology. *Annu Rev Pathol*. 2011;6:365-393

123. Říhová B. Biocompatibility of biomaterials: Hemocompatibility, immunocompatiblity and biocompatibility of solid polymeric materials and soluble targetable polymeric carriers. *Advanced Drug Delivery Reviews*. 1996;21:157-176

124. Onuki Y, Bhardwaj U, Papadimitrakopoulos F. A review of the biocompatibility of implantable devices: Current challenges to overcome foreign body response. *J Diabetes Sci*. 2008

125. Legrand N, Weijer K. Experimental models to study development and function of the human immune system in vivo. *The Journal of Immunology*. 2006

126. Lan P, Tonomura N, Shimizu A, Wang S, Yang Y-G. Reconstitution of a functional human immune system in immunodeficient mice through combined human fetal thymus/liver and cd34+ cell transplantation. *Blood*. 2006;108:487-492

127. Zhang B, Duan Z, Zhao Y. Mouse models with human immunity and their application in biomedical research. *Journal of Cellular and Molecular Medicine*. 2009;13:1043-1058

128. Tonomura N, Shimizu A, Wang S, Yamada K, Tchipashvili V, Weir GC, Yang Y-G. Pig islet xenograft rejection in a mouse model with an established human immune system. *Xenotransplantation*. 2008;15:129-135

129. Rong Z, Wang M, Hu Z, Stradner M, Zhu S, Kong H, Yi H, Goldrath A, Yang YG, Xu Y, Fu X. An effective approach to prevent immune rejection of human esc-derived allografts. *Cell stem cell*. 2014;14:121-130

130. Johnson TD, DeQuach JA, Gaetani R, Ungerleider J, Elhag D, Nigam V, Behfar A, Christman KL. Human versus porcine tissue sourcing for an injectable myocardial matrix hydrogel. *Biomater. Sci.* 2014;2:735-744

131. Badylak SF. Decellularized allogeneic and xenogeneic tissue as a bioscaffold for regenerative medicine: Factors that influence the host response. *Annals of Biomedical Engineering*. 2014;42:1517-1527

132. Vuyyuru R, Patton J, Manser T. Human immune system mice: Current potential and limitations for translational research on human antibody responses. *Immunologic research*. 2011;51:257-266

133. Brown BN, Ratner BD, Goodman SB, Amar S, Badylak SF. Macrophage polarization: An opportunity for improved outcomes in biomaterials and regenerative medicine. *Biomaterials*. 2012;33:3792-3802

134. Reiner SL. Helper t cell differentiation, inside and out. *Current opinion in immunology*. 2001;13:351-355

135. Pierson RN. Xenogeneic skin graft rejection is especially dependent on cd4+ t cells. *Journal of Experimental Medicine*. 1989;170:991-996

136. Chakir H, Wang H, Lefebvre DE, Webb J, Scott FW. T-bet/gata-3 ratio as a measure of the th1/th2 cytokine profile in mixed cell populations: Predominant role of gata-3. *Journal of immunological methods*. 2003;278:157-169

137. Allman A, McPherson T, Badylak S, Merrill L, Kallakury B, Sheehan C, Raeder R, Metzger D. Xenogeneic extracellular matrix grafts elicit a th2-restricted immune response. *Transplantation*. 2001;71:1631-1640

138. Bonecchi R, Sozzani S, Stine JT, Luini W, D'Amico G, Allavena P, Chantry D, Mantovani A. Divergent effects of interleukin-4 and interferon-gamma on macrophage-derived chemokine production: An amplification circuit of polarized t helper 2 responses. *Blood*. 1998;92:2668-2671

139. Monney L, Sabatos CA, Gaglia JL, Ryu A, Waldner H, Chernova T, Manning S, Greenfield EA, Coyle AJ, Sobel RA, Freeman GJ, Kuchroo VK. Th1-specific cell surface protein tim-3 regulates macrophage activation and severity of an autoimmune disease. *Nature*. 2002;415:536-541

140. Mosser D. The many faces of macrophage activation. *J Leukocyte Biol*. 2003

141. Porcheray F, Viaud S, Rimaniol A-C, Leone C, Samah B, Dereuddre-Bosquet N, Dormont D, Gras G. Macrophage activation switching: An asset for the resolution of inflammation. *Clin Exp Immunol*. 2005;142:481-489

142. Gordon S. Alternative activation of macrophages. *Nat. Rev. Immunol.* 2003

143. Mantovani A, Sica A, Locati M. Macrophage polarization comes of age. *Immunity*. 2005;23:344-346

144. Brown BN, Valentin JE, Stewart-Akers AM, McCabe GP, Badylak SF. Macrophage phenotype and remodeling outcomes in response to biologic scaffolds with and without a cellular component. *Biomaterials*. 2009;30:1482-1491

145. O'Gorman MR, Thomas J. Isotype controls--time to let go? *Cytometry*. 1999;38:78-80

146. Maecker HT, Trotter J. Flow cytometry controls, instrument setup, and the determination of positivity. *Cytometry*. 2006;69A:1037-1042

147. Glimcher LH, Murphy KM. Lineage commitment in the immune system: The t helper lymphocyte grows up. *Genes & development*. 2000;14:1693-1711

148. Brown BN, Badylak SF. Expanded applications, shifting paradigms and an improved understanding of host-biomaterial interactions. *Acta biomaterialia*. 2013;9:4948-4955

149. Stout R, Jiang C, Matta B, Tietzel I, Watkins S, Suttles J. Macrophages sequentially change their functional phenotype in response to changes

in microenvironmental influences. *Journal of immunology*. 2005;175:342-349

150. Mills CD, Kincaid K, Alt JM, Heilman MJ, Hill AM. M-1/m-2 macrophages and the th1/th2 paradigm. *Journal of immunology*. 2000;164:6166-6173

151. Valentin JE, Stewart-Akers AM, Gilbert TW, Badylak SF. Macrophage participation in the degradation and remodeling of extracellular matrix scaffolds. *Tissue engineering. Part A*. 2009;15:1687-1694

152. Badylak SF, Valentin JE, Ravindra AK, McCabe GP, Stewart-Akers AM. Macrophage phenotype as a determinant of biologic scaffold remodeling. *Tissue engineering. Part A*. 2008;14:1835-1842

153. Kigerl KA, Gensel JC, Ankeny DP, Alexander JK, Donnelly DJ, Popovich PG. Identification of two distinct macrophage subsets with divergent effects causing either neurotoxicity or regeneration in the injured mouse spinal cord. *The Journal of neuroscience : the official journal of the Society for Neuroscience*. 2009;29:13435-13444

154. Raeder RH, Badylak SF, Sheehan C, Kallakury B, Metzger DW. Natural anti-galactose α1, 3 galactose antibodies delay, but do not prevent the acceptance of extracellular matrix xenografts. *Transpl. Immunol.* 2002;10:15-24

155. Galili U, LaTemple DC, Radic MZ. A sensitive assay for measuring alpha-gal epitope expression on cells by a monoclonal anti-gal antibody. *Transplantation*. 1998;65:1129-1132

156. Livak KJ, Schmittgen TD. Analysis of relative gene expression data using real-time quantitative pcr and the 2(-delta delta c(t)) method. *Methods*. 2001;25:402-408

157. Ferguson VL, Dodson RB. Bioengineering aspects of the umbilical cord. *Eur J Obstet Gyn R B*. 2009;144:S108-S113

158. Colwell A, Longaker M. Fetal wound healing. *Frontiers in bioscience : a journal and virtual library*. 2003

159. Toole BP, Wight TN, Tammi MI. Hyaluronan-cell interactions in cancer and vascular disease. *The Journal of biological chemistry*. 2002;277:4593-4596

160. Niiyama H, Huang NF, Rollins MD, Cooke JP. Murine model of hindlimb ischemia. *Journal of visualized experiments : JoVE*. 2009

161. Limbourg A, Korff T, Napp LC, Schaper W, Drexler H, Limbourg FP. Evaluation of postnatal arteriogenesis and angiogenesis in a mouse model of hind-limb ischemia. *Nat Protoc*. 2009;4:1737-1746

162. Rivard A, Silver M, Chen D, Kearney M, Magner M, Annex B, Peters K, Isner JM. Rescue of diabetes-related impairment of angiogenesis by intramuscular gene therapy with adeno-vegf. *Am J Pathol*. 1999;154:355-363

163. Hartman JC, Pagel PS, Proctor LT, Kampine JP, Schmeling WT, Warltier DC. Influence of desflurane, isoflurane and halothane on regional tissue perfusion in dogs. *Can J Anaesth*. 1992;39:877-887

164. Meyer GA, Lieber RL. Skeletal muscle fibrosis develops in response to desmin deletion. *Am. J. Physiol., Cell Physiol.* 2012;302:C1609-1620

165. Wróblewski R, Edström L, Mair WG. Five different types of centrally nucleated muscle fibres in man: Elemental composition and morphological criteria. A study of myopathies, fetal tissue and muscle spindle. *J. Submicrosc. Cytol.* 1982;14:377-387

166. Ouma GO, Zafrir B, Mohler ER, Flugelman MY. Therapeutic angiogenesis in critical limb ischemia. *Angiology*. 2013;64:466-480

167. Haas TL, Lloyd PG, Yang HT, Terjung RL. Exercise training and peripheral arterial disease. *Comprehensive Physiology*. 2012;2:2933-3017

168. Buschmann I, Schaper W. Arteriogenesis versus angiogenesis: Two mechanisms of vessel growth. *News in physiological sciences : an international journal of physiology produced jointly by the International Union of Physiological Sciences and the American Physiological Society*. 1999;14:121-125

169. Scholz D, Ziegelhoeffer T, Helisch A, Wagner S, Friedrich C, Podzuweit T, Schaper W. Contribution of arteriogenesis and angiogenesis to postocclusive hindlimb perfusion in mice. *Journal of molecular and cellular cardiology*. 2002;34:775-787

170. Young DA, Ibrahim DO, Hu D, Christman KL. Injectable hydrogel scaffold from decellularized human lipoaspirate. *Acta biomaterialia*. 2011;7:1040-1049

171. Sicari BM, Rubin JP, Dearth CL, Wolf MT, Ambrosio F, Boninger M, Turner NJ, Weber DJ, Simpson TW, Wyse A, Brown EH, Dziki JL, Fisher LE, Brown S, Badylak SF. An acellular biologic scaffold

promotes skeletal muscle formation in mice and humans with volumetric muscle loss. *Science translational medicine*. 2014;6:234ra258

172. Badylak S, Vorp D, Spievack A, Simmons-Byrd A, Hanke J, Freytes D, Thapa A, Gilbert T, Nieponice A. Esophageal reconstruction with ecm and muscle tissue in a dog model. *J Surg Res*. 2005;128:87-97

173. Bach F, Ferran C, Hechenleitner P, Mark W. Accommodation of vascularized xenografts: Expression of “protective genes” by donor endothelial cells in a host th2 cytokine environment. *Nature medicine*. 1997

174. Singh VK, Mehrotra S, Agarwal SS. The paradigm of th1 and th2 cytokines: Its relevance to autoimmunity and allergy. *Immunologic research*. 1999;20:147-161

175. Brown BN, Londono R, Tottey S, Zhang L, Kukla KA, Wolf MT, Daly KA, Reing JE, Badylak SF. Macrophage phenotype as a predictor of constructive remodeling following the implantation of biologically derived surgical mesh materials. *Acta biomaterialia*. 2012;8:978-987

176. Cortiella J, Niles J, Cantu A, Brettler A, Pham A, Vargas G, Winston S, Wang J, Walls S, Nichols JE. Influence of acellular natural lung matrix on murine embryonic stem cell differentiation and tissue formation. *Tissue engineering. Part A*. 2010;16:2565-2580

177. Sellaro TL, Ravindra AK, Stolz DB, Badylak SF. Maintenance of hepatic sinusoidal endothelial cell phenotype in vitro using organ-specific extracellular matrix scaffolds. *Tissue Eng.* 2007;13:2301-2310

178. Cheng N-C, Estes BT, Awad HA, Guilak F. Chondrogenic differentiation of adipose-derived adult stem cells by a porous scaffold derived from native articular cartilage extracellular matrix. *Tissue engineering. Part A*. 2009;15:231-241

179. Waters RE, Terjung RL, Peters KG, Annex BH. Preclinical models of human peripheral arterial occlusive disease: Implications for investigation of therapeutic agents. *Journal of Applied ….* 2004

180. Lallier TE, Miner QW, Jr., Sonnier J, Spencer A. A simple cell motility assay demonstrates differential motility of human periodontal ligament fibroblasts, gingival fibroblasts, and pre-osteoblasts. *Cell and tissue research*. 2007;328:339-354

181. Senarathna J, Rege A, Li N, Thakor NV. Laser speckle contrast imaging: Theory, instrumentation and applications. *IEEE Rev. Biomed. Eng.* 2013;6:99-110

182. Roustit M, Millet C, Blaise S, Dufournet B, Cracowski JL. Excellent reproducibility of laser speckle contrast imaging to assess skin microvascular reactivity. *Microvasc. Res.* 2010;80:505-511

183. Zechner C, Lai L, Zechner JF, Geng T, Yan Z, Rumsey JW, Collia D, Chen Z, Wozniak DF, Leone TC, Kelly DP. Total skeletal muscle pgc-1 deficiency uncouples mitochondrial derangements from fiber type determination and insulin sensitivity. *Cell metabolism*. 2010;12:633-642

184. Brooke MH, Kaiser KK. Three "myosin adenosine triphosphatase" systems: The nature of their ph lability and sulfhydryl dependence. *J Histochem Cytochem*. 1970;18:670-672